The Luminous, the Massive and the Dusty: a Near- to Mid-Infrared Spectroscopic Study of Submillimeter Galaxies

Thesis by

Karín Menéndez-Delmestre

In Partial Fulfillment of the Requirements

for the Degree of

Doctor of Philosophy

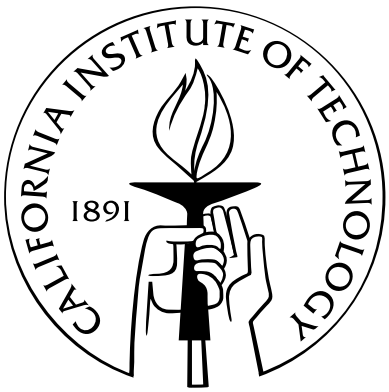

California Institute of Technology

Pasadena, California

2009

(Defended August 26, 2008)

Acknowledgements

All along my PhD at Caltech I have been the lucky receiver of many people's support. I am now facing the difficult task of verbally exposing my deepest thanks. If by reading this you have the impression I am thanking half of the planet, you are probably right! But, hey, as long as the acknowledgements are not longer than the thesis, I am sticking to the 'etiquette'. It seems like this is the first time that I have the opportunity to *officially* thank the individuals who have in one way or another helped me get where I am today. So I will start at the beginning, thanking Alfredo Torruella and Antonio Algaze, who during my early undergrad years at the University of Puerto Rico were key in captivating my attention in Physics; and Carmen Pantoja, thanks to whom I had the great chance of working at the fantastic Arecibo observatory (can anyone guess a slight bias?) and who has followed all of my adventures in the world of astronomy. I want to give special thanks to: Blanca Silvestrini, my earliest and constant mentor; Vicky Kaspi, with whom I had the chance of overlapping at McGill just before I graduated; Karl-Heinz Mack, with whom I worked at ASTRON in the Netherlands during the summer in which I discovered that astronomy had entered my life to stay; Paul van der Werf, who graciously welcomed me into his research group at the Leiden Sterrewacht to undertake a year of research; and Kirsten Kraiberg Knudsen, with whom I had the outmost pleasure to share an office at Leiden and who has ever since remained a dear friend.

During my years at Caltech, I had the chance of meeting and interacting with a lot of wonderful people. I especially want to thank David R. Law and Sarah Prunier-Law, for being so open and loving, for fun game nights and for dropping by unexpectedly at my place (you know we love it!). I am also particularly thankful to Hilke Schlicht-

ing, whose company as a running partner, friend and confidant was invaluable for me during our years of overlap here at Caltech. I also want to give special thanks to the group of gals with whom I enjoyed many fun days and nights of dancing, chatting and relaxing: Cathy Slesnick (nobody else is able to pull me out of bed for a run in the early morning!), Laura Hainline, Melissa Enoch and Danielle Cameron. Special thanks to Laura, who warmly welcomed me at her place when I first came to Caltech as a prospective student and who I very much enjoyed having as my big-sis (submillimetrically-speaking!)

I thank all the fun and wonderful people I met during my first year at Caltech and who helped me survive the ordeal of classes, exams and the general lack of social life: Sébastien Blais-Ouellette, Roger Donaldson, Jonathan Pritchard and my dear friend, Alexie Leauthaud. I thank my housemates Dawn Erb and Margaret Pan, with whom I shared a beautiful apartment and an awful landlord (and whose calm and inner-peace made it endurable for me!) I am also especially thankful to Dawn Erb, who was truly helpful and available in my second year craze of getting to know the ins-and-outs of NIRSPEC. I thank my classmates, with whom I rode the PhD years from their (fresh!) beginning to the (long-awaited) end: P. Brian Cameron, Adam L. Kraus, David R. Law, Dan P. Stark and Larry C. Weintraub.

An invaluable aspect of my time in Caltech has been the continuing waves of new people that I have come to meet (and to keep as good friends!), including: Jeandrew Brink, with whom I enjoyed very many good conversations over a weekly coffee sponsored by the Women Mentoring Women program (thanks Women's Center!); Kalliopi Dasyra, who has been a great friend since the very first time we met; Elisabeth Krause, who is always up for a camping trip or cooking great desserts for other people's great pleasure (ok, especially mine!); Johan Richard, with whom I have shared so many lovely evenings of dinner and games; Laura Perez and Walter Max-Moerbeck, with whom I look forward to many fun future moments; and Stuartt Corder, who has been a great partner during the thesis-crisis time of these past memorable months. Thanks to Greg Herzceg, JJ Gonzalez and John Long for unforgettably encounters of medianoches and cubanos. I am also especially grateful to Kartik Sheth, with whom

I worked closely during my first year on the wonders of barred galaxies in the local Universe and who through the years has been an enthusiastic and dedicated mentor, an (insistent!) gym-buddy, an ever-ready coffee-partner and a good friend.

I am also grateful to the many people who have helped me throughout my years at Robinson: Patrick Shopbell, Anu Mahabal and Cheryl Southard who have been crucial in helping me keep the faith on computers; Gina Armas, Diane Fujitani, Sandy Lester, Judith Mack, Judy McClain and Gita Patel for keeping the administrative wheels turning at Robinson, for helping in my travel (and money!) arrangements and for always being so nice and available.

I thank my Thesis (and Candidacy) defense committee (in advance!): Nick Z. Scoville, Andrew W. Blain, Judy Cohen, Lee Armus and Andrew Benson, as well as Mark Kamionkowski and Richard Ellis (though *in absentia* for the Thesis defense).

Naturally, this thesis would not have come together without the direction, support and guidance of my advisor, Andrew W. Blain. I am also greatly indebted to my collaborators, who have been incredibly instrumental through my years at Caltech. I thank Scott Chapman for serendipitously approaching me at the Robinson lounge and chatting me up on the vast research possibilities under Andrew's wing. I am certainly happy with how things turned out! I also want to give special thanks to Ian Smail, Mark Swinbank and Dave M. Alexander at Durham University in the UK, who really went out of their way to get involved and to provide (tons!) of resourceful insight to our collaborative work and who welcomed me in my visits to their Department. I also want to thank Lee Armus for his invaluable input and constructive criticism.

Thanks to all my old friends who have been so supportive through the years and who I hold so dear in my heart: Javier F. Silvestrini, Carla Friedrich, Laura Fregonese and Abigail Noain. At the pinnacle of all these thanks, is my family, my best-friend Sara and my beloved Thiago S. Gonçalves. Ma, pa, Katiuska, Raissuneta y papi: no hubiese aguantado sin el maravilloso y frecuente apoyo y cariño telefónico de ustedes. Sarucha, gracias por aguantar mis quejas doctorísticas y por estar de mi lado. Thiago, você é a coisa mais linda que levo desses anos... Gracias por mantenerme cuerda.

Abstract

Submillimeter (submm) surveys have uncovered a population of dust-enshrouded ultra-luminous galaxies ($L_{8-1000\,\mu m} \gtrsim few \times 10^{12}\ L_\odot$) that are inconspicuous in deep surveys at shorter wavelengths. Inferred to have high star-formation rates (SFRs $\gtrsim$ 1000 $M_\odot\ yr^{-1}$), submm-selected galaxies (SMGs) contribute significantly to the global SFR density at $z \sim 2-3$ and are thus critical players in building up stars in galaxies. Many SMGs have been shown to display X-ray, optical and near-infrared (IR) signatures of active galactic nuclei (AGN), prompting the question: how significant is the AGN contribution to their total luminosity? Central to understanding SMGs is the study of the nature of their power source, their internal dynamics, their SFRs and their masses. We study mid-IR and near-IR spectra of SMGs to investigate these aspects.

We have obtained the largest sample of 24 SMGs to date with the mid-IR *Spitzer* Infrared Spectrograph (IRS) at $z \sim 0.65-3.2$. Broad emission features from polycyclic aromatic hydrocarbons – typically associated to intense star-formation – are almost ubiquitous in the sample and the composite spectrum is well fit by a combination of a starburst component with an additional power law representing a $\lesssim 35\%$ AGN contribution to the bolometric luminosity. We find weak silicate absorption in contrast to local ultra-luminous IR galaxies (ULIRGs), suggesting that the mid-IR visible star formation in SMGs occurs in a more extended component.

We also study the near-IR emission of SMGs with the OH-Suppressing Infrared Imaging Spectrograph (OSIRIS), together with the Keck Laser-Guide Star Adaptive Optics system, to investigate the distribution and dynamics of the ionized gas. The two-dimensional insight of these observations allow us to distinguish and quantify

the compact AGN emission, which allows us to refine estimates of dynamical masses, SFRs and gas masses for the population. With a spatially-resolved spectroscopic insight into the kpc-scale structure of these galaxies, we find that the Hα emission in SMGs extends over scales $\sim 4 - 17$ kpc, setting SMGs apart from local ULIRGs, where intense emission is confined to the central $\lesssim 1$ kpc.

Contents

List of Figures

List of Tables

Chapter 1

Introduction

Galaxies host a myriad of astrophysical processes that encompass various physical scales, unfold on different characteristic timescales and whose luminous evidence spread over the full extent of the electromagnetic spectrum. The distribution of energy at different frequencies, or the spectral energy distribution (SED) of a galaxy, holds the key to understanding details of the processes taking place within, and which dominate the luminous output at each wavelength. The SED of a galaxy can be approximated by two main *bumps*: the *stellar* bump, extending from the ultraviolet (UV) to the optical and near-infrared ($\lambda \sim 0.1 - 3\mu$m); and the infrared (IR) bump, encompassing the longer mid-IR and far-IR wavelengths ($\lambda \sim 3 - 500\mu$m). The stellar bump arises from direct starlight escaping star-forming regions. On the other hand, the IR-bump corresponds mainly to thermal continuum emission from interstellar dust grains heated to temperatures in the range of $T \sim 15 - 1000$ K, depending on the hardness and intensity of the interstellar radiation field, and the size and chemical composition of the dust grains. In normal galaxies, the origin of this thermal emission is typically star formation, where UV photons are absorbed by intervening dust grains and re-radiated at longer wavelengths. However, in galaxies harboring an active galactic nucleus (AGN), star formation is not the sole source of IR emission. A significant fraction of the IR luminosity can also be attributed to dust re-radiated emission arising from regions close to the central AGN, where optical-to-hard-UV photons emitted from the accretion disk abound.

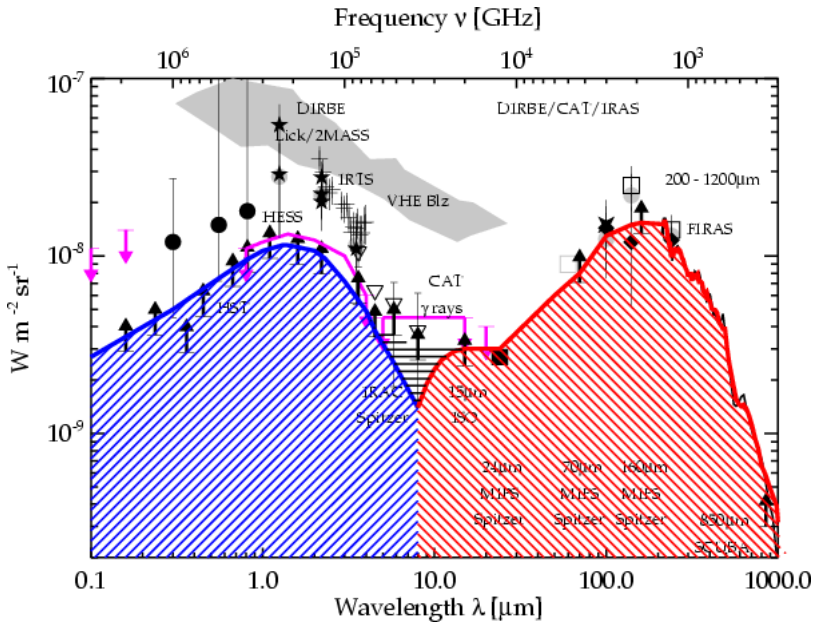

Figure 1.1 Spectral energy distribution of the Extragalactic Background Light (νI_ν vs. λ), taken from Dole et al. (2006). We can directly compare the Cosmic Optical Background (COB; blue hatched region) to the Cosmic Infrared Background (CIB; red hatched region) and see that the CIB accounts for roughly half of the total energy. Half of the extragalactic background light comes from starlight and half comes from dust-reprocessed light.

1.1 The Extragalactic Background Light and the Evolution in IR number counts

The collection of light emitted by all galaxies in the Universe makes up the Extragalactic Background (see Fig. 1.1). The SED of the Extragalactic Background can be divided into the mainly stellar Cosmic Optical Background (COB) and the reprocessed Cosmic Infrared Background (CIB) from dust emission, either from star-forming regions or AGN.

The cryogenic era of the *Spitzer* Telescope has allowed us to impose strict constraints on the IR number counts of the CIB (e.g., Dole et al. 2006 and references therein). Characterizing the different contributions to the Extragalactic Background in terms of number counts, redshift distribution and luminosity functions has been the focus of many recent studies (e.g., Gispert et al. 2000; Le Floc'h et al. 2005; Dole

et al. 2006). As can be seen from Fig. 1.1, the CIB accounts for roughly the same amount of energy as the COB. This finding is of paramount significance, as it means that there is as much unobscured radiated emission from galaxies as it is hidden from our view by intervening dust. Therefore, in order to constrain the global stellar budget, we need to consider not only the unobscured star formation, but also constrain how much star formation is responsible for the CIB.

How much of the IR light arises from star formation rather than AGN activity? In other words, how much of the energy enclosed by the CIB accounts for the build-up of super-massive black holes (SMBHs) and how much for the growth of stellar mass? To distinguish these two possible sources of dust emission and quantify the contribution of the CIB to the global star formation rate density (SFRD), it is crucial to constrain the SEDs of the individual IR-luminous sources that comprise the CIB. The outcome is also crucial to developing and testing galaxy formation models that seek to predict the interplay between the growth of SMBHs and the stellar bulk (Croton 2006; Monaco et al. 2007).

Locally the IR output of galaxies represents $\sim 30\%$ of their optical output (Soifer & Neugebauer 1991). Taking this into account, the roughly equal COB and CIB indicates that a shift in galaxy properties must have taken place at higher redshifts towards an enhanced IR emission. That is, to account for the total Extragalactic Background light an evolution in galaxy SEDs is necessary, with enhanced IR emission in the early Universe. Numerous IR studies have shown precisely such an evolution.

Within the local volume the galaxy luminosity function and SFRD is dominated by faint normal galaxies with bolometric luminosities $L_{bol} \lesssim 10^{11}$ $L_{\odot}$, such as the Milky Way (see Fig. 1.2). Galaxies with enhanced IR luminosities – such as Luminous and Ultra-Luminous Infrared Galaxies (LIRGs and ULIRGs with $10^{11} \lesssim L_{IR} \lesssim 10^{12}$ $L_{\odot}$ and $L_{IR} \gtrsim 10^{12}$ $L_{\odot}$, respectively; Sanders & Mirabel 1996) – are locally much less common than fainter galaxies. However, the contribution of these IR-luminous objects to the comoving energy density increases as we go out to higher redshifts, to the point where the contribution from LIRGs overtakes that of galaxies with lower IR luminosities at $z \sim 0.7$. At these intermediate redshifts, the contribution from

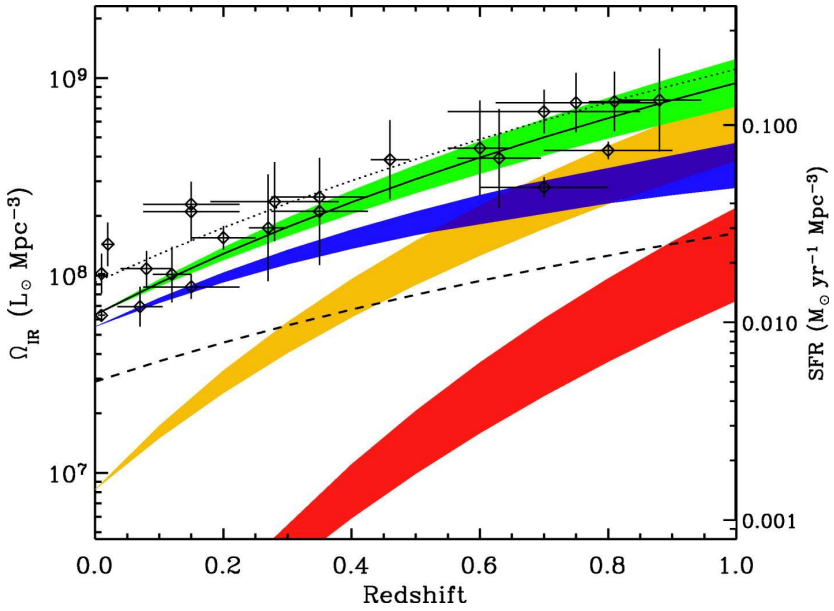

Figure 1.2 Comoving energy density as a function of redshift for galaxies based on IR luminosity, taken from Le Floc'h et al. (2005). The total contribution is denoted by the green curve. Also shown are the respective contributions from low-luminosity galaxies (i.e., $L_{IR} < 10^{11}$ $L_\odot$; blue), LIRGs (i.e., $10^{11} \lesssim L_{IR} < 10^{12}$ $L_\odot$; yellow), and ULIRGs (i.e., $L_{IR} \gtrsim 10^{12}$ $L_\odot$; red). At low redshifts, the comoving IR energy density is dominated by low-luminosity objects. However, the contribution from LIRGs overtakes that of the lower-luminosity galaxies at $z \sim 0.7$. ULIRGs, even though they are rare at these low redshifts, become rapidly important. The trend of their increasing contribution suggests that ULIRGs overtake that of LIRGs at $z \sim 2$ (see also Caputi et al. 2007).

ULIRGs still remains quite modest, though their contribution increments steadily with redshift from $z \sim 0$. Recent work suggests that the contribution of ULIRGs overtakes that of LIRGs at $z \gtrsim 2$ (Caputi et al. 2007). ULIRGs have thus undergone the fastest evolution in the last 8 Gyr, with their number density increasing by a factor of ~ 1000 from $z \sim 0$ to $z \sim 2$ (Chapman et al. 2005). Therefore, even though ULIRGs are quite rare in the local Universe and contribute a negligible fraction to the local SFRD, they have been found to be the major sites of massive star formation and metal production at higher redshifts (Smail et al. 2002).

1.2 Ultra-Luminous Infrared Galaxies at High Redshift: The Submillimeter Population

Most local ULIRGs are dust-enshrouded systems in the late stages of a merger (Sanders & Mirabel 1996; Veilleux et al. 2002) where both AGN and starburst activity coexist (e.g., Risaliti et al. 2006). Even though a range of dust temperatures can be ascribed to the IR bump of these objects, single temperatures of $T \sim 35 - 50$ K are typically a good fit to the SED at $\lambda \gtrsim 100\mu$m. At redshifts $z \sim 2$, the large IR luminous output is redshifted to longer wavelengths, making the far-IR ($\lambda \sim 70 - 200\mu$m), submillimeter (submm: $\lambda \sim 200\mu$m-1 mm) and millimeter (mm: $\lambda \sim 1 - 3$ mm) wavebands favorable regions to detect and study these high-redshift IR-luminous objects. Furthermore, the advantage of seeking sources at these wavebands is that the Rayleigh-Jeans SED is a steeply increasing function of frequency. This so-called *negative K-correction* translates into a flat or even increasing flux density with increasing redshift for a given temperature and luminosity, as we trace rest-frame wavelengths closer to the peak of the IR bump (see also Blain et al. 2002).

In the past two decades, hundreds of galaxies have been identified by submm and mm surveys at $\lambda \sim 850 - 125\,\mu$m (Smail et al. 1997; Barger, Cowie & Sanders 1999; Eales et al. 1999; Bertoldi et al. 2000; Cowie et al. 2002; Scott et al. 2002; Borys et al. 2003; Webb et al. 2003b; Coppin et al. 2005; Younger et al. 2007). The leading instruments for these discoveries and identifications have been the Submillimeter Common-User Bolometer Array (SCUBA; Holland et al. 1999) on the James Clerk Maxwell Telescope (JCMT)– which first gave these objects the name of *SCUBA galaxies*, the Max-Planck Millimeter Bolometer Array (MAMBO; Kreysa et al. 1998), BOLOCAM at the Caltech Submillimeter Observatory (Glenn et al. 1998) and more recently, the AzTEC camera (G. W. Wilson et al. 2008, in preparation) also on the JCMT. These submm observations preferentially pick out extremely luminous objects with cold dust temperatures, sufficient to boost the far-IR region of the thermal dust SED bump.

These submillimeter galaxies (hereafter, SMGs; see review by Blain et al. 2002)

comprise the bulk of the 850μm number counts (Borys et al. 2003; Knudsen et al. 2006) and their discovery rapidly held the promise of characterizing the contribution of individual galaxies to the CIB. However, the submm emission arises from thermal dust continuum emission and as such, the observed featureless spectrum reveals little about the astrophysics of these objects. For this reason, follow-up observations of this galaxy population have since been crucial to determine redshifts, luminosities and understand numerous details on the physical conditions within SMGs.

1.3 A Spectroscopically-Confirmed Sample: Radio-Identified Submillimeter Galaxies

The abundant dust that makes SMGs such prodigious submillimeter emitters, inevitably hampers the detection of rest-frame ultraviolet (UV) and optical emission from these objects. Photometric techniques that have been very successful at picking out large numbers of high-redshift galaxies (Lyman Break Galaxies or LBGs, Steidel et al. 2003; BzK galaxies, Daddi et al. 2004; BX/BM galaxies, Steidel et al. 2004; Distant Red Galaxies or DRGs, Franx et al. 2003) have thus proved ineffectual for SMGs. Despite great luminosities, the fraction of optical emission is quite modest in SMGs, $\sim 1\%$. Therefore, follow-up investigation of this optically-faint population has proved remarkably challenging. Furthermore, the large beam size $\sim 13''$ of the discovery mm and submm images do not offer sufficient angular resolution to pin-point the precise location of SMGs for follow-up observations at other wavelengths. This has hindered the progress in understanding the astrophysical details harbored within these galaxies.

Ultra-deep 1.4 GHz radio surveys with the Very Large Array (VLA) – with a $\sim$1.5$''$ beam-size – have provided the adequate angular resolution to identify radio counterparts to a substantial fraction of SMGs (e.g., Ivison et al. 1998, 2002). In this manner, $\sim 65\%$ of SMGs with $S_{850\mu m} > 5$ mJy are successfully identified with a μJy radio counterpart (see Chapman et al. 2005, hereafter C05, and references therein).

Even with precise radio locations on the sky, high S/N observations of SMGs at shorter wavelengths can remain very difficult, due to the high degree of obscuration present. However, deep near-IR imaging has resulted in the reliable identification of faint optical counterparts (Borys et al. 2004; Frayer et al. 2004; Smail et al. 2004).

With a useful sample of reliable counterparts in hand, the next crucial step in studying SMGs has been the determination of their spectroscopic redshifts. Prior to 2002, only a small number of SMGs actually had spectroscopic redshifts (Ivison et al. 1998, 2000; Barger et al. 1999b; Lilly et al. 1999). With a growing number of submm detections, a large redshift survey was clearly necessary. C05 describe the initiative of such an effort using the blue-sensitive Low-Resolution Imaging Spectrograph (LRIS-B; Oke et al. 1995; McCarthy et al. 1998) on Keck and obtained rest-frame UV redshifts for a large sample of 73 radio-identified SMGs, in the most part by identifying Lyα, and/or other emission and absorption lines. The success of these observations relied upon the surprising strength of the Lyα emission lines detected, considering the optical faintness of the population. These results indicate that Lyα photons can readily escape from SMGs, suggesting that the obscuring dust in these galaxies is not uniformly distributed, but rather clumpy in nature (Neufeld 1991; Chapman et al. 2004). The resulting redshift distribution of the SMG *radio-identified* sample revealed a median redshift of $< z > \sim 2.2$ (C05).

1.3.1 Potential Biases of the Radio-Detected Sample

A strong correlation has been shown to exist between the far-IR and radio emission in local star-forming galaxies (Helou et al. 1985; Condon 1992) and it has been further confirmed to extend to higher redshifts (Garrett 2002; Kovács et al. 2006). This relation appears to arise from an intrinsic connection between two very distinct processes that are ultimately governed by star formation: the far-IR emission is dominated by thermal dust emission arising from regions surrounding young, massive stars, while radio emission appears to be mostly due to the non-thermal synchrotron emission of cosmic rays – accelerated into the interstellar medium by supernova Type II and

Type Ib explosions – as they spiral around galactic-scale magnetic field lines. The fortuitous connection between such distinct mechanisms has been exploited to use deep radio observations as unbiased estimators of star formation of the dust-obscured high-redshift Universe (e.g., Yun et al. 2001). This has become especially useful in approaching the follow-up studies of galaxies detected at submm- and mm-wavebands, including the use of radio-to-submm spectral index technique to estimate redshifts for these objects (Carilli & Yun 1999).

Beyond the radio-identified sample of SMGs – with median flux densities of $< S_{1.4GHz} >\sim 75\mu$Jy – approximately $\sim 30\%$ of SMGs with $S_{850\mu\mathrm{m}} > 5\,$mJy remain without evident radio-counterparts at the sensitivity of current radio surveys (C05). To understand the inevitable selection biases we need to consider what objects are not represented within the radio-identified sample.

The lack of a radio counterpart in these SMGs can be attributed to higher redshifts ($z \gg 3$, C05; Younger et al. 2007): though submm observations benefit from negative K-correction, radio observations do not. Therefore, it is expected that with increasing redshift, the radio-to-submm flux ratio of the galaxy progressively decreases until the radio flux falls below the sensitivity of available radio instruments. It has also been suggested that radio-undetected SMGs may lie at similar redshifts as the radio-detected population, but that they have somewhat lower IR luminosities and colder characteristic dust temperatures, a combination which would result in similar observed 850-μm fluxes, but lower (and ultimately, undetectable) radio fluxes (Chapman et al. 2004). It is a priori impossible to distinguish between these two scenarios. The IR bump in the SED of dusty galaxies is thermal in origin, which implies that the observed submm- and radio-fluxes depend on $\mathrm{T}/(1+z)$ and so are affected exactly in the same manner by either increasing the redshift of the object or by reducing the dust temperature.

Despite these selection biases, the radio-identified sample presents a unique opportunity to study SMGs. They provide a large sample of objects with spectroscopically-confirmed redshifts, which are essential to undertake follow-up observations in order to build a steadily growing picture of the intrinsic nature of SMGs: their luminosities,

their masses and their powering sources, among others.

1.4 Submillimeter Galaxies: Ultra-Luminous Monsters at High-Redshift

Detailed follow-up observations of SMGs have revealed total IR luminosities of $L_{8-1000\mu m} \gtrsim 10^{12} - 10^{13}$ $L_{\odot}$ (C05), placing them under the ULIRG luminosity class (Sanders & Mirabel 1996). With substantial stellar masses $M_{stellar} \sim 10^{11}$ $M_{\odot}$, derived from photometry (Borys et al. 2005) and high SFRs $\gtrsim 100 - 1000$ $M_{\odot}$ yr^{-1} from optical (C05), near-IR (Swinbank et al. 2004) and X-ray work (Alexander et al. 2005a), SMGs are the likely progenitors of today's most massive galaxies ($L \gg L^{*}$; Lilly et al. 1999; Smail et al. 2004). As such, they are likely responsible for a large fraction of the stars that we see today.

Central to the study of SMGs is the source of their colossal bolometric luminosities. Deep optical and near-IR imaging has shown that SMGs typically display disturbed morphologies suggestive of merging or interacting systems (Smail et al. 1998, 2004), similar to what is observed in local ULIRGs. These results have prompted the idea that SMGs may be the high-z analogs of these extreme local objects, likely hosting similar astrophysical processes (e.g., C05). Local ULIRGs have been shown to be powered by intense and compact nuclear activity, either starburst in nature or arising from an embedded AGN, though in most instances being a composite of both power engines especially so as luminosity increases. In the case of SMGs, their submm selection suggests that if they are star-forming systems, then with SFRs $\sim$ 1000 $M_{\odot}yr^{-1}$ they would make a significant contribution to the global SFRD at $z = 2 - 3$ (C05). However, near-IR long-slit spectroscopy of SMGs by Swinbank et al. (2004) shows that these objects often – in $\sim$ 40% of cases – exhibit broad Hα lines (FWHM $\gtrsim$ 1000 km s^{-1}), revealing kinematic evidence of the large gas velocities within the broad-line region of a central AGN. Furthermore, ultra deep X-ray studies using the unique 2-Ms *Chandra* Deep Field-North (CDF-N) Survey suggest that $\sim 28 - 50\%$

host an obscured AGN (Alexander et al. 2005a), albeit under large columns of obscuring material ($N_H \gtrsim 10^{23} - 10^{24}$ cm^{-2}). These results all hint that star formation and AGN activity coexist within many SMGs, implying that we are witnessing the coupled growth of the stellar spheroid and a central SMBH (Alexander et al. 2008a).

With a mean redshift of $< z > \simeq 2.2$, the redshift distribution of radio-identified SMGs coincides with the global peak epoch of quasar activity (C05). The observational evidence connecting individual SMGs and AGNs, plus the coincidence of their redshift distributions strongly suggests that an evolutionary connection exists between these two populations. Such a connection is reminiscent of the merger–ULIRG–quasar evolution scenario first proposed by Sanders et al. (1988). Within this scenario, a merger between two gas-rich galaxies ignites intense star formation, which is initially obscured and likely corresponds to a dust-obscured ULIRG/submm-bright phase. As the central SMBH grows, feedback outflows carve channels through the dust obscuring material until the system becomes visible, entering the optically-bright quasar phase (see also Croton et al. 2006; Chakrabarti et al. 2006).

1.5 Aims of this Thesis

SMGs comprise an enigmatic galaxy population of which we are only now learning some of its detailed astrophysics. Reproducing the space number density of such starbursting monsters ($\sim 10^{-6}$ Mpc^{-3}; C05) at the high redshifts they occupy poses severe constraints to theoretical models of galaxy formation (Granato et al. 2000; Baugh et al. 2005). Attempts to match model predictions to the properties of SMGs have included deviating from the commonly adopted Salpeter initial mass function (IMF; Salpeter 1955) and invoking a top-heavy – in particular a $flat$ – IMF, in order to reconcile the stellar masses and SFRs at $z \sim 2$ with the masses of local massive ellipticals (e.g., Baugh et al. 2005). However, subsequent detailed work in the near-IR and X-ray has unveiled AGN signatures in a significant number of SMGs (Swinbank et al. 2004; Alexander et al. 2005a; Takata et al. 2006). This implies that a fraction of the total luminous output in SMGs may be due to AGN activity. Disentangling

the AGN contribution would potentially lead to lower SFRs and lower inferred stellar masses.

It is in the midst of these possibilities that I have undertaken the study of these galaxies. The focus of the research presented in this thesis is to increase our understanding of the detailed astrophysics hosted by SMGs. In particular, to investigate the contribution of AGN activity to the bolometric luminosities of SMGs (Chapters 2-3). We examine AGN signatures in the rest-frame optical spectra of individual SMGs (Chapter 4) and use integral field spectroscopic techniques to resolve for the first time the kpc-scale distribution of ionized gas in order to distinguish the AGN and extended emission regions and to revisit SFRs and dynamical masses uncontaminated by the AGN contribution (Chapter 5).

Near-IR and X-ray observations provide complementary insights into the emitting regions of SMGs and can be very useful at disclosing the presence of an AGN. In the near-IR, rest-frame optical emission lines may reveal kinematics or line ratios typical of ionized gas close to a central AGN. At the high X-ray energies direct continuum emission from hot gas close to an AGN can be detected at very high obscurations. Each of these approaches has its caveats: on the one hand, geometrical effects may hamper near-IR insight to the broad-line region of the AGN by intervening obscuring material; while on the other hand – considering that Alexander et al. (2005a) find that the majority of AGNs in SMGs are heavily obscured, with column densities of $N_H \gtrsim 10^{23}$ cm^{-2} – the presence of Compton-thick AGNs ($N_H \gtrsim 10^{24}$ cm^{-2}) without an X-ray AGN signature remains an important consideration (Alexander et al. 2008b). Furthermore, the number of SMGs with the necessary ultra-deep X-ray observations to reveal the presence of highly obscured AGN remain small ($\simeq 20$; Alexander et al. 2005a).

The presence of AGNs in SMGs suggests that AGN and starburst activity generally coexist within this population. This implies that part of the bolometric luminosity in SMGs may be reflecting SMBH growth rather than stellar buildup (Borys et al. 2005; Alexander et al. 2005a). Alexander et al. (2005a) report X-ray luminosities and spectral indices that suggest that even in the presence of an AGN, only $\lesssim 10\%$ of

the far-IR luminosity in SMGs can be attributed to them, supporting the claim that SMGs are dominated by star formation. However, the possibility of a small fraction of luminous, but Compton thick, AGN lurking within the SMG population remains an important consideration to take into account (see Coppin et al. 2008). At this stage, there is clearly uncertainty as to whether star formation or AGN activity is truly responsible for the bulk of the luminosity in the ensemble of the SMG population.

1.5.1 Mid-IR View of SMGs

The mid-IR emission of galaxies provides with a distinct insight that can unveil many astrophysical details of the radiation field harbored within and consequently about the nature of the dust-embedded power engine, be it AGN or star formation activity. With the advent of the *Spitzer* Space Telescope and with the unprecedented sensitivity of the onboard Infrared Spectrograph (IRS), the possibility has been opened to explore the mid-IR region of galaxies at high redshift.

In Chapters 2-3, I present an observing program that we have completed with *Spitzer* IRS to study the mid-IR properties of the largest sample of SMGs to date, with 24 radio-identified SMGs spanning the redshift range of $z \sim 0.6-3.2$. At mid-IR wavebands, emission arising from the dust itself provides an indirect insight into the illumination of the interstellar medium in SMGs and suffers from modest obscuration. It provides access to a number of mid-IR features, including silicate absorption, the emission from Polycyclic Aromatic Hydrocarbons – generally associated with intense star formation– and the warm/hot dust continuum emission – typically enhanced in the presence of an AGN. These features can be used to unveil details on the nature of the dust-enshrouded power engine: in particular, dust obscuration by silicates along the line of sight indicating the spatial extent of the mid-IR emission, the PAH-to-continuum strengths indicating the relative contributions from AGN and starburst activity, and the PAH relative strengths indicating properties of the ambient radiation field.

1.5.2 Long-Slit Near-IR Spectroscopy of SMGs

In Chapter 4 I discuss near-IR observations of five radio-identified SMGs at $z \sim 2$ with the Near-Infrared Spectrograph (NIRSPEC; McLean et al. 1998) on the Keck II Telescope, as part of a continuing program to build a large sample of SMGs with deep rest-frame optical spectroscopy (Swinbank et al. 2004). With these observations, we exploit line diagnostic in the rest-frame optical to: probe for the presence of AGNs through detection of broad emission lines; gauge metal enrichment; and measure offsets between the redshifts of UV and optical emitting gas.

Even with knowledge of the rest-frame UV redshifts from C05, acquiring spectroscopic redshifts for SMGs in the near-IR is extremely important. UV lines are typically subject to offsets that can reach up to $few \times 1000$ km s^{-1} with respect to Hα and molecular CO lines (Greve et al. 2005; Swinbank et al. 2004; Takata et al. 2006) and which arise from galactic outflows and winds that have been found to be significant in SMGs and other high-redshift galaxy populations (Adelberger et al. 2003). Even though these offsets provide valuable information about the winds in SMGs and their effect on potentially enriching the surrounding inter-galactic medium, rest-frame optical lines provide a more accurate redshift for the bulk of the gas in the interstellar medium and for the depth of the potential well of the galaxy.

1.5.3 A Near-IR Integral Field Spectroscopic View of SMGs

The absolute strengths and widths of rest-frame optical lines provide with powerful means of assessing SFRs, dynamical masses and the nature of the energy power sources. However, the presence of an AGN may enhance observed line kinematics, modify line ratios and boost absolute line emission fluxes. Having access only to the integrated flux over the portion of the galaxy that falls within the slit, NIRSPEC spectra face difficulties in disentangling the independent contributions from the AGN component and the star-forming regions, likely leading to incorrect and probable overestimates in SFRs and dynamical masses.

In Chapter 5 I present the integral field observations of Hα emission for three SMGs

with the OH-Suppressing Infrared Imaging Spectrograph (OSIRIS; Larkin et al. 2006) on the Keck II Telescope, used in conjunction with Laser-Guide Star Adaptive Optics (LGS-AO; Wizinowich et al. 2006; van Dam et al. 2006). The recent advent of OSIRIS provides a unique opportunity to probe the spatially-resolved two-dimensional spectra of the extended near-IR emission in SMGs, allowing us to discern between compact AGN and extended starburst components. Taking advantage of the kpc-scale spatial resolution we revisit estimates of dynamical mass and SFRs for the SMG population as represented by our sample. These estimates, critical for imposing constraints in current models of galaxy formation, had been in the past inevitably hampered by AGN contamination of emission lines in long-slit spectroscopic studies. Furthermore, we explore the dynamics of gas in the inner galaxy halo to improve our understanding on the internal dynamics of this enigmatic galaxy population.

Chapter 2

Mid-Infrared Spectroscopy of High-Redshift Submillimeter Galaxies: First Results

We present mid-infrared spectra of five submillimeter galaxies at $z = 0.65-2.38$ taken with the *Spitzer Space Telescope* [1]. Four of these sources, at $z \lesssim 1.5$, have strong features from Polycyclic Aromatic Hydrocarbons (PAHs) and their composite spectrum is well fitted by a starburst-dominated M82-like spectrum with an additional power-law component consistent with that expected from an AGN. Based on comparison with local templates of the 7.7 μm PAH equivalent width and the PAH-to-infrared luminosity ratio, we conclude that these galaxies host both star formation and AGN activity, with star formation dominating the bolometric luminosity. A single source at $z = 2.38$ displays a Mrk 231-type broad emission feature at rest-frame $\sim$8 μm that does not conform to the typical 7.7/8.6 μm PAH complex in starburst galaxies, suggesting a more substantial AGN contribution.

2.1 Introduction

It is over a decade since the discovery of a population of high-redshift galaxies identified through their submillimeter (submm) emission (Smail et al. 1997; Barger, Cowie & Sanders 1999; Eales et al. 1999; Bertoldi et al. 2000; Cowie et al. 2002; Scott et al.

[1] This chapter has been published in similar form as Menéndez-Delmestre et al. 2007.

2002; Borys et al. 2003; Webb et al. 2003a; Coppin et al. 2005; Younger et al. 2007). Their submm selection suggests that these are strongly starbursting systems. With implied star-formation rates (SFRs) of $\sim$ 100–1000 $M_{\odot}\,yr^{-1}$, these dust-enshrouded *submm* galaxies (hereafter, SMGs) may make a significant contribution to the global SFR density at $z \sim 2$–3 (C05). The absorbing dust that makes them such prodigious submm emitters also makes them quite optically faint and renders follow-up studies at shorter wavelengths challenging. The study of SMGs has been facilitated by the detection of a large fraction of them as μJy radio sources (Ivison et al. 2002) and more recently through millimeter-wave interferometry. This has allowed both the reliable identification of their counterparts (Smail et al. 2004), and subsequent measurement of their spectroscopic redshifts for fairly large samples (C05).

With a mean redshift of $<z>\sim 2.2$, the redshift distribution of the *radio-identified* SMGs in C05 coincides with the global peak epoch of quasar activity. The connection between SMGs and AGNs has been probed in recent near-IR and X-ray studies. Near-IR spectroscopy by Swinbank et al. (2004) show that broad Hα lines (FWHM $\gtrsim$ 1000 km s^{-1}) are often present in these galaxies, while deep X-ray studies using the sensitive *Chandra* Deep Field-North (CDF-N) Survey suggest that at least $\sim$28–50% of SMGs host an obscured AGN (Alexander et al. 2005a). A number of SMGs that display no AGN signatures in the rest-frame optical (Swinbank et al. 2004) were classified as AGNs based on X-ray observations (Alexander et al. 2005a). This is likely due to geometrical effects in which the broad-line region of the AGN remains hidden in the optical by intervening obscuring material. At high X-ray energies, direct X-ray emission is detectable through even very high column densities, allowing the direct detection of AGN at very high obscurations. However, Alexander et al. (2005a) find that the majority of AGNs in SMGs are more modestly obscured, with column densities of $N_H \sim 10^{23}$–$10^{24}\,cm^{-2}$. A similar mix of AGN and starburst activity is seen in local ultra-luminous infrared galaxies (ULIRGs; with total infrared luminosities, $L_{8-1000\ \mu m} \gtrsim 10^{12}$; Soifer et al. 1987; Sanders et al. 1988), most of which have been shown to be composite AGN–starburst systems (e.g., Armus et al. 2007). The SMGs have IR luminosities which are comparable to ULIRGs at low redshift,

prompting the question as to whether SMGs are high-redshift analogs of ULIRGs and hence whether we can learn about the physical processes within SMGs from studies of local ULIRGs (Tacconi et al. 2008).

The potential presence of luminous Compton-thick AGNs ($N_H \gtrsim 10^{24}\,cm^{-2}$) in the SMGs with no X-ray AGN signature remains a significant caveat to these results. Furthermore, the samples of SMGs with the necessary ultra-deep X-ray observations to reveal the presence of highly obscured AGN are small. Hence it is possible that a small fraction of luminous, but Compton thick, AGN lurk within the SMG population (see Coppin et al. 2008).

Rest-frame optical emission provides direct insight into the stellar emission and ionized gas of a galaxy, but suffers from obscuration due to intervening dust. At longer wavelengths, the mid-IR emission arising from the dust itself provides an indirect insight into the dust-enshrouded nature of SMGs and suffers from much less obscuration than the shorter, optical wavelengths. We therefore designed a program to follow up a large sample of 24 SMGs in the mid-IR using *Spitzer*'s Infrared Spectrograph (IRS; Houck et al. 2004) in an effort to answer the following questions for a large and representative sample of the SMG population: Are SMGs composite AGN–starburst systems? To what extent does AGN activity contribute to the total infrared output of these galaxies? Is there a spectrum of varying levels of AGN activity across the population? Are local ULIRGs good analogs for the mid-IR emission of SMGs?

The main components contributing to the mid-IR spectrum of a galaxy are: thermal dust continuum, emission from vibrational modes in PAH molecules and other atomic and molecular lines. The continuum emission at longer mid-IR wavelengths, $\lambda \gtrsim 12$ μm, arises from emission by very small grains (VSG; $\lesssim$ 10nm) of dust found around either obscured AGN or in star-forming regions. This is often referred to as the VSG continuum, or the *warm* dust continuum ($T_{Dust} \lesssim 250\,K$). At shorter wavelengths, $\lambda \lesssim 6$ μm, the continuum traces emission from dust heated to significantly hotter temperatures ($T_{Dust} \gtrsim 500\,K$) likely due to its close location near an AGN or possibly a hot, nuclear starburst region. This is what we refer to as the *hot* dust continuum. PAH molecules ($\lesssim$ few nm) consist of chained benzene rings, associated

hydrogen and other trace elements, such as Si and Mg. The line emission in the mid-IR waveband is dominated by PAH molecules which are excited by the UV photons that are copiously available in star-forming regions. The main PAH emission features arise from the bending and stretching of skeletal C-C or peripheral C-H bonds and are observed at rest-frame 6.2, 7.7, 8.6, 11.3, 12.7 and 17 μm (e.g., Draine & Li 2007). The strength of these features have been used in mid-IR surveys with the *Infrared Space Observatory* (ISO; Genzel et al. 1998; Rigopoulou et al. 1999; Tran et al. 2001; Laurent et al. 2000) to estimate the relative contributions of starburst and AGN for the brightest local galaxies (e.g., Rigopoulou et al. 1999). It has been shown locally that stronger PAH features are associated with regions of intense star formation (Helou 1999), while they are typically absent in powerful AGN (Voit 1992).

With the unprecedented sensitivity of *Spitzer* IRS, it has been possible to explore the mid-IR region of galaxies at high redshift down to continuum levels of $S_{24\ \mu m} \gtrsim 0.1$ mJy (e.g., Yan et al. 2005, hereafter Y05; Yan et al. 2007; Lutz et al. 2005, 2007; Desai et al. 2006; Rigopoulou et al. 2006; Teplitz et al. 2007). At lower redshifts, investigation of the mid-IR properties of local galaxies with IRS provide for a sample of detailed templates against which high-redshift sources can be compared (e.g., Spoon et al. 2004; Armus et al. 2004, 2006, 2007; Weedman et al. 2005; Brandl et al. 2006; Sturm et al. 2006; Desai et al. 2007). A wide range of mid-IR spectra has been uncovered for high-redshift sources, ranging from continuum-dominated spectra with no PAH features to PAH-dominated spectra (e.g., Weedman & Houck 2008). Between these two extremes there are a myriad of composite spectra displaying a significant continuum with superposed PAH features (e.g., Yan et al. 2007).

We have an IRS program to study the range of mid-IR properties of a sample of 24 high-redshift SMGs, using the radio-identified sample with spectroscopic redshifts compiled by C05. Here we present IRS spectra of the first five targets observed: four are at lower redshifts, with $z = 0.65 - 1.5$ (SMM J221733.12+001120.2, SMM J163658.78+405728.1, SMM J030227.73+000653.5, SMM J163639.01+405635.9), and one at $z = 2.38$ (SMM J163650.43.43 +405734.5). The spectra of the low-redshift targets cover wavelengths longwards of 10 μm and give insight into the longer mid-

IR emission from SMGs; the full sample is more focused on $z \sim 2$ SMGs and hence probes shorter rest-frame wavelengths (see Chapter 3). This preliminary sample is otherwise representative of the SMG population, in terms of bolometric luminosity, dust temperature and submillimeter-to-radio flux ratio.

2.2 Observations and Reduction

We observed each target using the low resolution Long-Low (LL) observing mode of IRS ($R \sim 57 - 126$) at two different nod positions for 30 cycles of 120s each. We cover rest-frame emission longwards of 6 μm to probe for PAH emission at 6.2, 7.7, 8.6 and 11.3 μm and for silicate absorption centered at 9.7 μm. The data for these first five SMGs were obtained between August 2005 and February 2006.

The data were processed using the Spitzer IRS S13 pipeline [2], which includes saturation flagging, dark subtraction, linearity correction, ramp correction and flat-fielding. With a slit size of $\sim 10.7 \times 168''$, IRS does not resolve the SMGs spatially, and the targets were treated as point sources throughout the data reduction and analysis. We performed additional reduction of the 2D spectra using IRSCLEAN [3] to remove rogue pixels, and relied on differencing between the nod positions to subtract the residual background. We used the SPitzer IRS Custom Extraction (SPICE) [4] software to optimally extract flux-calibrated 1D spectra, by taking a weighted average of profile-normalized flux at each wavelength to increase the S/N of these faint sources. A more detailed description of the observations, reduction and analysis of the entire IRS SMG program is included in Chapter 3.

[2] http://ssc.spitzer.caltech.edu/irs/dh/
[3] http://ssc.spitzer.caltech.edu/archanaly/contributed/irsclean
[4] http://ssc.spitzer.caltech.edu/postbcd/spice.html

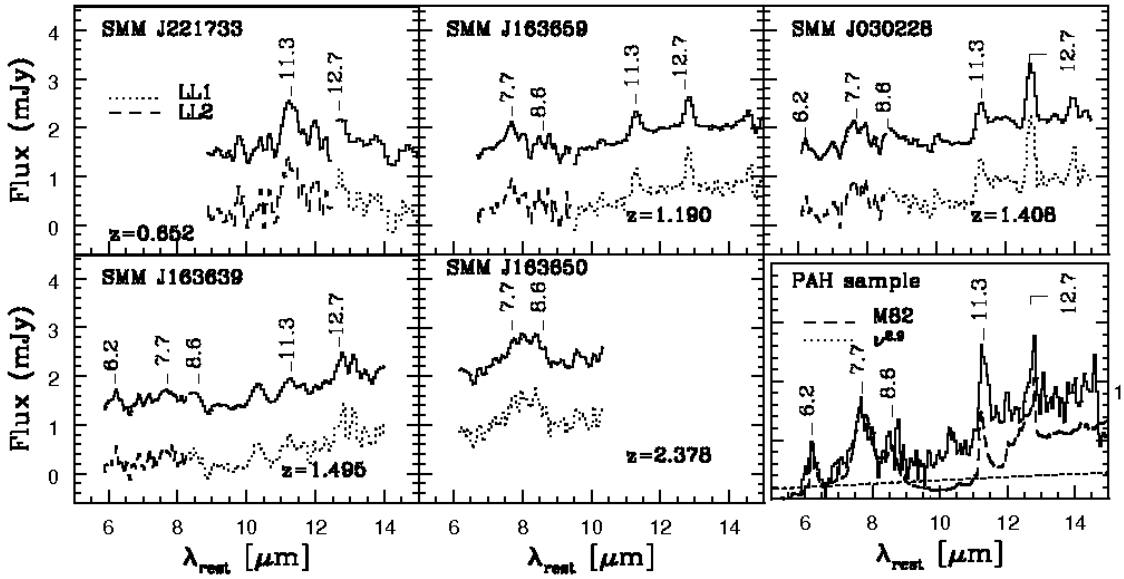

Figure 2.1 Flux-calibrated1D *Spitzer* IRS spectra of five SMGs and the composite spectrum of the PAH sample. For the five individual spectra, the lower curve represents the unsmoothed spectrum, with the first order (LL1: $\lambda_{obs} = 19.5 - 38$ μm) and second order (LL2: $\lambda_{obs} = 14 - 21.3$ μm) of the low-resolution mode shown in dotted and dashed lines, respectively. The upper curve shows the spectrum smoothed by three pixels and offset in flux for clarity. The various wavelengths of PAH emission features are indicated. We show the smoothed version of the composite spectrum for the PAH sample, together with the ISO SWS spectrum of M82 (dashed line), smoothed to the resolution of IRS and normalized to the 7.7 μm PAH feature. The excess in the SMG composite, when fitted by M82, is consistent with an additional power-law component emission from an AGN (dotted line; see §2.3.1.2).

2.3 Results and Discussion

The mid-IR spectra of the SMGs SMM J221733.12, SMM J163658.78, SMM J030227.73 and SMM J163639.01 show moderate to strong PAH features (see Fig. 2.1), and we refer to these targets collectively as the *PAH sample*. Detection of PAH emission is assumed to indicate the presence of starburst activity. At most a very shallow dip is present around 9.7 μm in the spectra, indicating little silicate absorption.

Our highest-redshift source, SMM J163650.43, is somewhat different to the other targets, with a broad emission feature at rest-frame $\sim$8 μm, unlike the typical blended PAH complex of the 7.7 and 8.6 μm features found in starburst galaxies. It is more reminiscent of the spectrum of Mrk 231 (Armus et al. 2007), which features an unabsorbed continuum sandwiched between absorption from silicates at longer wavelengths and from hydrocarbons at shorter ones (Spoon et al. 2004; Weedman et al. 2006). This suggests that SMM J163650.43 has more substantial AGN-activity than the SMGs in the PAH sample, consistent with the presence of a strong CIV (λ1549) feature at rest-frame UV (C05) and a broad Hα component ($\simeq 1753 \pm 238$ km s^{-1}; Swinbank et al. 2004), both revealing the unambiguous presence of an AGN. We discuss the properties of this source in more detail in Chapter 3 (Menéndez-Delmestre et al. 2008) and concentrate here on the median properties of the SMGs with clear PAH emission.

To get an insight into the physics inherent to SMGs in our PAH sample, we compare their spectra with extensively studied local templates: the AGNs Mrk 231 (Armus et al. 2007) and NGC 1068 (Sturm et al. 2000), the starburst M82 (Förster Schreiber et al. 2003) and the more luminous ULIRGs Arp 220 (Armus et al. 2007) and NGC 6240 (Armus et al. 2006). Arp 220 has been a favorite template for high-redshift SMGs (Pope et al. 2006; Kovács et al. 2006): it has strong PAH features, indicative of starburst activity, and a steep mid-IR continuum due to a heavily obscured nuclear component inferred to be responsible for the bulk of the IR luminosity (Spoon et al. 2004). AGNs have been identified in both merging components of NGC 6240 but a starburst dominates the total IR luminosity (Komossa et al. 2003).

A qualitative comparison of the spectra of our PAH sample with these templates rules out Mrk 231, NGC 1068 and Arp 220 as good matches, but the spectra are similar to those of M82 and NGC 6240. Similar results were found by Lutz et al. (2005), who detected strong PAH features in the spectra of two SMGs at $z \sim 2.8$ that were well fitted by an M82-type spectrum.

2.3.1 The Composite SMG Spectrum

We take advantage of the similarity between the spectra in the PAH sample and of our precisely known redshifts (C05) to double our S/N by constructing a composite spectrum by averaging the individual spectra (Fig. 2.1). We use the composite spectrum to make a preliminary assessment of the independent contributions of starburst and AGN activity in our PAH sample. Normalizing the local templates to the 7.7 μm peak in the composite spectrum, we find that the composite is well fitted at $\lambda \lesssim 9$ μm by the NGC 6240 and M82 spectra (Fig. 2.1). However, neither template provides a good fit to the composite spectrum at $\lambda \gtrsim 9$ μm: the continuum emission of NGC 6240 exceeds that of the composite spectrum at $\lambda \gtrsim 12$ μm, while the spectrum of M82 falls below it. No physically reasonable AGN component can be added to the NGC 6240 spectrum to produce a good fit to the composite spectrum at longer wavelengths. On the other hand, an M82-type spectrum plus a power-law continuum provides a good fit to the composite data at all wavelengths.

2.3.1.1 The Starburst Component

The 7.7 μm PAH feature is generally the most prominent in the mid-IR spectra of starburst galaxies. Its strength relative to the continuum, measured by the equivalent width (EW), can be used to evaluate the fractional starburst contribution to the total bolometric output, as the hot mid-IR continuum is enhanced significantly in the presence of an AGN. Starburst-dominated objects, such as M82 and NGC 6240, are characterized by larger PAH EWs than objects with a prominent AGN, such as Mrk 231.

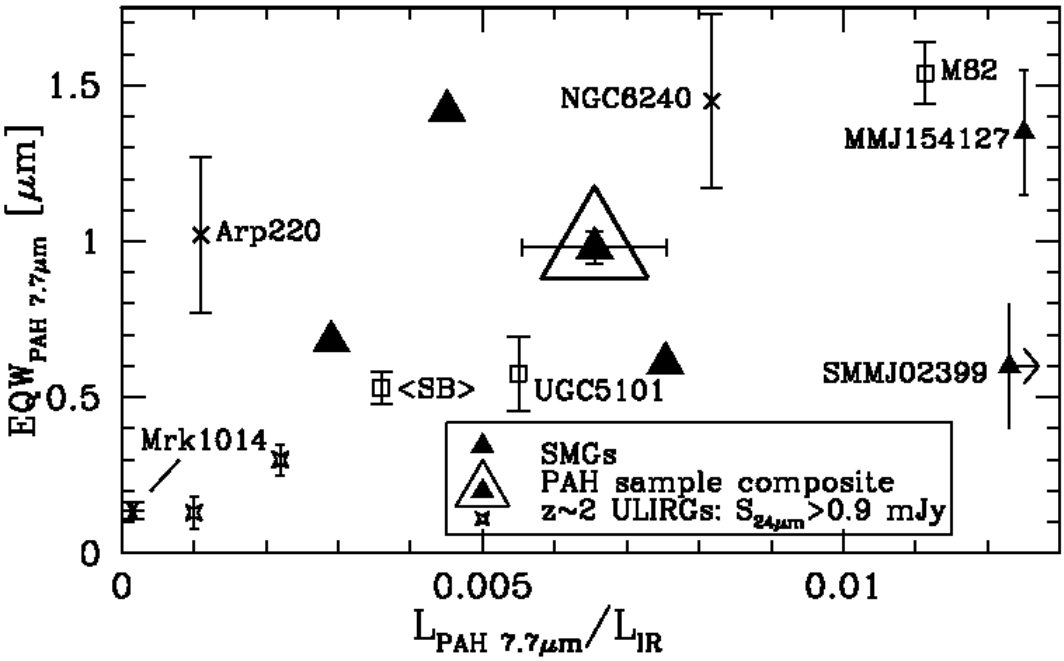

Figure 2.2 Relative strengths of the 7.7 μm PAH feature as measured by the PAH-to-IR ($8 - 1000$ μm) luminosity ratio and the rest-frame EW for the SMGs in the PAH sample (large triangles). We estimate the values for M82 (Förster Schreiber et al. 2003), Arp 220 (Spoon et al. 2004), NGC 6240 (Armus et al. 2006) and for the pair of SMGs in Lutz et al. (2005) (small triangles) directly from their published spectra assuming a linear continuum slope; the error bars reflect the uncertainties of this approach. We derive a lower EW for NGC 6240 than Armus et al. (2006), due to differences in continuum definition. Error bars for the Y05 sources, for the starburst-dominated UGC 5101 (Armus et al. 2004) and for the average of 13 nearby starburst galaxies studied with IRS (Brandl et al. 2006) reflect the uncertainties presented by the authors of the respective papers.

Measured EWs are sensitive to how the continuum is defined. We define a linear continuum by interpolating between two points clear of PAH emission, at 6.8 μm and 13.7 μm, or at 9 μm when the spectrum does not include one or other of these points. In Fig. 2.2 we plot the 7.7 μm rest-frame EWs and PAH-to-IR luminosity ratios for the SMGs in the PAH sample with 7.7 μm coverage and for the composite spectrum. The error in $L_{7.7\ \mu\mathrm{m}}/L_{8-1000\ \mu\mathrm{m}}$ for our SMG sample is dominated by a $\simeq 20\%$ uncertainty in the total IR luminosities (C05) [5]. We compare a number of low- and high-redshift sources, including two ULIRGs at $z \sim 2$ with clear PAH detections from the Y05 sample with $S_{24\ \mu\mathrm{m}} \gtrsim 0.9$ mJy, and two SMGs (SMM J02399−0136 with $S_{850\ \mu\mathrm{m}} = 23$ mJy and MM J154127+6616 with $S_{850\ \mu\mathrm{m}} = 14.6$ mJy) at $z \simeq 2.8$ (Lutz et al. 2005).

According to the line-to-continuum (l/c) diagnostic presented by Genzel et al. (1998), systems with $(l/c)_{7.7\ \mu m} \gtrsim 1$ are classified as starburst-dominated and those with $(l/c)_{7.7\ \mu m} < 1$, as AGN-dominated. With $(l/c)_{7.7\ \mu\mathrm{m}} \gtrsim 1$, starbursts appear to dominate in our PAH sample, that of Y05 and (Lutz et al. 2005). However, the distribution in 7.7 μm EW and PAH-to-IR luminosity ratio in Fig. 2.2 may suggest a distinction in the relative starburst-to-AGN contributions, with lower values of these parameters indicating a stronger AGN contribution. We distinguish three regions in Fig. 2.2: (1) a region with low PAH-to-IR luminosity ratios, occupied by Mrk 1014 (Armus et al. 2004) and the 24 μm-bright sample of Y05; (2) an intermediate PAH-to-IR luminosity region where NGC 6240 and the bulk of the SMGs in our sample are located; and (3) a region with the highest PAH-to-IR luminosity ratios, occupied by M82 and the two SMGs in Lutz et al. (2005).

At $z \sim 2$, the 24 μm flux traces 8 μm rest-frame continuum; a stronger hot mid-IR continuum (produced by an AGN) dilutes the strength of PAH features, leading to lower $L_{7.7\ \mu\mathrm{m}}/L_{8-1000\ \mu\mathrm{m}}$. The location of the Y05 sample in the plot could follow from the selection of 24 μm-bright targets ($S_{24\ \mu m} \gtrsim 0.9$ mJy) at this redshift, which would select objects with lower starburst-to-AGN ratios. SMGs in our sample have higher

[5] Kovács et al. (2006) show that SMGs fall below the local FIR-radio relation and thus the C05-derived $L_{8-1000\ \mu\mathrm{m}}$ values, which rely on this relation, are in average overestimated by a factor of ~ 2.

$L_{7.7\ \mu\mathrm{m}}/L_{8-1000\ \mu\mathrm{m}}$ ratios, similar to NGC 6240, which we interpret as an indication of a markedly stronger starburst contribution to the total luminosity than in the Y05 sample. With similar IR luminosities, the location of the SMG pair from Lutz et al. (2005) in this plot indicates that the 7.7 μm PAH feature is very strong. With large values for both the EW and the PAH-to-IR luminosity ratio, MM J154127 has been suggested to be dominated by starburst activity (Lutz et al. 2005). The large PAH-to-IR luminosity ratio for SMG SMM J02399 suggests strong starburst-activity; however, the relatively low EW value, together with the evident strong mid-IR continuum (see Fig. 2.1, Lutz et al. 2005) is consistent with this source having roughly equal AGN and starburst contributions.

The SMGs in our PAH sample have values of $\mathrm{EW}_{7.7\ \mu\mathrm{m}}$ and $L_{7.7\ \mu\mathrm{m}}/L_{8-1000\ \mu\mathrm{m}}$ that place their starburst-to-AGN ratio between that of the AGN-dominated ULIRG Mrk 1014 and the starburst M82. This is qualitatively similar to NGC 6240, which has both starburst and AGN components. As a caveat, we note that even though the 7.7 μm PAH-to-FIR luminosity ratio is associated with the starburst-to-AGN ratio, it is also sensitive to details of the SED of the system, such as the presence of multiple dust components at different temperatures and the amount of extinction (e.g., Arp 220; Spoon et al. 2004). This may explain the particularly high 7.7 μm PAH-to-IR luminosity ratio for SMM J02399.

2.3.1.2 The AGN Component

Mid-IR line diagnostics suggest that SMGs are starburst-like. The spectra of the starburst-dominated galaxies M82 and NGC 6240 provide a good fit to the composite spectrum at $\lambda \lesssim 9\ \mu$m; however, only an M82-type spectrum with an additional power law AGN component gives a good fit to the composite spectrum at all wavelengths. The power-law component is defined as $S_\nu \sim \nu^{-2.9}$, consistent with the range of IR spectral indices for 3C quasars in Simpson & Rawlings (2000).

From the power-law component flux at 10.5 μm we estimate the X-ray luminosity (L_X) using the correlation between $S_{10.5\ \mu\mathrm{m}}$ and $S_{2-10\mathrm{keV}}$ presented by Krabbe et al. (2001). This yields $L_X \sim 10^{44}\,\mathrm{erg\,s^{-1}}$ for an AGN at the average redshift for the SMGs

presented here, $z \sim 1.4$, in reasonable agreement with the X-ray luminosities found for the SMGs in Alexander et al. (2005a). Following their approach, we compare the average X-ray-to-far-IR ratio of the SMGs in the PAH sample with the typical ratio for quasars and find that the residual flux is consistent with an underlying AGN contributing in the order of ∼10% to the total far-IR emission. This agrees with their result that AGN activity is often present in SMGs but does not dominate the energetics. Since the 10.5- μm excess is dominated by lower redshift sources, further SMGs at $z \lesssim 2$, included in Chapter 3 (Menéndez-Delmestre et al. 2008), will better constrain this excess.

2.4 Conclusions

We present first results of a *Spitzer* IRS program to characterize the mid-IR spectra of high redshift SMGs. We compare the spectra to well-studied local templates and find that SMGs have starburst mid-IR spectra more like M82 than the often quoted local analog Arp 220. The composite spectrum of the SMGs in the PAH sample is well fitted by an M82-like starburst-component with a power-law continuum most likely representing a fainter underlying AGN. This similarity to the M82 spectrum suggests that the chemistry of the interstellar medium and radiation fields in these systems may be understood by looking at local galaxies in detail. Analysis of the 7.7 μm equivalent widths and PAH-to-IR luminosity ratios show that SMGs are markedly different from the other 24 μm-selected samples, such as the ULIRGs at $z \sim 2$ (Y05), which have stronger AGN contributions. This work provides further evidence that SMGs host both star formation and AGN activity, but that star formation dominates the bolometric luminosity, reiterating the role of SMGs as the build-up sites for a significant fraction of the stellar content we see today.

An advantage of this sample is that by probing the lower-redshift end of the C05 SMG sample distribution it provides rest-frame wavelength coverage longwards of 9 μm to assess better the AGN contribution. The SMG at $z = 2.38$, with a redshift closer to that of a typical C05 SMG, displays a potentially more AGN-dominated

Mrk 231-type SED, with a broad emission feature at rest-frame ~ 8 μm. The difference in AGN contributions within our preliminary sample suggests an increasing relative AGN-activity in SMGs at higher redshifts, probably due to the 24 μm-based selection of targets. The full sample, with a more extended redshift distribution, will provide us with additional valuable information concerning the typical SMG population.

Acknowledgements We thank the Spitzer Science Center staff for their support, particularly Patrick Ogle for his help in the optimization of the spectral extraction. This work is based on observations made with the Spitzer Space Telescope, which is operated by the Jet Propulsion Laboratory, California Institute of Technology under a contract with NASA. Support for this work was provided by NASA through an award issued by JPL/Caltech.

Chapter 3

Mid-Infrared Spectroscopy of Submillimeter Galaxies: Extended Star Formation in Massive High-Redshift Galaxies

We have completed an observing program with *Spitzer* IRS to study the mid-IR properties and investigate the energetics of 24 SMGs [1]. This program comprises the largest sample of SMGs observed with *Spitzer* IRS and covers the full extent of properties of the radio-identified population of SMGs in the redshift range of $z \sim 0.65$–3.2. We observe broad PAH emission features in more than 80% of our sample. We find that the median mid-IR spectrum is well-described by a starburst component with an additional power law, $F_\nu \sim \nu^{-2}$, likely representing a $\lesssim 35\%$ AGN contribution to the bolometric luminosity. Our results thus confirm that even in the case of SMGs with a significant AGN contribution revealed at other wavelengths, starburst activity dominates the bolometric luminosity. We find that SMGs show weaker silicate absorption at ~ 9.7 μm than local ULIRGs. This implies that the continuum and PAH emitting regions of the SMGs are less obscured than in similarly luminous local ULIRGs. We interpret this as evidence for a more extended distribution of cool and warm dust in SMGs compared to the more compact starbursts in local ULIRGs. We also find stronger 6.2 μm PAH emission in SMGs (relative to the 7.7 μm PAH feature) than in local starbursts. These results suggest that SMGs are not simply high-redshift

[1] This chapter has been submitted to ApJ in similar form as Menéndez-Delmestre et al. 2008.

analogs of either local ULIRGs or nuclear starbursts, but instead they appear to have star formation which resembles that seen in less-extreme star-forming environments at $z \sim 0$ – suggesting their intense activity is distributed across a far larger region than the $\sim$ 1-kpc nuclear bursts in local ULIRGs.

3.1 Introduction

In Chapter 2 we presented the *Spitzer* IRS results for the first five SMGs observed in the program (Menéndez-Delmestre et al. 2007), which complemented earlier IRS results for two SMGs at $z \sim 2.8$ presented by Lutz et al. (2005). Since then, Valiante et al. (2007) and Pope et al. (2008) obtained IRS spectra of nine SMGs in blank field and cluster lens surveys and of 13 SMGs from the GOODS-North Field, respectively. Here we present our results for our full sample of 24 SMGs, comprising the largest sample of SMGs observed to date with *Spitzer* and nearly doubling the number of SMGs observed with IRS. We discuss our sample selection and observing strategy in §3.2. The steps comprising the reduction and analysis of the spectra are discussed in §3.2 and §3.3. Our results are presented in §3.4 and discussed in detail in §3.5. We assume a ΛCDM cosmology, with $H_0 = 71\,\mathrm{km\,s^{-1}\,Mpc^{-1}}$, $\Omega_M = 0.27$ and $\Omega_\Lambda = 0.73$.

3.2 Observations and Reduction

The SMGs in our program were selected from the sample of 73 spectroscopically-confirmed, radio-identified SMGs in C05. We aimed for full coverage of the range in redshifts, radio, submm and total IR luminosities present in the C05 sample (see Fig. 3.1) to build a sample representative of the radio-identified SMG population in general. We note that several of the SMGs from the C05 spectroscopic sample fall in the GOODS-North region and were included in the IRS studies focused on that field (Pope et al. 2008). Together with our sample, these are effectively part of a larger IRS study of the C05 survey which covers a total of 33 SMGs (or 45% of the parent C05 sample).

Table 3.1. Summary of *Spitzer* IRS Observations

Name	R.A.[a] ($h\,m\,s$)	Dec. ($^\circ\,'\,''$)	z^b_{opt}	Date	LL1 (ramp [s] × cycles)	LL2 (ramp [s] × cycles)
SMM J030227.73	03 02 27.73	+00 06 53.5	1.408	Jan. 2006	120 × 30	120 × 30
SMM J030231.81	03 02 31.81	+00 10 31.3	1.316	Feb. 2006	120 × 30	120 × 30
SMM J105151.69	10 51 51.69	+57 26 36.0	1.147	May 2006	120 × 30	120 × 30
SMM J105158.02	10 51 58.02	+57 18 00.3	2.239	May 2006	120 × 30	–
SMM J105200.22	10 52 00.22	+57 24 20.2	0.689	May 2006	120 × 30	120 × 30
SMM J105227.58	10 52 27.58	+57 25 12.4	2.142	May 2006	120 × 30	–
SMM J105238.19	10 52 38.19	+57 16 51.1	1.852	May 2006	120 × 30	120 × 30
SMM J105238.30	10 52 38.30	+57 24 35.8	3.036	May 2006	120 × 30	–
SMM J123549.44	12 35 49.44	+62 15 36.8	2.203	May 2006	120 × 30	–
SMM J123553.26	12 35 53.26	+62 13 37.7	2.098	May 2006	120 × 30	–
SMM J123707.21	12 37 07.21	+62 14 08.1	2.484	May 2006	120 × 30	–
SMM J123711.98	12 37 11.98	+62 13 25.7	1.992	May 2006	120 × 30	120 × 30
SMM J123721.87	12 37 21.87	+62 10 35.3	0.979	May 2006	120 × 30	120 × 30
SMM J163639.01	16 36 39.01	+40 56 35.9	1.495	Aug. 2005	120 × 30	120 × 30
SMM J163650.43	16 36 50.43	+40 57 34.5	2.378	Sept. 2005	120 × 30	–
SMM J163658.78	16 36 58.78	+40 57 28.1	1.190	Sept. 2005	120 × 30	120 × 30
SMM J221733.02	22 17 33.02	+00 09 06.0	0.926	June 2006	120 × 20	120 × 30
SMM J221733.12	22 17 33.12	+00 11 20.2	0.652	Nov. 2005	120 × 15	120 × 15
SMM J221733.91	22 17 33.91	+00 13 52.1	2.555	June 2006	120 × 30	–
SMM J221735.15	22 17 35.15	+00 15 37.2	3.098	June 2006	120 × 30	–
SMM J221735.84	22 17 35.84	+00 15 58.9	3.089	June 2006	120 × 30	–
SMM J221737.39	22 17 37.39	+00 10 25.1	2.614	June 2006	120 × 30	–
SMM J221804.42	22 18 04.42	+00 21 54.4	2.517	June 2006	120 × 30	–
SMM J221806.77	22 18 06.77	+00 12 45.7	3.623	June 2006	120 × 30	–

[a] Radio position from C05 compilation.

[b] Spectroscopic redshifts from C05.

While we aimed to span the full range in multi-wavelength properties of radio-identified SMGs, to have a realistic chance of detecting the galaxies with IRS we selected the 24 SMGs with the highest estimated 24 μm fluxes.[2] As 24 μm observations were not available at the time of the proposal, we estimated 24 μm fluxes for the SMGs in C05 from fitting the SEDs to the radio (1.4 GHz), submm (850 μm) and available optical photometric data points (see C05 and references therein). We note that selection of 24 μm-bright sources (albeit estimated) may introduce a two-sided selection effect. Selection based on bright 24 μm-fluxes will preferentially pick out the hot dust emission in AGNs. However, at redshifts $z \sim 2$, the 7.7 μm-PAH feature is redshifted onto the 24 μm band: this is a prominent emission feature, associated with star-formation activity and will result in a boosted 24 μm flux. We discuss this potential selection bias in more detail in §3.4.5. From a parallel mid-IR imaging survey of the radio-identified SMGs in C05 with the Multiband Imager for *Spitzer* (MIPS) by Hainline et al. (2009) our IRS subsample has MIPS 24 μm band fluxes in the range $S_{24\ \mu\mathrm{m}} \sim 0.09$–$0.85$ mJy with a median value of $< S_{24\ \mu\mathrm{m}} >= 0.33 \pm 0.18$ mJy.

The details of our observations are summarized in Table 3.1. We observed all our targets using the low-resolution ($R \sim 57$–126) Long-Low (LL) observing module of IRS. The slit width for this module is $\sim 10.7''$, which corresponds to roughly 100 kpc at $z \sim 2$, and so each target is fully enclosed in the observed slit and is thus treated as a point source. With shared coverage of the first LL order (LL1: 19.5–38.0 μm) and the second LL order (LL2: 14.0–21.3 μm) we aimed to cover rest-frame emission longwards of 6 μm to search for PAH emission and for any silicate absorption at 9.7 μm. With a redshift range of $z = 0.65$–3.2 for the full sample, the LL1 IRS module alone provides the relevant coverage for SMGs with $z \gtrsim 2.2$; while the LL2 module is also required for SMGs with $z \lesssim 2.2$. We observed each target at two different nod positions for a total integration time of 1–2 hours with each module. The data were obtained between August 2005 and June 2006.

[2]We used the online tool SPEC-PET to calculate estimated S/N for galaxies according to the estimated $S_{24\mu\mathrm{m}}$ value (http://ssc.spitzer.caltech.edu/tools/specpet/).

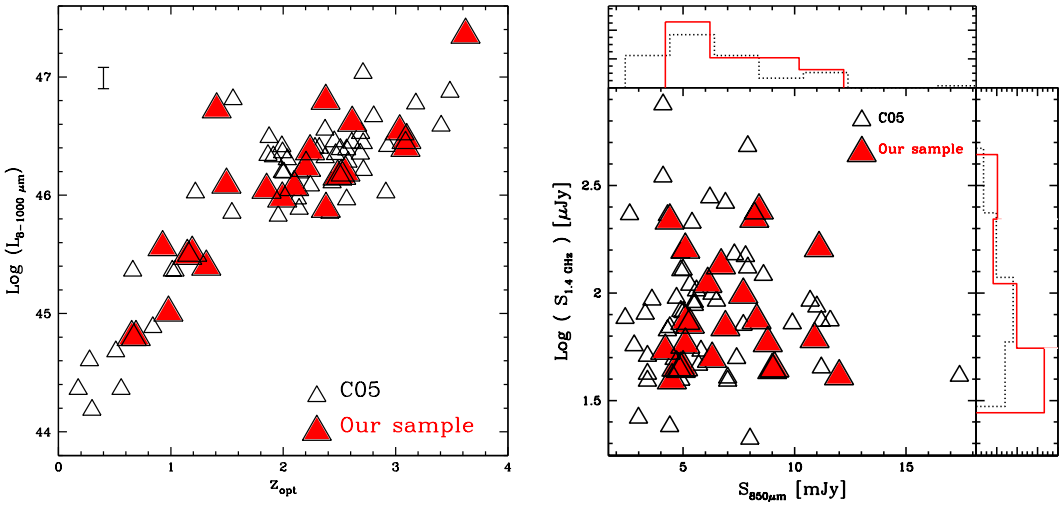

Figure 3.1 (**Left:**) The distribution of redshifts and IR luminosities (8–1000 μm) of the parent sample of radio-identified SMGs compiled by C05 with our IRS subsample highlighted. We plot a representative error on the IR luminosities. (**Right:**) The distribution of radio and submillimeter fluxes for the full C05 sample and those in the subsample observed with IRS. The histograms show the cumulative distribution of the full sample and the IRS subsample. These plots demonstrate that the IRS sample is representative of the parent sample of radio-identified SMGs, covering the full range in radio and submm properties, redshift and IR-luminosity.

We reduced the data using the *Spitzer* IRS S14 pipeline.[3] To ensure homogeneity throughout the sample, we reprocessed the raw data from our earlier results (Menéndez-Delmestre et al. 2007), which had been processed by the S13 pipeline. We performed additional cleaning of the 2D spectra using the *SSC* utility IRSCLEAN [4] to remove rogue pixels, by creating a mask for each Astronomical Observing Request (AOR). We use the rogue pixel mask associated with the observing cycle as a base and then identify additional deviant pixels in a *superdroop* file resulting from the averaging of all droop files within a single AOR. We relied on differencing between the two nod positions to subtract the residual background. To do this, we median-combined all cycles for science images with the same module order (LL1 or LL2) and nod position. For each module order, we then subtracted the median of all science images at one nod position from that of the other nod position.

For each LL order, we used the SPitzer IRS Custom Extraction [5] (SPICE) software to extract flux-calibrated 1D spectra from each 2D sky-subtracted median-combined nod. We used the *optimal extraction* mode recently included in SPICE. Optimal extraction entails taking a weighted average of profile-normalized flux at each wavelength to increase the S/N in IRS observations of faint sources (Horne 1986; Narron et al. 2006). Flux calibration is based on observations of a standard star during the same observing cycle as the science observations and has a 10% uncertainty (see IRS Data Handbook [6] for details). The SPICE-extracted 1D spectra for the different nods within one LL order were then median-combined. We combined the orders using IRAF to produce a final spectrum for each target, excluding the noisy edges at $\lambda_{obs} \lesssim 14.2$ μm and $\lambda_{obs} \gtrsim 35$ μm. The resulting spectra are shown in Fig. 3.2.

[3] http://ssc.spitzer.caltech.edu/irs/dh/
[4] http://ssc.spitzer.caltech.edu/archanaly/contributed/irsclean
[5] http://ssc.spitzer.caltech.edu/postbcd/spice.html
[6] http://ssc.spitzer.caltech.edu/irs/dh/

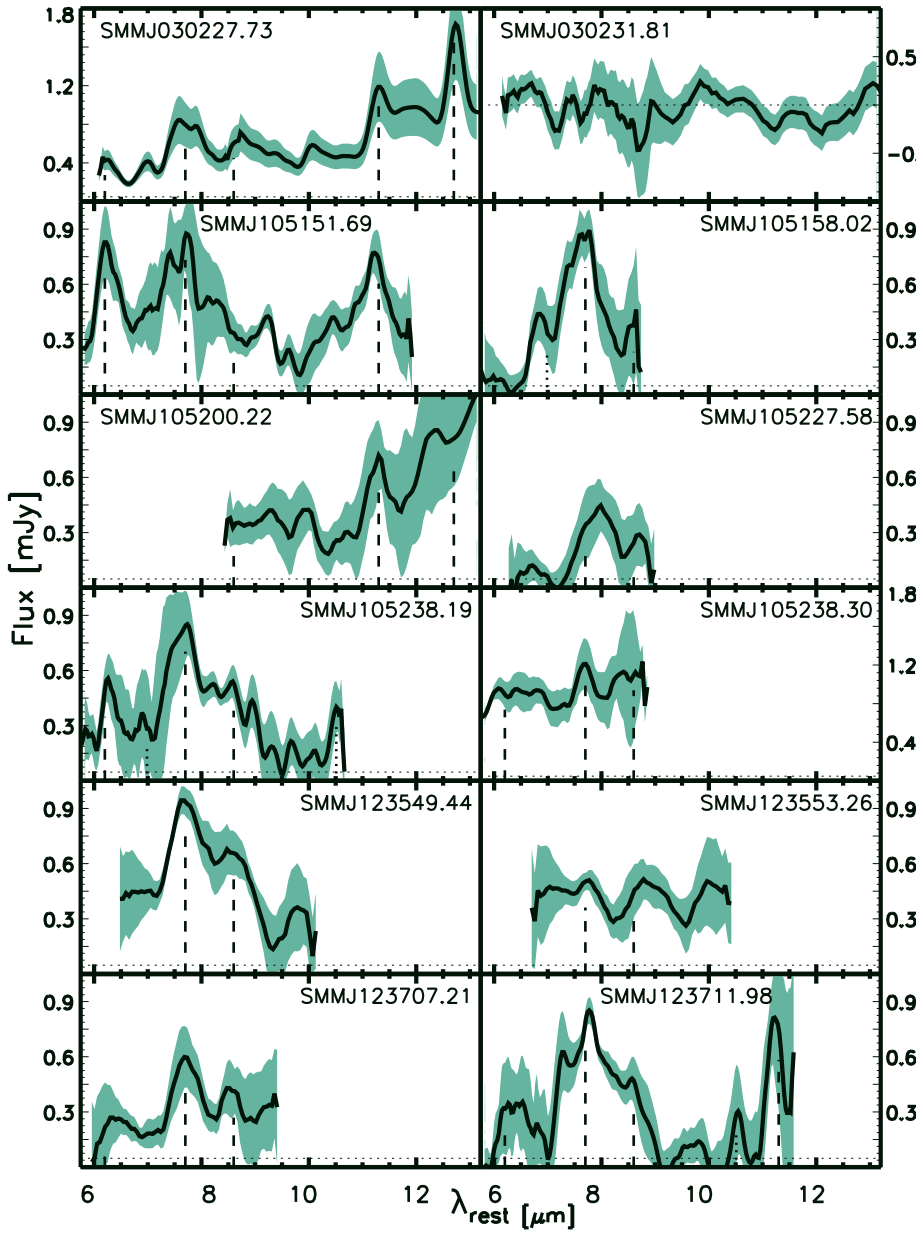

Figure 3.2 The rest-frame mid-IR spectra of all 24 SMGs in our sample, smoothed to the instrument resolution ($\Delta\lambda \sim 0.3$ μm at $\lambda \sim 24$ μm). The zero level for each spectrum is denoted by a horizontal short-dashed line and the shading represents the flux uncertainty, as given by SPICE. We do not detect SMM J030231.81. The locations of PAH features at 6.2, 7.7, 8.6, 11.3 and 12.7 μm are indicated by the dashed lines and these features are visible in a large fraction of our sample. The position of tentative narrow line emission from [ArII] (6.99 μm) and/or [SiV] (10.51 μm) are shown by dotted lines in SMM J105158.02, SMM J105238.19, SMM J123711.98, SMM J123721.87, SMM J163639.01, SMM J221733.91 and SMM J221735.15.

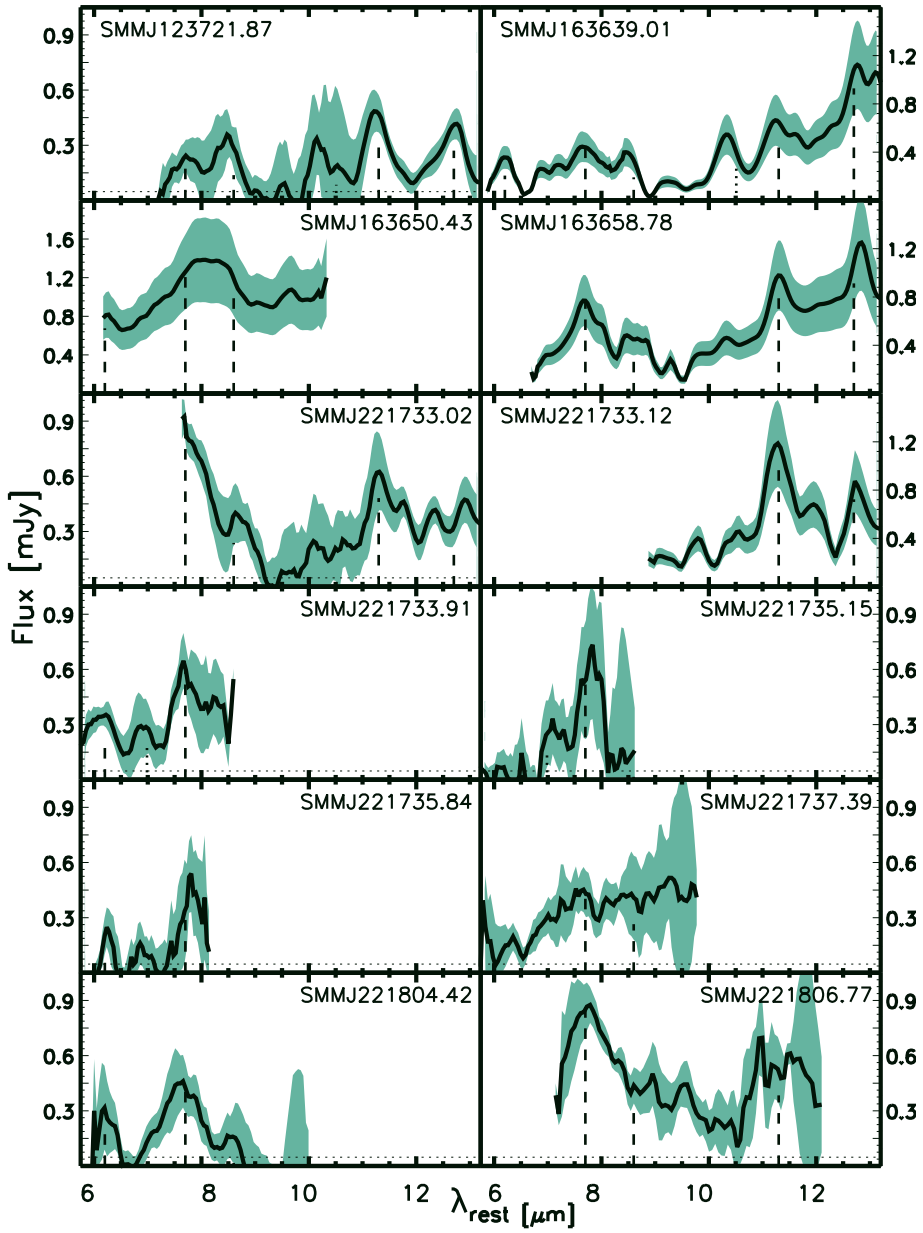

Fig. 3.2. — Continued.

3.3 Analysis

The spectra in Fig. 3.2 show a range of emission and absorption features. One of the key advantages of our survey over previous studies is the availability of spectroscopic redshifts for the entire sample from C05. With spectroscopic redshifts in hand, we have a priori knowledge of the observed wavelengths where emission and absorption features are expected. We therefore identified PAH features, silicate absorption centered at ~ 9.7 μm and a number of possible forbidden narrow emission lines, such as [ArII] (6.99 μm) and [SIV] (10.51 μm). We see that a large fraction of our sample show PAH emission and we mark these and the other spectral features on Fig. 3.2.

To derive quantitative estimates of the strength of the emission and absorption features and determine their precise wavelengths we need to fit the spectra. However, given our modest integration times (Table 3.1), we reach a signal to noise (S/N) of only 1–5 in the continuum emission at 24 μm [7]. At this S/N we found that intricate spectral fitting programs (e.g., PAHFIT; Smith et al. 2007) are not appropriate. We thus adopted a simple and straight-forward fitting approach which we describe below.

The measurements of the fluxes and EWs of features in the spectra required that we first determine the continuum level for each spectrum before measuring the strength of each individual emission and absorption feature. The resulting EW and flux measurements are extremely sensitive to the fitting method selected, particularly in the determination of the continuum level. A number of alternative fitting methods have been used by different authors, making a fair comparison of PAH strengths in different samples a rather subjective and delicate issue, as discussed by Sajina et al. (2007). In particular, the prevalence of interactive fitting methods has further complicated the reproducibility of mid-IR properties between samples. Hence in this work we have adopted a method of continuum and PAH fitting that ensures complete reproducibility. Moreover, in order to make fair comparisons between the SMGs in our sample and other low- and high-redshift sources, we have re-measured all the mid-IR features in all of these samples using our method. We have applied our method

[7] S/N was determined within a λ-window of $\Delta\lambda \sim 1.4$ μm on the individual nod-subtracted 2D spectra

to select local ULIRGs from the Bright *IRAS* sample studied by Armus et al. (2006, 2007) and Desai et al. (2007), the low-redshift nuclear starburst-dominated galaxies presented by Brandl et al. (2006) and the mid-IR selected high-redshift sources of Sajina et al. (2007). As we noted earlier, we have also included in our comparisons the 13 SMGs in the GOODS-North field studied by Pope et al. (2008), nine of which have optical redshifts measured by C05 and thus naturally complement our sample.

The thermal mid-IR continuum, arising either from starburst or AGN activity can be described by a power-law, $S_\nu \sim \nu^{-\alpha_{\rm MIR}}$, where the value of the power-law index $\alpha_{\rm MIR}$ gives an indication of the steepness of the spectrum. Flatter mid-IR continua with low power-law indices ($\alpha_{\rm MIR} \lesssim 0.5$) are usually associated with unobscured AGNs, where emission from the hot dust close to the AGN is readily observed. Steeper continua ($\alpha_{\rm MIR} \gtrsim 0.5$) are on the other hand associated with starburst activity, but can also be found in dust-obscured AGNs. Hence we determined the power-law continuum index $\alpha_{\rm MIR}$ for the spectra in our sample to: (1) characterize the continuum slope and investigate the underlying energetics, and (2) to define the continuum level on which PAH emission features are superimposed.

To determine $\alpha_{\rm MIR}$ we use the χ^2 minimization IDL routine LINFIT to obtain the best linear fit to each SMG spectrum in $\log(S_\nu)$–$\log(\nu)$ space (see Fig. 3.3). We first obtain the best linear fit to each full spectrum and calculate the rms in the (original − fit) residual spectrum. Then, we identify those wavelength regions in the original spectrum where the data points lie more than 1× the rms away from this first linear fit. In this way, we automatically identify the wavelength regions where emission and absorption features are present. We then perform a second round of linear fitting, where we exclude these regions from the fit. We adopt the results of this second fit as our final continuum, with the influence of emission and absorption features minimized. The uncertainty in the continuum level is established considering the flux uncertainty given by SPICE for each individual spectrum. These flux uncertainties propagate into an uncertainty of $\sim 20\%$.

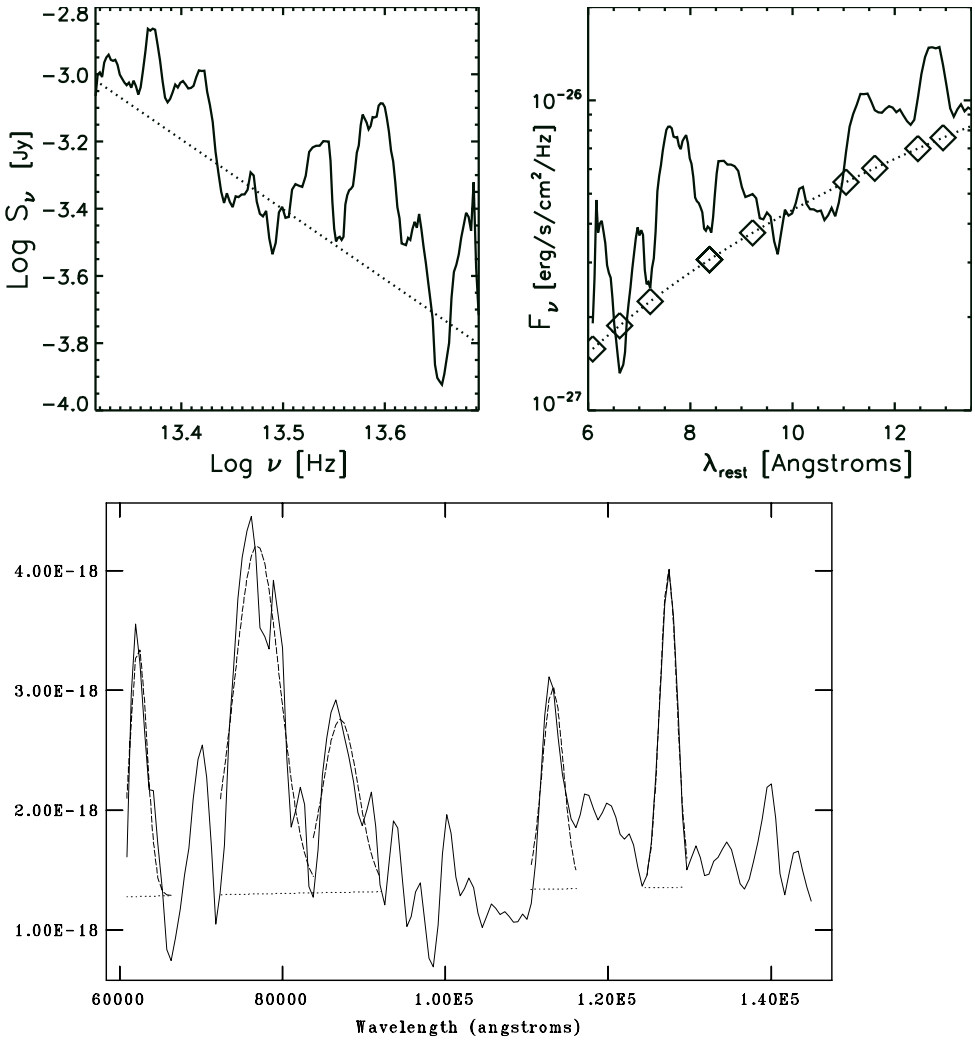

Figure 3.3 (**Top Left:**) Sample spectrum in $Log[S_\nu] - Log[\nu]$ space that illustrates our approach to continuum determination. The solid line is the spectrum of SMM J030227.73 and the dotted line is the best fit continuum determined through the method described in §3.3. (**Top Right:**) For each PAH feature, we defined a fitting window covering a narrow wavelength range centered at the expected central PAH wavelengths ($6.22, 7.598, 8.61, 11.33, 12.62$ μm; Draine & Li 2007). The edges of these fitting windows are denoted in this figure by open diamonds on the spectrum. (**Bottom:**) Mid-IR spectrum of SMM J030227.73 with flux expressed in units of λS_λ. The gaussian fit for each PAH feature is shown as dashed curves.

Having determined the continuum, we search for the presence of PAH emission features at 6.2, 7.7, 8.6, 11.3 and 12.7 μm. Since our targets have a range in redshift, $z \sim 0.65$–3.2, the wavelength coverage varies from 6–22 μm for the lowest redshift SMGs to 4.2–8.3 μm for the highest redshift. Out of all detected SMGs in our sample, 90% include coverage of the 7.7 μm region of the spectrum, thus providing a large sample of 20 SMGs to investigate the spectral features within this important wavelength region. We define a wavelength window around each spectral feature and use the IRAF task SPLOT to fit the PAH features with individual gaussians, where the center and FWHM are left as free parameters within the fitting window. We create a cursor file specifying the fitting windows and continuum level for each spectrum to automate the fitting process and thus avoid the lack of reproducibility inherent to other interactive fitting tasks. The wavelength regions used to fit the 6.2, 7.7, 8.6, 11.3 and 12.7 μm PAH features were approximately 6.026–6.617, 7.031–8.302, 8.242–8.922, 10.813–11.812, 12.409–13.029 μm, respectively (see Fig. 3.3). We adopt the SPLOT output uncertainties in the resulting EWs and luminosities, which account for the noise level present in the spectra. These errors are indicated in Table 3.2 and correspond to an average uncertainty of $\sim 30\%$. We derive a redshift associated with each PAH feature from its observed central wavelength. The final PAH-based redshift for spectra displaying multiple PAH features corresponds to the weighted mean of the redshifts derived from the individual PAH features, where the weights are provided by the PAH fitting uncertainties.

Finally, to determine the depth of the silicate absorption, we define the optical depth as $\tau_{9.7\ \mu\mathrm{m}} = \log_{10}[S_{cont}/S_{obs}]$, where S_{obs} is the flux level observed at 9.7 μm and S_{cont}, the interpolated flux of continuum in the absence of any absorption. We measure the latter from our power law continuum fit. The EWs and fluxes for PAH emission and absorption features we derive are listed in Table 3.2.

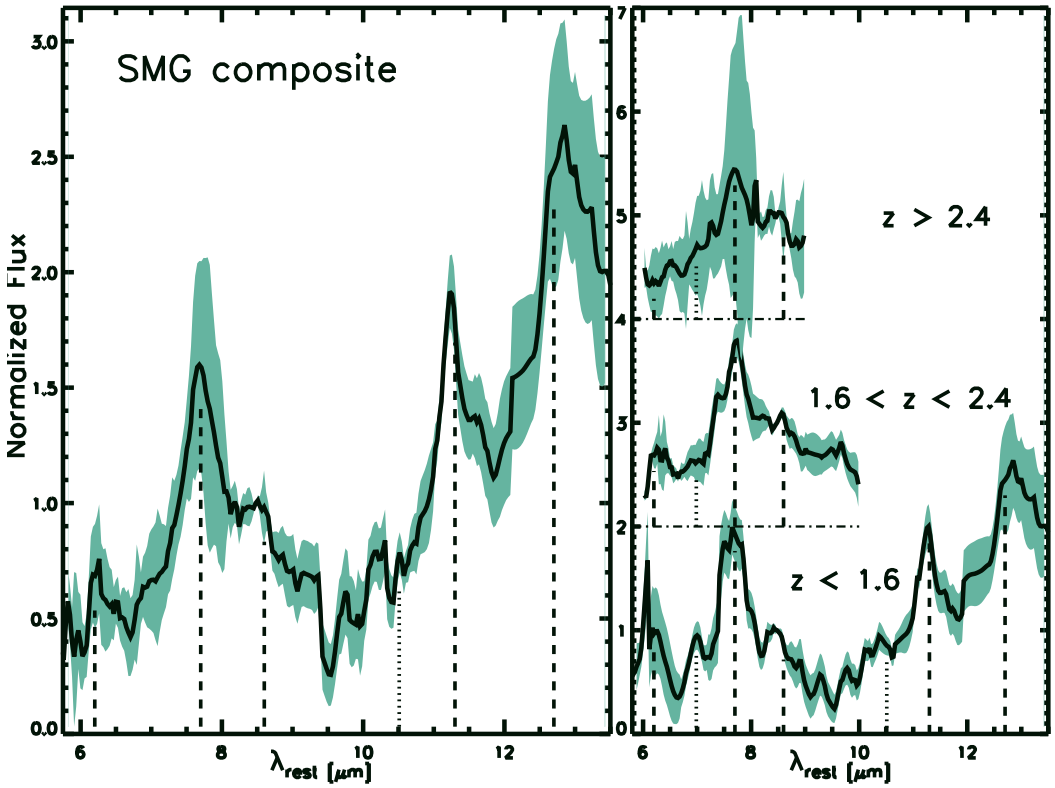

Figure 3.4 (**Left:**) The median-combined rest-frame composite spectrum of 22 SMGs detected in our sample, with the shaded area representing the 1-σ sample standard deviation. We assume optical redshifts (C05), except for the five SMGs in which PAH features suggest an alternate redshift (see Table 3.2). The composite spectrum is dominated by strong PAH emission at 6.2, 7.7, 8.6, 11.3 and 12.7 μm, with an underlying red continuum. All the spectra are normalized by their flux at $\lambda = 8.5\,\mu$m in the rest-frame (see §3.3.1 for details). (**Right:**) Composite spectra for subsets of SMGs in three separate redshift bins, where the zero level of each spectrum is denoted by a dash-dotted horizontal line. These demonstrate that at $\lambda > 10$ μm our composite spectrum is dominated by sources at $z < 1.6$.

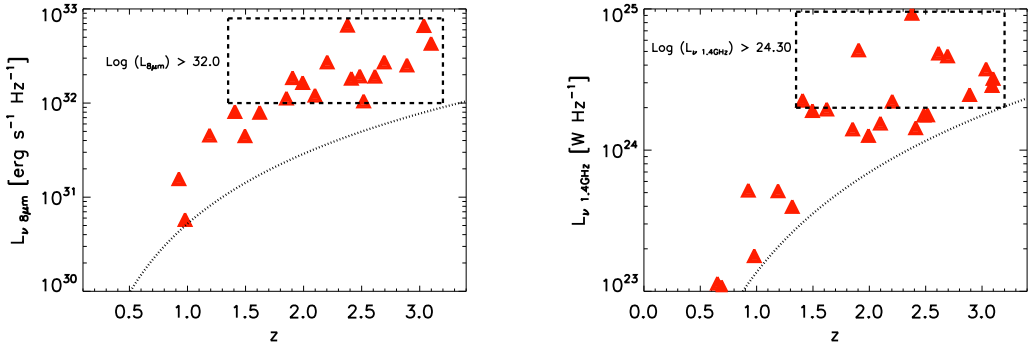

Figure 3.5 (**Left:**) Rest-frame 8 μm luminosity, measured from rest-frame IRS spectra, as a function of redshift for the SMGs in our sample. The dotted curve represents the lowest 8 μm luminosity accessible to *Spitzer* IRS at each redshift, assuming a flux sensitivity of $S_{24\ \mu\mathrm{m}} \sim 0.2\,\mathrm{mJy}$. The dashed box denotes the luminosity-complete subsample of SMGs with $\mathrm{L}_{8\ \mu\mathrm{m}} \gtrsim 10^{32}$ erg s^{-1} from which we build composite spectra based on 24 μm-brightness. (**Right:**) Similar plot for the rest-frame radio luminosity density at 1.4 GHz for the SMGs in our sample. The dotted line represents the 3-σ flux sensitivity ($\sim$ 30 μJy) of the radio observations discussed in C05. The dashed box encloses the SMGs with $\mathrm{L}_{1.4GHz} \gtrsim 2 \times 10^{24}$ erg s^{-1} Hz^{-1} that comprise the radio-luminosity-complete sample used to create SMG composites based on radio-brightness. See §3.3.1 for details.

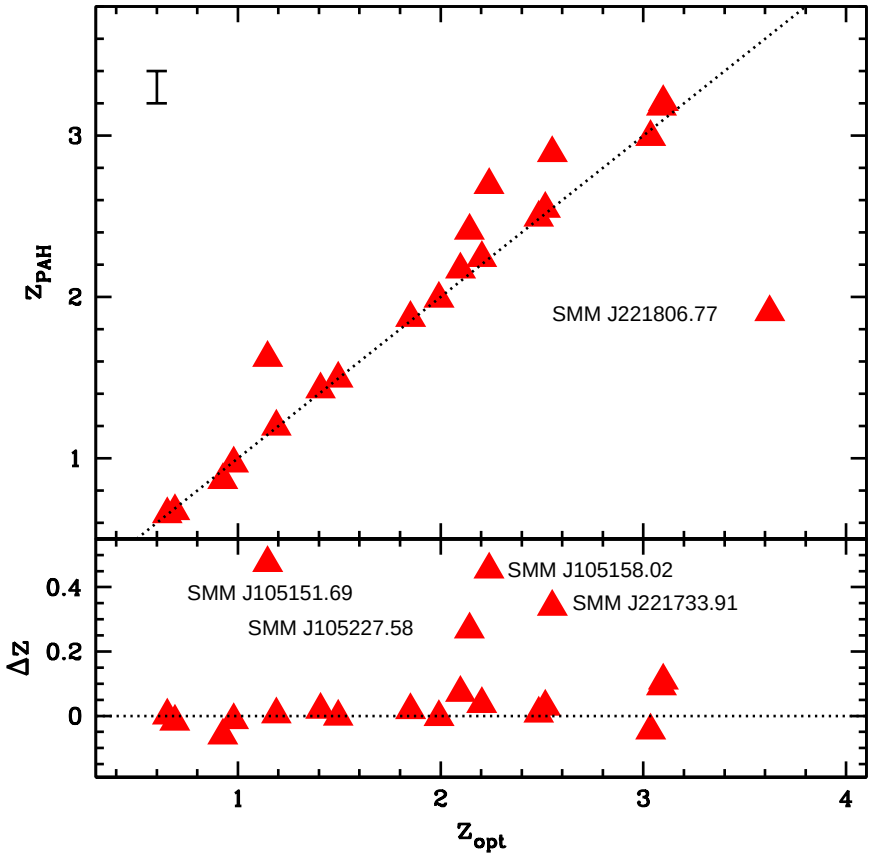

Figure 3.6 A comparison of the PAH-derived redshifts with the rest-frame UV redshifts for the SMGs in our sample (C05). Five out of the 23 detected SMGs have multiple PAH features that suggest a redshift significantly different from the optical one, namely SMM J105151.69, SMM J105227.58, SMM J105158.02, SMM J221733.91 and SMM J221806.77. Four out of these five SMGs have mid-IR spectra displaying one particularly prominent feature that we associate with the 7.7 μm PAH line. The presence of additional fainter features confirm the validity of this assumption. The typical uncertainty in the PAH-based redshifts is shown by the error bar in the top panel.

3.3.1 Composite Spectra

In the interest of obtaining a representative spectrum for the sample as a whole, with a higher S/N to enable identification of fainter underlying features, we also median-combined the individual spectra of the SMGs into a composite. The full collection of individual spectra in our sample cover the rest-frame wavelength range $\lambda \sim$ 5–22 μm. To reduce bias towards the mid-IR properties of SMGs within a narrower redshift range, we only include in the composite spectrum wavelengths covered by the data for *at least* five SMGs. The individual spectra in Fig. 3.2 also display a significant spread in rest-frame continuum level with $S_{9\mu\mathrm{m}} \sim 0.2$–$1.2\,\mathrm{mJy}$ and so we normalize them by their flux at a rest-frame wavelength of 8.5 μm. Only the spectrum of SMM J221733.12 does not cover this wavelength and is thus excluded from the composite. The final composite spectrum includes 22 detected SMGs, and is shown in Fig. 3.4. The sample standard deviation of the SMG composite spectrum increases towards longer wavelengths, in part reflecting the fact that fewer individual spectra contribute at $\lambda_{rest} \gtrsim 10$ μm. To better demonstrate the redshift ranges which contribute to the different wavelength regions in the composite (and their variations) we divide our sample into three different redshift bins and construct composite spectra of low-, intermediate- and high-redshift SMGs (see Fig. 3.4). We discuss these in §3.4.6.

We also take advantage of the range in properties covered by our sample (see Fig. 3.1) to investigate mid-IR spectral properties of different SMG sub-populations. We follow the method described above to construct composite spectra of subsamples of SMGs based on 24 μm and radio brightness to search for trends within our sample. However, composite spectra based on apparent brightness mix sources with different intrinsic luminosities at different redshifts: we attempt to minimize this bias in these composites by defining luminosity-complete sub-samples of SMGs. First, we restrict the sample of SMGs that go into each composite to those that fall within a redshift range for which we are close to complete in terms of mid-IR and radio luminosity. At the median redshift of our sample, $< z > \sim 2$, the observed 24 μm flux corresponds

to redshifted rest-frame 8 μm emission. Therefore, we define luminosity-complete sub-samples of SMGs by using the rest-frame luminosities at 8 μm and at 1.4 GHz.[8] We impose a luminosity cut and select all SMGs with luminosities greater than the limiting luminosity (see Fig. 3.5). To build the 24 μm-composites we restrict the parent sample to SMGs with $L_{8\ \mu m} \gtrsim 10^{32}$ erg s^{-1}. For the radio composite, we include SMGs with $L_{1.4GHz} \gtrsim 2 \times 10^{24}$ erg s^{-1} Hz^{-1}. As a result, low-redshift SMGs with the lowest mid-IR and radio luminosities within the sample, even though they have the highest apparent fluxes, are excluded from the 24 μm- and radio-brightness composites. We discuss these composites in §3.4.5.

3.4 Results

Out of the 24 SMGs in our sample shown in Fig. 3.2, we detect PAH emission and continuum in 16 SMGs, PAH emission and no continuum in three SMGs, continuum but no PAH emission in another four SMGs and neither continuum nor PAH emission in only a single SMG (SMM J030231.81). Hence, our sample contains 19 SMGs with PAH emission and 20 with detectable continuum emission. In addition, marginal detections of [ArII] (6.99 μm) and [SiV] (10.51 μm) narrow-line emission were found in several individual SMGs (see Fig. 3.2). We give the emission and absorption line properties for the individual SMGs in Table 3.2. Results for the various composite spectra are presented in Table 3.3.

[8] $L_{1.4GHz} = 4\pi D_L^2 S_{1.4GHz}(1+z)^{-(\alpha+1)}$ W Hz^{-1}, assuming $\alpha = -0.8$, the average spectral index for star-forming galaxies (e.g., Yun et al. 2001)

3.4.1 PAH-based Redshifts

We have rest-frame UV redshifts for all the SMGs in our sample from optical spectroscopy (C05) using the blue-sensitive Low-Resolution Imaging Spectrograph (Oke et al. 1995; McCarthy et al. 1998) on Keck II. These spectroscopic redshifts allowed us to identify confidently faint emission and absorption features in the mid-IR spectra of individual SMGs. Nevertheless, with 19 SMGs displaying prominent PAH emission, we can determine a mid-IR redshift for each SMG based on the location of the redshifted PAH features and compare these to the rest-frame UV redshifts for these galaxies. PAH-based redshifts (z_{PAH}) for our sample are shown in Table 3.2 and are compared to the redshifts from C05 (z_{opt}) in Fig. 3.6. We note that PAH-derived redshifts have a large uncertainty ($\Delta z \sim 0.1$) arising from the intrinsically large width of PAH features ($\mathrm{FWHM}_{7.7\mu\mathrm{m}} \gtrsim 10^4\,\mathrm{km\,s^{-1}}$). Redshifts based on rest-frame UV features are thus more precise, although equally we note that as the optical emission in these systems does not trace the bolometric emission well, there are opportunities for them to be erroneous if the optical spectroscopic IDs are spatially offset from the true radio counterpart. The comparison in Fig. 3.6 demonstrates that the IRS spectra of the majority of the SMGs have features consistent with the rest-frame UV redshifts. However, there are five SMGs where the features suggest an alternate redshift (see Table 3.2) that is significantly different from the rest-frame UV redshift.

For the five SMGs with discrepant redshifts (see Fig. 3.7), the reasons for the disagreement are in all cases due to ambiguous line identifications resulting from low S/N features in the UV spectra, and so we discuss these individually. We note that these corrections to the redshifts have not significantly changed the interpretation of these sources.[9] We also note that one of the new PAH redshifts, for SMM J105158.02, strengthens the significance of the $z \sim 2.7$ SMG cluster/association discovered in Blain et al. (2004).

In the case of SMM J221733.91, an initial indication of a redshift around $z \sim 2.5$ from absorption features in a low S/N spectrum was apparently verified by a weak Hα

[9]Changes in redshift at the 10–20% level at $z \sim 2$ do not result in changes to the luminosities or temperatures beyond the associated calibration errors.

Table 3.2. Characterization of Mid-IR Spectral Features in Individual SMGs

SMM J	z_{opt}[a]	z_{PAH}[b]	$S_{6.2}$[c]	$EW_{6.2}$[d]	$S_{7.7}$	$EW_{7.7}$	$S_{8.6}$	$EW_{8.6}$	$S_{11.3}$	$EW_{11.3}$	$S_{12.7}$	$EW_{12.7}$	$\tau_{9.7}$[e]	$S_{24.0}$[f]
030227.73	1.408	1.43	5.51±0.97	0.18±0.03	20.44±1.50	0.65±0.05	7.92±1.40	0.25±0.04	5.47±1.00	0.17±0.03	6.93±0.84	0.21±0.03	>0.05	0.45
030231.81[g]	1.316	–	–	–	–	–	–	–	–	–	–	–	–	–
105151.69	1.147	1.62	16.07±1.20	0.50±0.04	17.60±2.50	0.79±0.09	–	–	4.40±1.60	0.43±0.15	–	–	>0.34	0.28
105158.02	2.239	2.69	–	–	8.56±7.10	–	0.69±7.50	0.83±0.06	–	–	–	–	–	0.12
105200.22	0.689	0.67	–	–	–	–	–	–	3.55±1.10	0.28±0.09	–	–	>0.49	0.88
105227.58	2.142	2.41	–	–	8.62±1.50	0.57±0.10	1.58±0.92	0.10±0.06	–	–	–	–	–	0.19
105238.19	1.852	1.87	9.13±0.64	0.33±0.02	26.11±1.10	1.39±0.06	6.45±1.20	0.43±0.08	–	–	–	–	>0.27	0.51
105238.30	3.036	2.99	–	–	6.05±0.62	0.04±0.00	–	–	–	–	–	–	–	0.75
123549.44	2.203	2.24	–	–	15.38±1.40	0.21±0.02	2.13±0.84	0.03±0.01	–	–	–	–	–	0.63
123553.26	2.098	2.17	–	–	4.18±1.30	0.09±0.03	5.19±1.70	0.16±0.05	–	–	–	–	–	0.39
123707.21	2.484	2.49	4.91±1.20	0.19±0.05	12.30±1.20	0.45±0.04	2.90±0.71	0.10±0.02	–	–	–	–	–	0.18
123711.98	1.992	1.99	8.75±0.96	0.41±0.04	36.07±1.70	2.47±0.12	6.68±1.30	0.58±0.11	5.55±0.67	0.85±0.10	–	–	>0.26	0.56
123721.87	0.979	0.97	–	–	2.77±1.10	0.72±0.30	4.35±1.00	1.32±0.31	4.29±1.00	1.16±0.28	2.77±1.20	0.93±0.41	>1.01	0.21
163639.01	1.495	1.49	8.32±1.00	0.51±0.06	10.00±1.80	0.64±0.11	4.45±1.30	0.25±0.08	3.75±1.50	0.20±0.08	6.31±1.50	0.33±0.08	>0.66	0.21
163650.43[h]	2.378	–	–	–	34.93±1.80	0.23±0.01	–	–	–	–	–	–	–	0.95
163658.78	1.190	1.20	–	–	20.51±1.70	0.89±0.07	4.72±1.40	0.20±0.06	5.46±1.10	0.23±0.05	4.95±1.10	0.20±0.05	>0.21	0.56
221733.02	0.926	0.87	–	–	–	–	3.05±1.10	0.21±0.08	4.97±1.10	0.70±0.15	–	–	>0.11	0.31
221733.12	0.652	0.65	–	–	–	–	–	–	13.89±1.60	1.53±0.17	4.77±1.30	0.57±0.16	>1.20	0.36
221733.91	2.555	2.89	5.33±1.20	0.16±0.04	9.45±1.20	0.36±0.05	–	–	–	–	–	–	–	0.24
221735.15	3.098	3.21	–	–	11.54±0.99	0.44±0.04	–	–	–	–	–	–	–	0.04
221735.84	3.089	3.18	3.98±0.61	–	6.28±0.61	–	–	–	–	–	–	–	–	0.01
221737.39[h]	2.614	–	–	–	–	–	–	–	–	–	–	–	–	0.14
221804.42	2.517	2.55	2.72±0.84	0.09±0.03	13.97±2.10	1.28±0.19	–	0.14±0.18	–	–	–	–	–	0.10
221806.77	3.623	1.91	–	–	25.98±0.97	0.17±0.01	4.90±0.67	0.04±0.01	7.35±0.67	0.12±0.01	–	–	–	0.60

[a] Optical redshifts from C05

[b] PAH-based Redshifts; see §3.4.1 for details.

[c] PAH fluxes in units of $10^{-15}\,\mathrm{erg\,s^{-1}cm^{-2}}$. Quoted errors correspond to PAH fitting uncertainties. An additional $\sim 20\%$ is attributed to flux calibration and continuum determination.

[d] PAH rest-frame EWs are expressed in units of μm

[e] Optical depth derived from Silicate-absorption feature. See §3.4.4 for details.

[f] Fluxes reported are average fluxes within $\lambda_{obs} = 23.7 \pm 2.35\mu$m in the individual IRS spectra, to reproduce the 24μm-MIPS band wavelength coverage.

[g] This SMG remained undetected.

[h] We do not report PAH measurements for SMGs with featureless spectra within the relevant PAH region or when PAH features are markedly blended, since relative fitting uncertainties become unduly dominant.

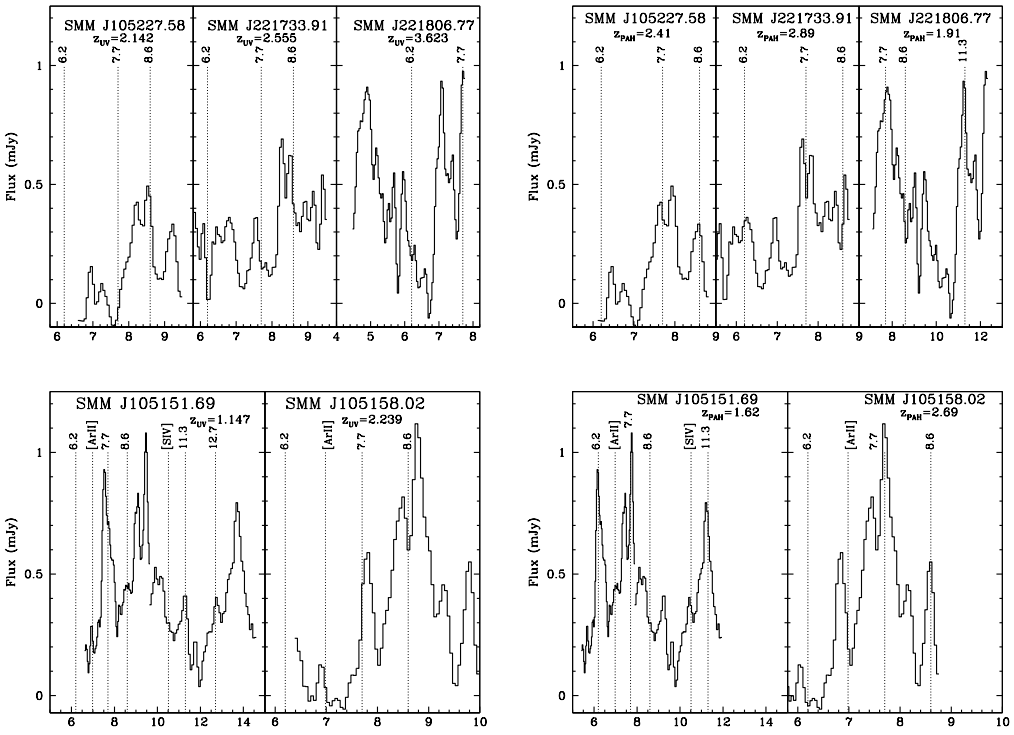

Figure 3.7 Alternate PAH-based redshifts for five individual SMG cases. (**Left:**) Rest-frame mid-IR spectra of SMM J105227.58, SMM J221733.91, SMM J221806.77, SMM J105151.69 and SMM J105158.02 assuming rest-frame UV redshifts (C05). (**Right:**) Rest-frame mid-IR spectra for the same five SMGs with the PAH-based redshifts. For clarity, we have excluded flux uncertainties, which are presented in Fig. 3.2. See §3.4.1 for details.

line at $z = 2.555$ (Swinbank et al. 2004). However, a deeper UV-spectrum, doubling the S/N, revealed an unambiguous $z = 2.865$ from multiple absorption features, consistent with the $z = 2.89$ found from the IRS spectrum.

Similarly with SMM J105227.58, the original noisy UV absorption line spectrum suggested $z = 2.142$. Subsequent deeper spectroscopy revealed this source to be $z = 2.407$ from weak Lyα emission, as well as CIV$_{1549}$ absorption and emission, consistent with the PAH redshift.

SMM J221806.77 was identified at $z = 3.623$ from a single weak emission line in a relatively sky-free spectral region and corroborated by a red continuum dropping out in the B band. The PAH-based redshift $z = 1.91$ suggests that the continuum of this source is more heavily reddened, and that the rest-frame UV emission feature is either noise or a superposed line detection from a different galaxy.

SMM J105158.02 was identified at $z \sim 2.2$ in the UV through various low S/N absorption features. An apparent Hα detection consistent with $z = 2.239$ was proposed as the true redshift (Swinbank et al. 2004), although a failed attempt to detect CO gas cast some doubt on the reality of the redshift (Smail et al., in prep). Re-analysis of a deeper UV spectra reveals a suite of absorption features consistent with $z = 2.694$ (SiII$_{1260}$, CII$_{1335}$).

Finally, for SMM J105151.69, an apparent emission line proposed as [OII]$_{3727}$ corresponding to $z = 1.147$ is not confirmed in later Keck spectra taken on this galaxy at a different position angle, and it has now been identified as an emission line galaxy slightly offset from the radio position. The PAH-based redshift of $z = 1.62$ is consistent with UV-spectra [CIII]$_{1909}$ absorption features and MgII$_{2800}$ emission features.

3.4.2 PAH Luminosities and PAH Ratios

The 7.7 μm PAH feature is the most prominent in the mid-IR spectra of star-forming galaxies and is particularly useful in studying star formation in sources at high redshift. We derive PAH luminosities from the integrated line fluxes presented in Table 3.2 and we plot these in Fig. 3.8. We find 7.7 μm PAH luminosities for SMGs

in the range $\sim 10^{43}$–$10^{45}\,\mathrm{erg\,s^{-1}}$ and hence that, as expected from their far-IR luminosities, SMGs have PAH luminosities that exceed those of local nuclear starbursts (Brandl et al. 2006) and ULIRGs [10] (Armus et al. 2007) by up to nearly four and two orders of magnitude, respectively. These PAH luminosities indicate that $\sim$ 1–5% of the bolometric luminosity in SMGs escapes in the form of PAH emission. We discuss the comparison of SMGs and local sources further in §3.4.6.1.

Different PAH emission features arise from distinct bending/vibrational modes of the PAH molecules (Draine & Li 2007). The different modes can be enhanced relative to each other as a result of varying PAH ionization state and PAH molecule size. Exposure to a more energetic radiation field may strip PAH molecules of peripheral H-atoms. A decrease in the fraction of neutral PAHs would diminish the strength of the 8.6, 11.3 and 12.7 μm PAH features, which are produced by the in-plane (8.6 μm) and out-of-plane (11.3, 12.7 μm) C-H bending mode. As a result, the 6.2 and 7.7 μm PAH features, which are thought to be produced by C-C skeleton vibration (Draine & Li 2007), would dominate. Within this context, the relative strength of PAH features can be used to probe the energetics of the underlying radiation field (e.g., Galliano et al. 2008). The size distribution of PAH molecules may also affect the observed relative strength of features: smaller PAHs ($N_C \lesssim 10^3$) tend to emit more strongly at 6.2 and 7.7 μm (Allamandola et al. 1989). In the hottest regions close to an AGN, sublimation of these smaller PAH molecules may result in a suppression of short-wavelength PAH emission features. Dust extinction has also been shown to play an important role in explaining the variation in the relative strength of PAH features. In particular, strong extinction can increase the 7.7/6.2 and 7.7/8.6 PAH ratios (Rigopoulou et al. 1999) due to an ice absorption feature at $\sim 6\,\mu$m (which reduces the 6.2 μm PAH emission, Spoon et al. 2002) and broad silicate absorption at $\sim 9.7\,\mu$m which reduces the strength of 8.6 μm PAH emission in highly extincted sources.

We derive the ratios of the integrated flux in the 6.2, 7.7 and 11.3 μm PAH features in our sample to investigate the energetics and extinction in the star-forming

[10] We include NGC 6240, Mrk 1014, UGC 5101, Arp 220, FSC 05189−2524, FSC 12112−0305, Mrk 273, FSC 14348−1447, FSC 22491−1808 from Armus et al. (2007).

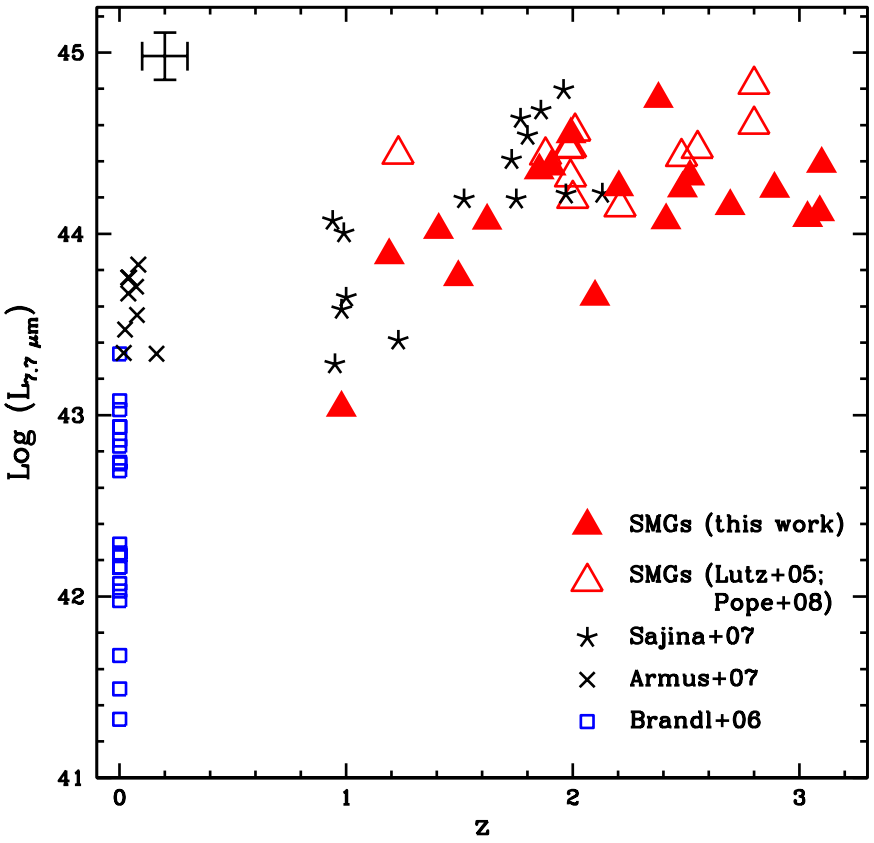

Figure 3.8 The 7.7 μm-PAH luminosities as a function of redshift for the SMGs in our sample. In addition we plot the two SMGs at $z \sim 2.8$ from Lutz et al. (2005) and the SMGs from Pope et al. (2008), many of which come from C05. For comparison we also plot aperture-corrected low-redshift nuclear starburst-dominated galaxies (Brandl et al. 2006), local ULIRGs from the bright *IRAS* sample (Armus et al. 2006, 2007) and high-redshift mid-IR-selected sources (Sajina et al. 2007). We see that SMGs are among the most PAH-luminous objects in the universe, with PAH features nearly four and two orders of magnitude more luminous than local starbursts and local ULIRGs, respectively. This means that the SMG population comprises the most vigorous star-formation events ever observed. See §3.4.2.

environments within SMGs. Fig. 3.9 illustrates that the distribution in values for the 7.7/11.3 PAH ratio in SMGs is very broad and extends over a similar range to that of the high-redshift 24μm-selected sources studied by Sajina et al. (2007). We also compare to the nuclear starburst galaxies from Brandl et al. (2006) and find that SMGs have a median 7.7/11.3 PAH ratio similar to that of low-redshift nuclear starbursts (3.7 ± 1.7 versus 3.7 ± 0.9). Such diversity in PAH ratios is also present in local ULIRGs (e.g., Rigopoulou et al. 1999; Peeters et al. 2004), indicating that diverse radiation field strengths are found amongst both low- and high-redshift sources. However, we note that the need for measurable 11.3 μm emission means that this comparison only includes SMGs at $z < 1.6$ (Fig. 3.4).

Fig. 3.9 also shows that the bulk of SMGs have 7.7/6.2 PAH ratios that are lower than both the high-redshift sources in Sajina et al. (2007) and the median value found for local nuclear starbursts (2.5 ± 1.4 for SMGs versus 5.3 ± 1.7 for the starbursts). This suggests that an intrinsic difference in either radiation field or extinction exists between SMGs and low-redshift nuclear starbursts, which results in a suppressed 6.2 μm PAH feature (Rigopoulou et al. 1999) and a relatively prominent 7.7 μm PAH feature. As we discuss in §3.5.2, we believe that a lesser degree of extinction is responsible for this behavior in SMGs.

3.4.3 Continuum Slopes

The continuum power-law index $\alpha_{\rm MIR}$ characterizes the steepness of the mid-IR continuum, although it requires adequate wavelength coverage to be measured reliably. In Table 3.4 we present the $\alpha_{\rm MIR}$ values for the SMGs whose spectra cover a wavelength range that extends longwards of the silicate absorption and that we thus consider reliable. We find that the SMGs in our sample have a median mid-IR power-law index of $\alpha_{\rm MIR} = 1.3 \pm 1.1$, typical of the continuum found for star-forming regions. The individual spectra span a range of power-law indices $\alpha_{\rm MIR} \sim -0.6$–$2.5$. The majority of our sample, 9/14 SMGs or $\sim 65\%$, have power-law indices which are characteristic of star forming regions ($\alpha_{\rm MIR} \gtrsim 0.5$). The remaining 35% (5/14) have $\alpha_{\rm MIR} \lesssim 0.5$

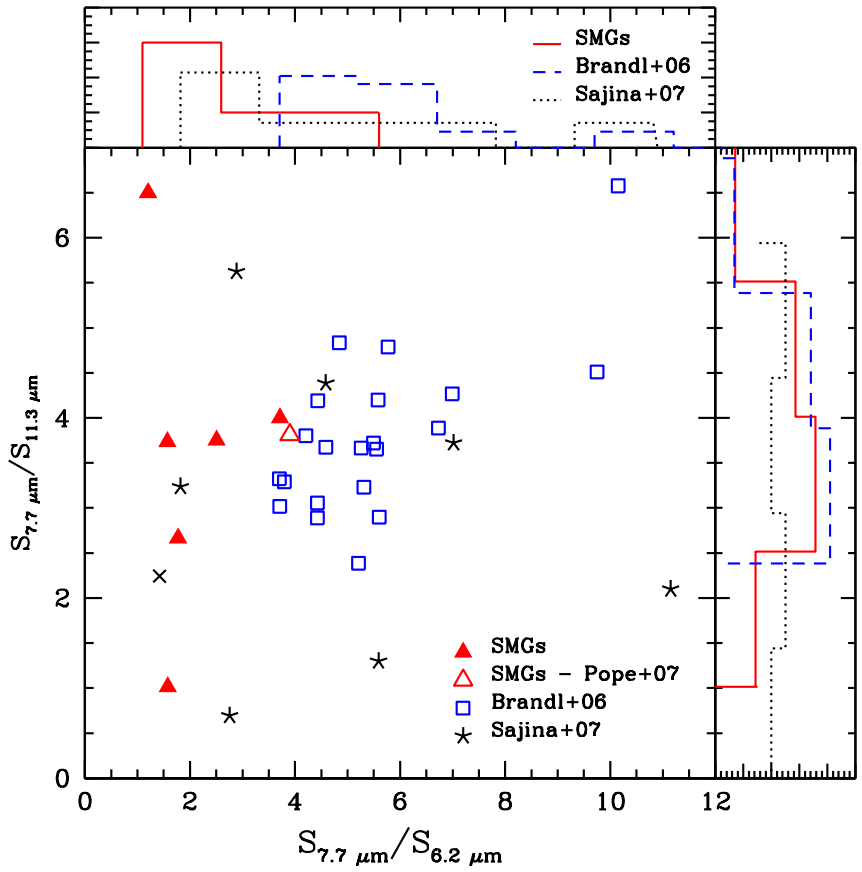

Figure 3.9 PAH ratios for the SMGs in our sample. We also include PAH ratios measured for a sample of low-redshift nuclear starbursts (Brandl et al. 2006), and high-redshift mid-IR selected sources (Sajina et al. 2007). SMGs have similar 7.7/11.3 PAH ratios to these two populations and the distribution of 7.7/6.2 PAH ratios occupies the same range as high-redshift mid-IR selected sources. However, SMGs display 7.7/6.2 PAH ratios that are in general lower than that of low-redshift starbursts.

more characteristic of AGN-dominated regions (e.g., Deo et al. 2007).

For a subset of our sample (those at $z < 1.6$) we can also characterize the continuum shape in the SMGs from their $S_{6\mu m}/S_{12\mu m}$ colors, which is measured at wavelengths devoid of substantial contamination from PAH emission. At 6 μm, the continuum traces thermal emission from hot ($T_{dust} \sim 500$ K) dust, while at 12 μm, the continuum is dominated by dust heated to lower temperatures ($T_{dust} \sim 250$ K). We find that the 4/7 ($\sim 60\%$, Table 3.4) of the SMGs for which we can determine their mid-IR colors show red continua ($S_{6\mu m}/S_{12\mu m} \lesssim 0.3$, $\alpha_{\rm MIR} \gtrsim 0.5$) which resemble the

colors of low-redshift star-forming galaxies and the nuclear starburst galaxies presented by Brandl et al. (2006): $S_{6\mu m}/S_{12\mu m} \sim 0.18$–$0.53$. The remaining 40% of this subsample have bluer continua ($S_{6\mu m}/S_{12\mu m} \gtrsim 0.3$, $\alpha_{\rm MIR} \lesssim 0.5$), more typical of the high-redshift mid-IR selected sources of Sajina et al. (2007) with $S_{6\mu m}/S_{12\mu m} \gtrsim 0.3$.

Taken together, these results suggests that the mid-IR continuum emission in the two-thirds of the SMGs in our sample has the spectral characteristics associated with star forming systems locally. The remaining third of the SMGs show more AGN-like mid-IR continua, although these frequently also display strong PAH emission.

3.4.4 Obscuration as Measured by silicate Absorption

One of the clearest indicators of absorption in the mid-IR arises from intervening amorphous silicate dust grains. Silicate absorption from the stretching of Si-O bonds centered around 9.7 μm is the main absorption feature within the wavelength range considered in this work and is measurable in roughly half of the SMGs in our sample, those at $z < 2.0$.

We use the strength of the silicate-absorption feature as a measure of the obscuration along the line of sight to the warm continuum emission, $\tau_{9.7\mu m}$. We note that this definition of optical depth assumes that the obscuring material lies in a foreground screen, which is likely to be too naive a model for the complex spatial mix of absorption and emission in SMGs.

To calculate $\tau_{9.7\mu m}$ for the individual SMGs, we assume that the bottom of silicate absorption feature is well constrained. However, we stress that since we only detect faint continuum with $S/N \lesssim 3$ for a number of SMGs in our sample, the values we derive for the strength of the silicate absorption are likely lower limits (see Table 3.2). We find a range of optical depths $\tau_{9.7\ \mu m} \sim 0.05$–$1.2$ for the SMGs in our sample, with a median value of $< \tau_{9.7\mu m} >= 0.3 \pm 0.1$.[11] For the composite spectrum, which benefits from an improved S/N, we find an optical depth of $\tau_{9.7\ \mu m} = 0.44 \pm 0.06$.

In Fig. 3.10 we compare the optical depths in SMGs to those of low-redshift nuclear

[11]Including the SMGs with redshifts from C05 from Pope et al. (2008) extends this range to $\tau_{9.7\ \mu m} \sim 1.4$.

starbursts and ULIRGs and to high-redshift mid-IR selected sources. We find that the bulk of SMGs have $\tau_{9.7\ \mu\mathrm{m}}$ values that extend across the range of values covered by high-redshift mid-IR selected sources, but are typically less than those seen in local nuclear starbursts or local ULIRGs. This suggests that the SMGs have lower typical extinction along the lines of sight to their warm continuum emission sources. We stress that the IRS observations of the local ULIRG sample contain 80–90% of the star-formation activity in these systems falling in the slit, and hence these differences in apparent optical depth are not due to comparing galaxy-integrated measurements for the SMGs to measurements of just the nuclear component in local systems (Armus et al. 2007).

We also explore in Fig. 3.10 the distribution in $\tau_{9.7\ \mu\mathrm{m}}$ as a function of the 7.7 μm PAH luminosity relative to the hot-dust continuum at 6 μm, $L_{7.7}/L_6$. The distribution in $(L_{7.7}/L_6)$-values for SMGs and low-redshift star-forming galaxies is quite similar ($L_{7.7}/L_6 \sim 0.1 - 0.8$), and separates from the mid-IR bright high-redshift sources, which display lower values ($L_{7.7}/L_6 \lesssim 0.4$).

3.4.5 Composite Spectra of SMG subsets

3.4.5.1 Investigating 24 μm Selection Biases

We investigate the differences between 24μm-bright and 24μm-faint SMGs (in the observed frame) to understand how representative our sample is of the bulk of the SMG population which have counterparts which are faint at 24 μm. Using the SMGs within the $L_{8\ \mu\mathrm{m}}$-complete sample described in §3.3.1 (see Fig. 3.5), we construct mid-IR composite spectra based on 24 μm-brightness: SMGs with $S_{24\ \mu\mathrm{m}} \gtrsim 0.4\,\mathrm{mJy}$ comprise the 24μm–bright composite, while those with $S_{24\ \mu\mathrm{m}} \lesssim 0.4\,\mathrm{mJy}$ make up the 24μm–faint composite (see Fig. 3.11).

We see stronger 7.7 μm PAH emission, as demonstrated by the line's EW (see Table 3.3), in the 24μm–faint composite, while the 24μm–bright composite displays a greater contribution from hot dust continuum. Thus it appears that the strong PAH emission we see in our SMG sample at $z \sim 2$ is not likely to be a result of our use

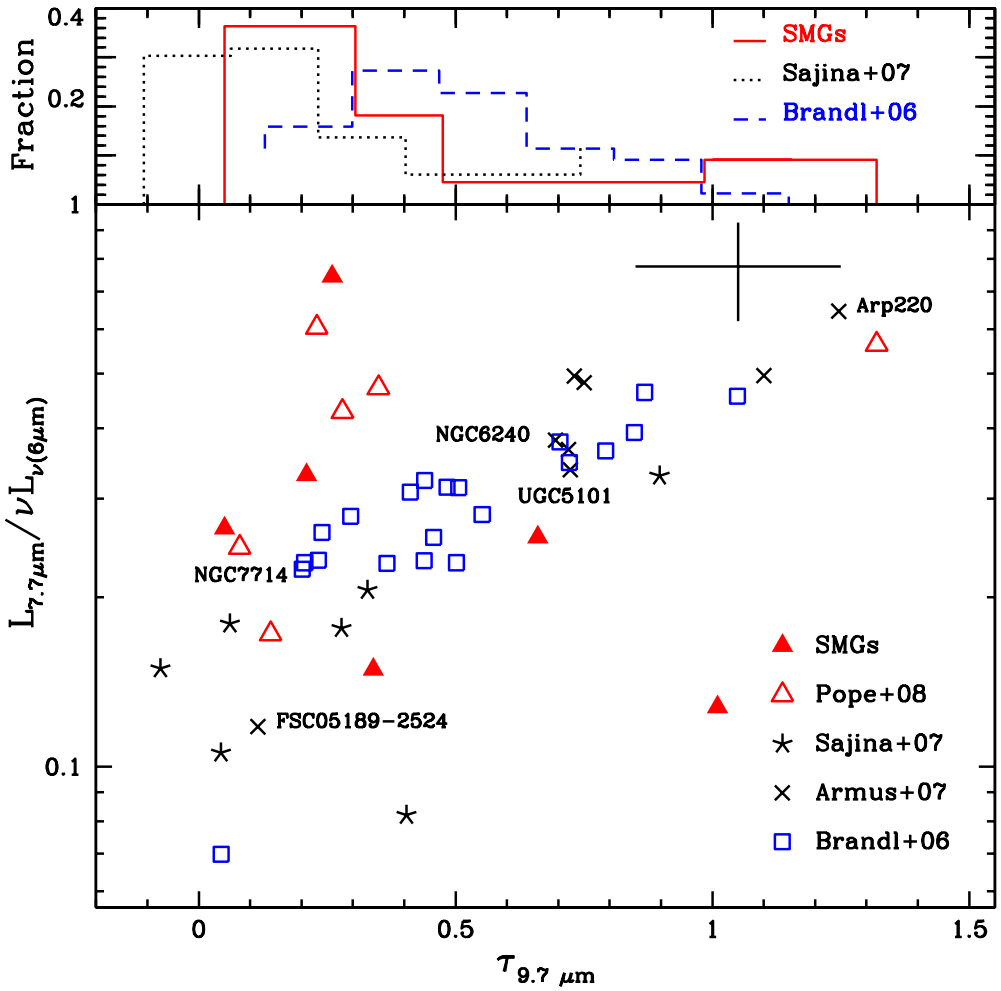

Figure 3.10 A plot of the 7.7 μm PAH luminosity relative to the 6 μm continuum luminosity as a function of silicate optical depth. We include only those SMGs that provide sufficient wavelength coverage for reasonable continuum estimates: 10 SMGs from our sample and seven SMGs from Pope et al. (2008). Optical depths for local nuclear starbursts (Brandl et al. 2006), local ULIRGs (Armus et al. 2007) and high-redshift 24μm-selected sources (Sajina et al. 2007) are also shown for comparison. The error bar displays the representative uncertainties in these measurements. The histogram at the top shows the cumulative distributions for the three samples. We see that the SMGs display much weaker silicate absorption than local nuclear starbursts and ULIRGs, but proportionally stronger 7.7 μm PAH emission. This suggests that the activity in these systems is occurring in less intense environments, even though the SMGs have integrated star-formation rates some four orders of magnitude higher than the local starbursts.

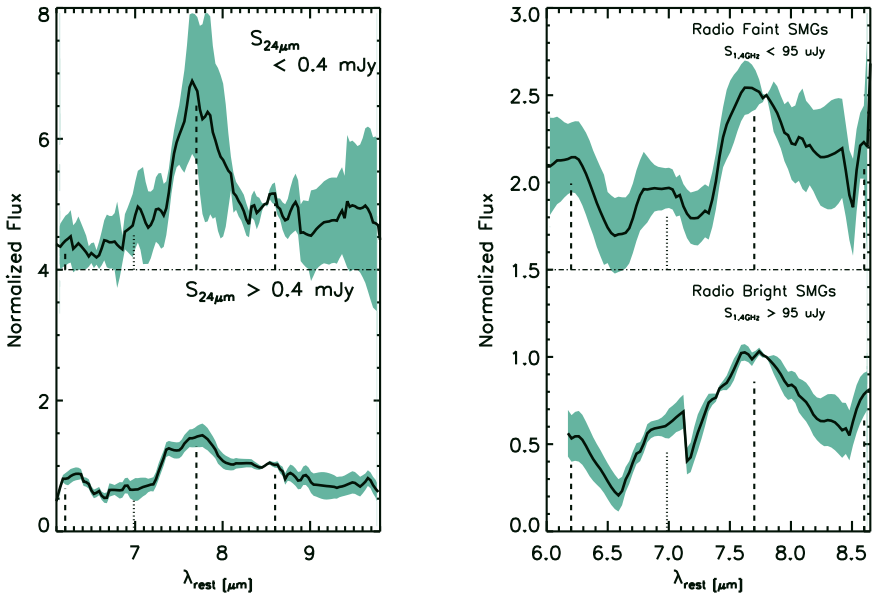

Figure 3.11 (**Left:**) The composite spectra of the seven 24 μm-bright SMGs (bottom) and of the seven 24 μm-faint SMGs (top) within the $L_{8\mu m}$-complete sample. (**Right:**) Composite spectra of the five radio-bright SMGs (top) and of the five radio-faint SMGs (bottom) within the $L_{1.4GHz}$-complete sample. Note that the spectra of the individual SMGs that comprise the radio composites are normalized by their flux at $\lambda = 7.8$ μm. The same flux-scale is maintained for the spectra within each panel and the dash-dotted line denotes the offset zero level for the 24 μm-faint and radio-faint composites. We see that 24μm-faint composite is significantly more PAH-dominated than the 24μm-bright composite, while the latter displays a stronger continuum. In the case of the radio-composites, the radio-bright sample displays a broader 7.7 μm PAH feature over a slightly more prominent continuum. The characterization of the radio-composite spectra do not reveal any significant difference within our measurement uncertainties (see Table 3.3).

Table 3.3. Composite Spectra

Composite	# SMGs	z_{median} [a]	$L_{6.2}$ [b]	$EW_{6.2}$ [c]	$L_{7.7}$	$EW_{7.7}$	$L_{11.3}$	$EW_{11.3}$	$S_{6\mu m}/S_{12\mu m}$	$\alpha_{\rm MIR}$	$\tau_{9.7\mu m}$
all	22	2.00	0.50 ± 0.01	0.05 ± 0.01	3.57 ± 0.05	0.42 ± 0.02	1.16 ± 0.04	0.19 ± 0.02	0.34 ± 0.07	1.17 ± 0.11	0.44 ± 0.06
24um-Bright[d]	7	2.10	–	–	3.51 ± 0.05	0.32 ± 0.01	–	–	–	–	–
24um-Faint[e]	7	2.61	–	–	10.67 ± 0.06	0.69 ± 0.01	–	–	–	–	–
Radio-Bright[f]	5	3.04	–	–	3.67 ± 0.22	0.17 ± 0.04	–	–	–	–	–
Radio-Faint[g]	5	2.38	–	–	1.92 ± 0.11	0.17 ± 0.03	–	–	–	–	–
Starburst-dominated (Xray/UV/opt)[h]	16	1.98	0.59 ± 0.02	0.06 ± 0.01	5.46 ± 0.11	0.70 ± 0.04	1.87 ± 0.15	0.44 ± 0.10	0.41 ± 0.11	0.46 ± 0.07	0.21 ± 0.05
Starburst-dominated (mid-IR)[i]	12	1.97	1.02 ± 0.02	0.09 ± 0.02	5.04 ± 0.11	0.63 ± 0.04	2.09 ± 0.12	0.49 ± 0.08	0.36 ± 0.15	0.40 ± 0.06	0.48 ± 0.10
AGN (Xray/UV/opt)[j]	8	2.00	2.36 ± 0.08	–	3.23 ± 0.15	0.42 ± 0.06	1.66 ± 0.09	0.37 ± 0.02	0.46 ± 0.18	0.59 ± 0.08	0.26 ± 0.04
AGN (mid-IR)[k]	10	2.02	0.75 ± 0.03	–	4.62 ± 0.13	0.52 ± 0.04	1.53 ± 0.10	0.31 ± 0.06	0.44 ± 0.26	0.50 ± 0.06	0.02 ± 0.01

[a] Median redshift of SMGs comprising composite spectrum.

[b] PAH luminosities are expressed in units of $10^{44}\,{\rm erg\,s^{-1}}$. Uncertainties are derived from the propagation of integrated line flux uncertainties as determined by our PAH fitting approach. An additional $\sim 20\%$ is attributed to flux calibration and continuum determination.

[c] PAH rest-frame EWs are expressed in units of [μm].

[d] $S_{24\mu m} > 0.40\,{\rm mJy}$ from the 8μm luminosity-complete sub-sample of SMGs with $L_{8\mu m} > 10^{32}\,{\rm erg\,s^{-1}}$

[e] $S_{24\mu m} < 0.40\,{\rm mJy}$ from the 8μm luminosity-complete sub-sample of SMGs with $L_{8\mu m} > 10^{32}\,{\rm erg\,s^{-1}}$

[f] $S_{1.4GHz} > 95\mu$Jy from the luminosity-complete sub-sample of SMGs with $L_{1.4GHz} > 2 \times 10^{24}\,{\rm erg\,s^{-1}\,Hz^{-1}}$

[g] $S_{1.4GHz} < 95\mu$Jy from the luminosity-complete sub-sample of SMGs with $L_{1.4GHz} > 2 \times 10^{24}\,{\rm erg\,s^{-1}\,Hz^{-1}}$

[h] Composite of SMGs classified as starburst-dominated in the rest-frame optical (Swinbank et al. 2004; Takata et al. 2006), UV (C05) and/or X-ray (Alexander et al. 2005a)

[i] Composite of SMGs classified as starburst-dominated in the mid-IR, with $EW_{7.7\mu m} > 1$ and $\alpha_{\rm MIR} > 0.5$. See text for details.

[j] Composite of SMGs with AGN signatures in the X-ray (Alexander et al. 2005a) and/or in the near-IR (Swinbank et al. 2004; Takata et al. 2006)

[k] Composite of SMGs with AGN signatures in the mid-IR: $EW_{7.7\mu m} < 1$ and $\alpha_{\rm MIR} < 0.5$. See text for details.

of estimated 24 μm-fluxes in selecting our sample, although the prevalence of sources with strong continuum emission (and hence the contribution from AGN or highly obscured starbursts) is likely to be higher in our sample than in the general SMG population.

3.4.5.2 Exploring the Radio Bias

We use the range in radio fluxes covered by our sample (see Fig. 3.1) to investigate possible intrinsic trends in mid-IR properties associated with radio brightness. We seek to address potential differences between our sample of radio-identified SMGs and the $\lesssim 30\%$ of $S_{850\mu\mathrm{m}} \gtrsim 5\,\mathrm{mJy}$ SMGs with radio counterparts below the sensitivity of current radio surveys. The lack of a radio counterpart for an SMG may result from their lying at significantly higher redshifts than the radio-identified population ($z \gg 3$, C05; Younger et al. 2007). We cannot test this suggestion with our sample as we have targeted SMGs with known redshifts. However, it has also been suggested that the radio-undetected SMGs lie at similar redshifts to the dominant radio-detected population, but that they have somewhat lower IR luminosities and slightly colder characteristic dust temperatures, a combination which would result in similar observed 850 μm fluxes (Blain et al. 1999; Chapman et al. 2004). Our radio-detected sample may therefore be biased towards systems with hotter characteristic dust temperatures, either due to typically more compact star forming regions or the presence of an AGN. To investigate this possibility, we divide our sample into radio-bright and radio-faint SMGs. We first define a luminosity-complete sub-sample of SMGs based on their rest-frame radio luminosity and use their apparent radio fluxes to build the composite spectra (see Fig. 3.11).

The radio-faint SMG composite has a narrow 7.7 μm PAH feature that emerges sharply from the continuum, while the radio-bright composite displays a broader, less distinct PAH feature. Considering the line-to-continuum parameter (l/c; e.g., Genzel et al. 1998), traditionally used to gauge the strength of PAH features, the radio-faint composite displays a higher 7.7 μm–(l/c) relative to the radio-bright composite. This difference may suggest that the radio-bright composite has a larger obscured AGN

contribution, which we perceive in the mid-IR as a broadening of the 7.7 μm PAH feature, which could ultimately become a continuum-dominated feature at $\lambda \sim 8$ μm, similar to the spectrum of SMM J163650.43. However, the EWs of the 7.7 μm PAH feature in these composites are not significantly different within the measurement uncertainties (see Table 3.3). Therefore, overall our observations do not reveal any significant difference in mid-IR properties based on radio-luminosity and we conclude that our radio-detected SMG sample is likely to be representative of the whole SMG population at $z \lesssim 3.5$.

3.4.5.3 Starburst and AGN-Dominated Composites

The SMGs in our sample have been classified prior to this work as either AGN- or star-formation–dominated systems using deep X-ray observations (Alexander et al. 2005a), rest-frame optical spectroscopy (Swinbank et al. 2004; Takata et al. 2006) and/or rest-frame UV spectroscopy (C05). Table 3.4 provides a summary of these classifications. We construct composites for an AGN and star-forming class based on these classifications to investigate differences in mid-IR spectral properties (see Fig. 3.12). Since we do not take mid-IR properties into account to build these composites, the differences are not the result of any mid-IR selection bias.

Both composite spectra display prominent PAH features, but the PAH emission in the AGN composite spectrum lies on top of a stronger continuum, in comparison to the star-forming composite: the 7.7 μm PAH feature EW of 0.42 ± 0.06 and 0.70 ± 0.04 respectively reflect this difference. The other possible difference between these composites is that the AGN composite spectrum has an emission feature at $\lambda = 10.51$ μm, which is much less obvious in the star-forming composite. This feature may correspond to [SIV] narrow-line emission, which is commonly associated with a hot starburst or AGN activity (Spoon et al. 2002; Ogle et al. 2006). We note that all of the individual SMGs in this AGN-composite whose spectra cover the $\lambda \sim 10.5$ μm wavelength region show what could correspond to [SIV] emission (see Fig. 3.2). Since the SMGs that make up this composite have AGN signatures in the rest-frame UV and optical, it is likely that our line of sight has direct access into the broad line

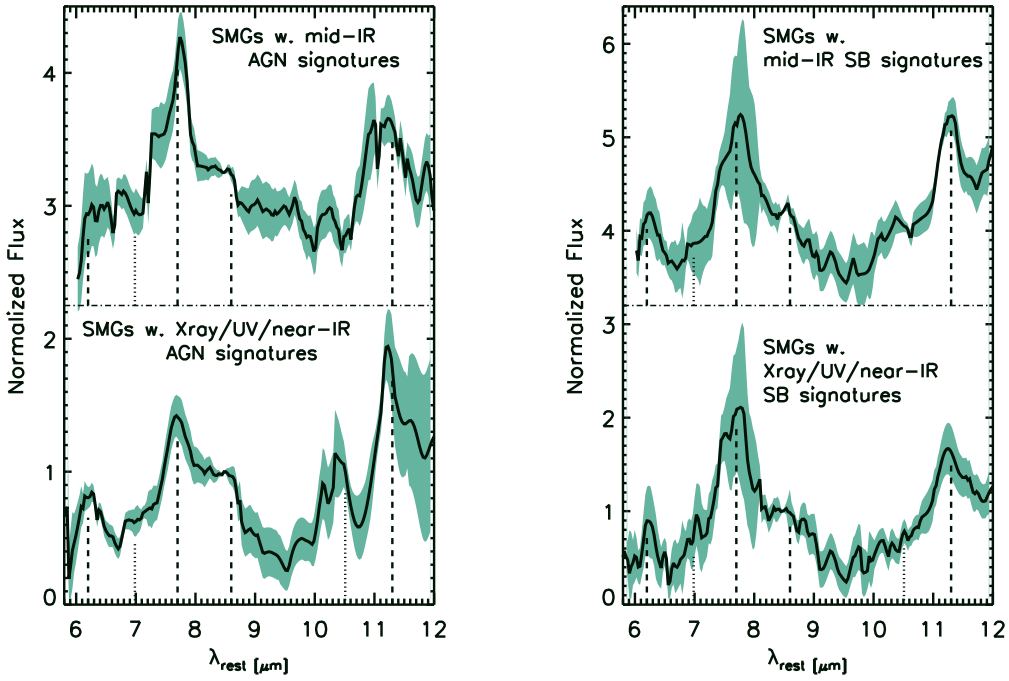

Figure 3.12 (**Left:**) Composite mid-IR spectra of the eight SMGs in the sample with AGN signatures in the X-ray (Alexander et al. 2005a), optical (C05) or near-IR (Swinbank et al. 2004) (bottom) and of the 10 SMGs with mid-IR spectra that suggest the presence of an AGN (top). (**Right:**) Composite spectra of the 16 SMGs in our sample with *no* AGN signature either in the X-ray, optical or near-IR (bottom) and of the 12 SMGs with mid-IR spectra dominated by strong star-formation activity. We see that the AGN-composites display an enhanced continuum relative to the star-forming counterparts. We also note that the AGN-composite with AGN signatures at wavelengths other than the mid-IR (bottom left panel) displays a prominent emission feature, likely corresponding to [SIV] emission from an AGN. See §3.4.5.3 for details.

region. Thus it is also possible that this feature corresponds instead to solid silicate emission from very near a central AGN.

In Fig. 3.12 we show the composite spectra for AGN- and starburst- subsets, based this time on their mid-IR classifications. We classify SMGs with $\mathrm{EW}_{7.7\ \mu\mathrm{m}} \gtrsim 1$ or steep mid-IR continua ($S_{6\ \mu\mathrm{m}}/S_{12\ \mu\mathrm{m}} \lesssim 0.3$) as star-formation–dominated systems; SMGs with $\mathrm{EW}_{7.7\ \mu\mathrm{m}} \lesssim 1$ or flat mid-IR continua ($S_{6\ \mu\mathrm{m}/12\ \mu\mathrm{m}} \gtrsim 0.8$ or $\alpha_{\mathrm{MIR}} \lesssim 0.5$) are classified as having a significant AGN contribution (see Table 3.4). Both of these composites display an enhanced underlying continuum, relative to their respective composite counterparts based on AGN signatures at other wavelengths. This is most likely due to the need to have moderate mid-IR emission for an object to be classifiable in the mid-IR. However, there is one notable difference between the two mid-IR classified spectra: Fig. 3.12 shows that the 6.2 μm PAH feature appears to have been diluted by the enhanced continuum in the AGN composite.

3.4.6 The SMG Spectrum

With more than $\sim 80\%$ of the individual SMGs in our sample displaying PAH features, unsurprisingly the composite spectrum in Fig. 3.4 displays prominent PAH emission. Using our large sample of SMGs covering a wide redshift range, we explore composite spectra of SMGs in three redshift bins: low ($z \leq 1.6$), intermediate ($z = 1.6$–2.4) and a high ($z \geq 2.4$); see Fig. 3.4. The SMGs in the low-redshift bin dominate the composite spectrum at $\lambda \gtrsim 10$ μm. All three redshift composites display strong 7.7 μm PAH emission and a prominent 8.6 μm feature. With increasing redshift we observe a broadening of the 7.7 μm PAH feature and a weakening of the 6.2 μm PAH feature. The increase in scatter around the median composite spectrum indicates either a more diverse range in spectral properties at the higher redshifts, or poorer S/N. However, we note that the three composites display an increase in continuum level with redshift. Within the context discussed in §3.4.2, the weakening of the observed 6.2 μm PAH emission feature may be an indication that SMGs at higher redshifts suffer from either increased extinction, hampering detection of PAH emission

features at the shorter wavelengths, or from a systematic hardening of the radiation field that the PAH molecules encounter.

3.4.6.1 Comparison to Local Templates

In Chapter 2 (Menéndez-Delmestre et al. 2007) we found that the composite spectrum is well fit by a starburst-like template (represented by M82) with an additional continuum component, likely arising from an AGN (see Fig. 2.1). We found that the mid-IR spectral features of SMGs are more comparable to those of the M82 starburst, than to other well-studied local ULIRGs, such as Arp 220 and Mrk 1014. We now consider our complete sample of 24 SMGs.

The mid-IR composite spectrum of the SMGs in our sample is reasonably well fit at $\lambda \lesssim 10$ μm by the composite spectrum of nearby nuclear starburst-dominated galaxies (Brandl et al. 2006; see Fig. 3.13). By using this more diverse starburst template, we seek to better represent the diversity in continuum slopes and PAH strengths in starburst-dominated galaxies in the local Universe.

The PAH component of the SMG composite spectrum is well represented by a starburst template, but we find that an additional power-law continuum remains necessary to describe the overall composite spectrum: at the longer wavelengths, $\lambda \gtrsim 10$ μm, the starburst template fails to match the continuum level (see Fig. 3.13). This continuum component may be associated with AGN activity or an additional starburst continuum component. To quantify this we characterize the red continuum in the composite SMG that is unaccounted for by the starburst template by fitting a power-law to the (SMG composite − starburst-template) residuals. We find that the residuals are best fit by a power-law $F_\nu \sim \nu^{-\alpha_{\rm MIR}}$, where $\alpha_{\rm MIR} = 1.97 \pm 0.22$. In the next section we estimate an upper limit to the contribution from an AGN, making the conservative assumption that all of the additional continuum component arises from a dust-enshrouded AGN.

Table 3.4. AGN and Starburst Signatures in Radio-Identified SMGs

SMM J	$\alpha_{\rm MIR}$[a]	$S_{6.0}/S_{12.0}$	X-ray[b]	UV[c]	Hα	mid-IR	Comment
030227.73	2.08 ± 0.11	0.24 ± 0.12	–	SB	AGN[d,e]	int	$\alpha_{\rm MIR} > 0.5$, EW$_{7.7\mu m} < 1$
030231.81	–	–	–	SB	–	–	undetected
105151.69	0.07 ± 0.22	0.96 ± 0.48	–	SB	–	int	$\alpha_{\rm MIR} < 0.5$, EW$_{7.7\mu m} < 1$
105158.02	–	–	–	SB	SB[d]	SB?	strong PAH emission above faint continuum
105200.22	1.76 ± 0.11	0.30 ± 0.14	–	SB	–	SB	$\alpha_{\rm MIR} > 0.5$
105227.58	–	–	–	SB	–	int	EW$_{7.7\mu m} < 1$
105238.19	–	–	–	SB	–	SB	EW$_{7.7\mu m} > 1$
105238.30	–	–	–	AGN	–	AGN	EW$_{7.7\mu m} < 1$, continuum-dominated
123549.44	–	–	AGN	SB	int[d]/AGN[e]	int	EW$_{7.7\mu m} < 1$
123553.26	−0.75 ± 0.50	–	SB	SB	–	AGN	$\alpha_{\rm MIR} < 0.5$, EW$_{7.7\mu m} < 1$, continuum-dominated
123707.21	2.46 ± 1.3	–	AGN	SB	SB[e]	int	EW$_{7.7\mu m} < 1$
123711.98	−0.10 ± 0.30	<1.07	AGN	SB	–	int	$\alpha_{\rm MIR} < 0.5$, EW$_{7.7\mu m} > 1$, faint continuum
123721.87	0.22 ± 0.33	<0.86	AGN	AGN	SB[e]	int	EW$_{7.7\mu m} < 1, \alpha_{\rm MIR} < 0.5$
163639.01	2.20 ± 0.32	<0.22	–	SB	SB[d]/int[e]	int	EW$_{7.7\mu m} < 1, \alpha_{\rm MIR} > 0.5$
163650.43	–	–	–	int	AGN[d,e]	AGN	Absorbed continuum
163658.78	2.07 ± 0.32	0.24 ± 0.06	–	SB	–	SB	$\alpha_{\rm MIR} > 0.5$, EW$_{7.7\mu m} \sim 1$
221733.02	−0.62 ± 0.45	–	–	SB	SB[e]	int	$\alpha_{\rm MIR} < 0.5$, prominent 7.7μm PAH feature
221733.12	1.26 ± 0.25	–	–	SB	–	SB	$\alpha_{\rm MIR} > 0.5$, prominent 11.3, 12.7μm PAH features
221733.91	0.84 ± 0.72	–	–	SB	SB[d]	int	$\alpha_{\rm MIR} > 0.5$, EW$_{7.7\mu m} < 1$
221735.15	–	–	–	SB	–	–	EW$_{7.7\mu m} < 1$, faint continuum
221735.84	–	–	–	SB	–	–	7.7μm PAH feature above faint continuum
221737.39	–	–	–	SB	AGN[e]	AGN	featureless, continuum-dominated
221804.42	–	–	–	SB	–	SB?	EW$_{7.7\mu m} > 1$, faint continuum
221806.77	−0.39 ± 0.35	–	–	SB	–	int	EW$_{7.7\mu m} < 1$, $\alpha_{\rm MIR} < 0.5$

[a] We report mid-IR colors for SMGs with wavelength coverage $\lambda_{rest} \sim 6$–12μm.

[b] From Alexander et al. (2005a)

[c] From C05

[d] From Swinbank et al. (2004)

[e] From Takata et al. (2006)

3.4.7 The AGN Contribution to the Bolometric Luminosity in SMGs

Hard X-ray emission provides one of the most direct routes to estimate the luminosities of AGN. However, in the presence of high column densities, such as are found for SMGs ($N_H \sim 10^{23}$–$10^{24}\,cm^{-2}$; Alexander et al. 2005a,b), hard X-ray photons may be completely absorbed. In these difficult cases an alternate probe for AGN emission is to trace the mid-IR emission from hot dust near the AGN. The mid-IR thus provides a complementary insight into a deeply obscured AGN (Sturm et al. 2006; Lutz et al. 2004). In particular, Krabbe et al. (2001) show that the 10.5 μm-flux is tightly correlated with the moderately hard X-ray emission, $S_{2-10keV}$, both in Seyfert and in starburst galaxies, which have markedly distinct mid-IR slopes. We use the derived correlation for Seyfert galaxies to estimate the X-ray luminosity of the AGN component in the SMG composite spectrum and thus estimate the AGN contribution to the bolometric luminosity of SMGs.

The composite spectrum includes a power-law continuum, $S_\nu \sim \nu^{-\alpha_{MIR}}$, with spectral slope $\alpha_{MIR} = 1.97 \pm 0.22$ (see Fig. 3.13). From the 10.5 μm continuum flux we infer an X-ray luminosity, $L_X \sim 8 \times 10^{43}\,erg\,s^{-1}$, for the SMGs in our sample at $< z > \sim 2.0$. Encouragingly, this estimate is in close agreement with the absorption corrected rest-frame 0.5–8 keV X-ray luminosities found for the SMGs in the *Chandra* Deep Field (Alexander et al. 2005a), $< L_X >= 5 \times 10^{43}$ erg s^{-1}. To assess the contribution of the AGN to the energetics of the SMGs we first estimate the far-IR luminosities of the SMGs using the observed radio–far-IR correlation for SMGs (Kovács et al. 2006), yielding an average far-IR luminosity of $L_{IR} \sim 5 \times 10^{45}\,erg\,s^{-1}$. We then use the approach of Alexander et al. (2005a) and Menéndez-Delmestre et al. (2007), adopting the X-ray-to-FIR luminosity ratio typically found for quasars ($L_X/L_{IR} \simeq 0.05$; Alexander et al. 2005a) to estimate that the AGN in SMGs contribute $L_{IR} \simeq 1.6 \times 10^{45}$ erg s^{-1}, or $\lesssim 35\%$ of the SMG's far-IR luminosities. As discussed earlier, due to the biases towards including mid-IR bright SMGs in our sample, it is likely that the AGN contribution estimated here is biased high. It is also

very likely that some fraction of this red continuum arises from dust emission heated by very deeply enshrouded starbursts in these SMGs and so we claim this as a firm upper limit to the AGN contribution in typical SMGs.

With an SMG composite dominated by PAH features, it is clear that the bolometric luminosity of SMGs is in general dominated by star formation. However, the individual mid-IR SMG spectra display modest variation in AGN contribution and in some cases reveal the presence of an AGN that remains invisible at other wavelengths (see Table 3.4). In particular, there is evidence that SMM J123553.26 is a Compton-thick AGN: it is undetected in the X-ray but is bright and dominated by continuum emission in the mid-IR and displays no mid-IR signatures of star formation (see Fig. 3.2). Extrapolating from its mid-IR spectrum, we estimate a hot dust luminosity [12], $L_{6\mu\mathrm{m}} \sim 2.0 \times 10^{45}$ erg s^{-1}. Following the procedure described by Alexander et al. (2008b) we use the 0.5–2 keV observed luminosity for SMM J123553.26 (Alexander et al. 2005a) to derive a rest-frame 1.6–24.8 keV luminosity, which we convert to an intrinsic X-ray luminosity, $L_{2-10\mathrm{keV}} < 2 \times 10^{42}$ erg s^{-1}, assuming an X-ray spectral index, $\Gamma = 1.4$. On the basis of the X-ray-to-6μm luminosity ratio of this SMG, we find that it lies significantly below the X-ray-to-6μm luminosity relationship found for nearby AGN, suggesting that this source hosts a luminous Compton-thick AGN (e.g., Alexander et al. 2008b). However, we note that this SMG lies very close to a number of mid-IR bright sources, which complicates the deblending of the individual flux contributions in MIPS 24 μm imaging (Hainline et al. 2009). We detect only a single source in the IRS 2D spectrum. While this coincides with the position expected for SMM J123553.26, it remains possible that the measured mid-IR flux of this source does not correspond to the X-ray source.

3.4.8 Comparison to SMGs in Other Samples

With a sample of 23 detected SMGs in this work, plus nine from Valiante et al. (2007) and 13 from Pope et al. (2008), we have statistics to allow an adequate eval-

[12] $\nu\,\mathrm{L}_\nu = 4\pi D_L^2 S_{6\mu\mathrm{m}} \times \nu_{6\mu\mathrm{m}}/(1+z)$

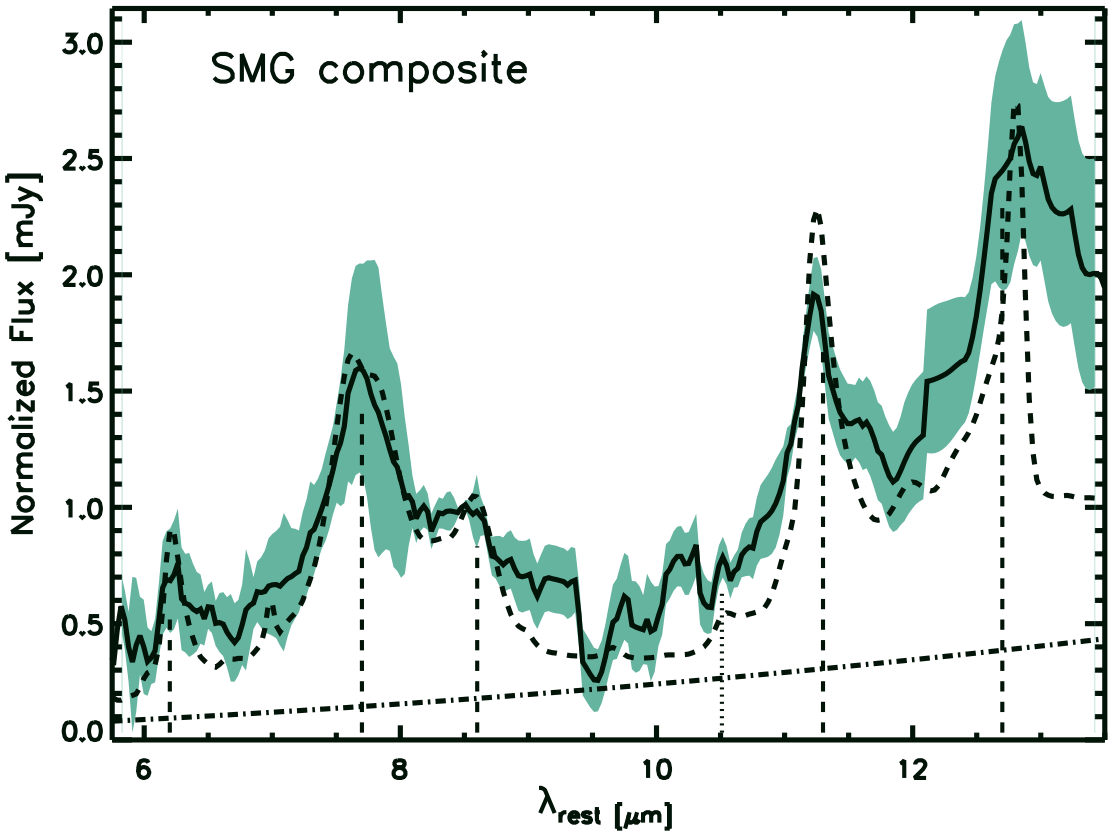

Figure 3.13 The composite spectrum of 22 SMGs detected in our sample as shown in Fig. 3.4. The dashed curve is the mid-IR composite spectrum of 13 starburst-dominated low-redshift galaxies from Brandl et al. (2006), scaled down to match the SMG composite spectrum at 7.7 μm. The dash-dotted line is the power-law component ($\nu S_\nu \sim \nu^{-\alpha}$, $\alpha_{\rm MIR} \sim 1.97$) that best represents the continuum in the composite SMG that is unaccounted for by the starburst template. See § 3.4.7 for details.

uation of the mid-IR properties of the SMG population as a whole. The majority of SMGs display dominant PAH features atop an underlying power-law continuum, that potentially arises from an AGN.

Together with results published in parallel mid-IR studies (Lutz et al. 2005; Menéndez-Delmestre et al. 2007; Valiante et al. 2007; Pope et al. 2008), we are uncovering the range in mid-IR properties present within this galaxy population: mid-IR spectra that correspond to dominant starbursts, with varying AGN contributions to their bolometric luminosity. We find only one clear example of a continuum-dominated source with a prominent broad feature centered at $\lambda \sim 8$ μm, SMM J163650.43 (Menéndez-Delmestre et al. 2007). Three other SMGs in our sample display featureless continuum-dominated spectra (SMM J105238.30, SMM J123553.26, and SMM J221737.39). In the sample of nine detected SMGs presented by Valiante et al. (2007) and Lutz et al. (2005), SMM J02399-0136 displays PAH features overlaying a particularly strong continuum, and is thus classified as a source powered by equal contributions of star formation and a Compton-thick AGN (Valiante et al. 2007). Out of the 13 SMGs in the GOODS-North field, SMM J123600.15 (C1; Pope et al. 2008) also displays PAH features on a steeply rising continuum and is classified as an SMG with a 44% AGN contribution to the bolometric luminosity.

We note that 25% of the SMGs in our sample lie at redshifts $z \lesssim 1.2$, which is a redshift range not covered by the other SMG mid-IR studies. This extension to lower redshifts provides us with an extended insight into the longer mid-IR wavelengths, $\lambda \gtrsim 11.5$ μm, for a crucial comparison between SMGs and potential local analogs. This longer wavelength coverage is also very useful for constraining better the mid-IR continuum in these sources, and so for measuring features such as the 9.7 μm silicate absorption.

To determine explicitly the effect of including these longer wavelengths, we recalculated our results considering only the composite spectrum shortwards of $\lambda = 11.5$ μm. In this case, we find that the composite spectrum of the SMGs in our sample is well fit by the starburst template from Brandl et al. (2006) with an additional shallower continuum ($\alpha_{\rm MIR} \sim 0.94 \pm 0.31$), which translates into a $\lesssim 30\%$ AGN contribution. This

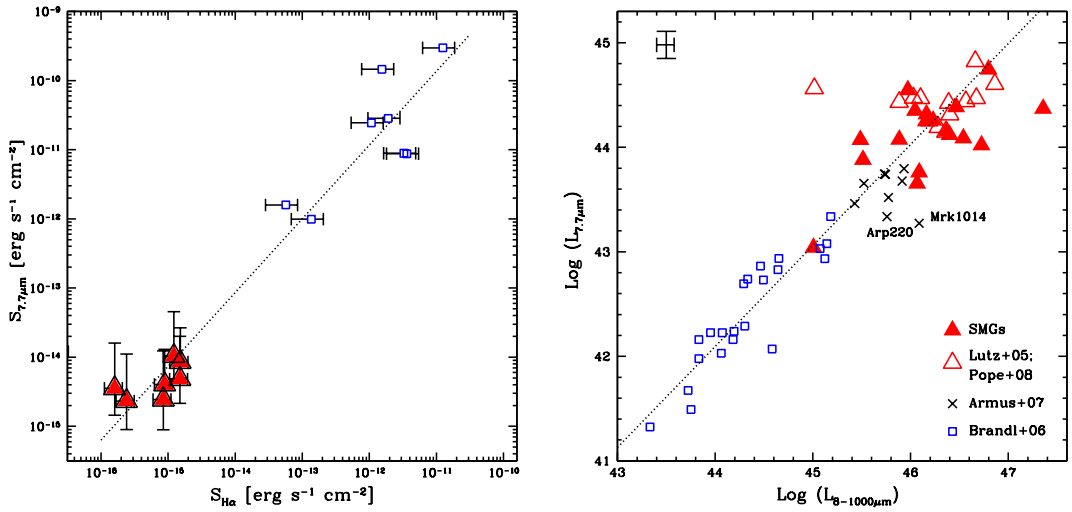

Figure 3.14 (**Left:**) The integrated flux of the 7.7 μm PAH feature as a function of narrow-line Hα flux for SMGs in our sample and for local galaxies. The Hα fluxes are corrected for extinction, typically by a factor of 2–3. Hα fluxes for the low redshift star-forming galaxies are taken from Armus et al. (1989), Heckman et al. (1990), Veilleux et al. (1999), Buat et al. (2002) and Lira et al. (2002). An uncertainty of $\sim 10\%$ is associated with the fluxes of the 7.7 μm PAH features for the low-redshift systems and this uncertainty is smaller than the points in the graph. The dotted line represents a simple best linear fit for both the low- and high-redshift samples, demonstrating the clear correlation between these parameters. We see that PAH integrated fluxes correlate well with narrow-line Hα and that SMGs extend the local relation out to the PAH- and Hα-bright region. (**Right:**) PAH luminosities as a function of IR luminosity for the SMGs in our sample and for those in Pope et al. (2008) and Lutz et al. (2005). We use total IR luminosities from C05, corrected by approximately a factor of two, following Kovács et al. (2006). We also include aperture-corrected PAH luminosities of low-redshift nuclear starbursts (Brandl et al. 2006) and local ULIRGs (Armus et al. 2007). The dotted line shows a simple best linear fit to local nuclear starbursts. The error bar represents the typical uncertainties in the observations.

power-law index is significantly lower than that corresponding to the best power-law fit determined for the full composite spectrum in Fig. 3.13, $\alpha_{\rm MIR} = 1.97 \pm 0.22$. The AGN contribution derived for the short-wavelength SMG composite is in agreement with the results of Pope et al. (2008), where the redshift range of the SMGs studied is restricted to $z \gtrsim 1.2$.

3.5 Discussion

We compare the mid-IR properties of the SMGs in our sample with those of starburst-dominated low-redshift galaxies (Brandl et al. 2006), select local ULIRGs from the Bright IRAS sample (Armus et al. 2006, 2007) and the mid-IR selected sources of Sajina et al. (2007). We use PAH luminosities, PAH relative intensities, the steepness of the continuum and the strength of silicate absorption to compare the level of star-forming activity, the energetics in radiation environments and the distribution of cold and warm dust in these galaxies.

SMGs have among the most luminous PAH emission of any population in the universe, displaying levels of activity which are unseen in local samples (Fig. 3.8). This result reflects the significant increase in star-formation activity in the high-redshift SMG population which underpins the thousand-fold increase in the space density of ULIRGs out to $z \sim 2$ (C05). A similar increase in PAH luminosity has been seen by Desai et al. (2007), who investigated the strength of the 6.2 μm PAH feature in ULIRGs at low and intermediate redshifts ($z \lesssim 1$) and found that ultra-luminous sources at high redshift have PAH EWs larger than any present in the local Universe.

We find that PAH luminosities display no dependence on continuum slope or continuum mid-IR color. Hot dust located close to an AGN would contribute to an enhanced continuum emission at the shorter mid-IR wavelengths ($\lambda \lesssim 10$ μm), and so we associate mid-IR spectra displaying flatter continua with the likely presence of an unobscured AGN. The presence of large PAH luminosities in SMGs with a flat mid-IR spectrum suggests that even in the presence of an AGN, PAH molecules are

abundant in these galaxies. Under the PAH *destruction* scenario (see Voit 1992), highly energetic photons from an AGN overcome the PAH binding energy, deplete the population of PAH molecules and thus reduce the observed PAH luminosity. Rather than a decrease in PAH luminosity, we find that SMGs with flatter continua generally have lower PAH EWs. Similar results have been recently discussed in the context of low-redshift ULIRGs by Desai et al. (2007), where a decrease in EWs for the 6.2 and 11.3 μm PAH features is observed with increasing 24 μm rest-frame luminosity. Together with these results, our findings suggest that an increase in the dust continuum dilutes the prominence of PAH features with respect to the local continuum. Our study allows us to extend the validity of this PAH-*dilution* scenario out to the higher redshifts of SMGs.

3.5.1 PAH Luminosities as a Star-Formation Rate Indicator

In Fig. 3.14 we compare the strength of the observed PAH features with familiar SFR indicators: Hα and the total IR-luminosity (Kennicutt 1998). In the past, authors have explored the use of the mid-IR light as a measure of galaxy SFRs. Elbaz et al. (2002) claim that the flux measured in the 6.75 μm *ISO* band is related to the total IR luminosity, which in the absence of an AGN is taken to be a good tracer of star-forming activity (Kennicutt 1998). Roussel et al. (2001) and Förster Schreiber et al. (2004) showed that there exists a correlation between *ISO* 6.75 μm light and Hα luminosity in local spirals and starburst galaxies. With the advent of much more sensitive Spitzer 8 μm IRAC results, Wu et al. (2005) and Alonso-Herrero et al. (2006) confirmed that the 8 μm band flux is closely associated with the star formation taking place in low-redshift ($z \lesssim 0.2$) luminous infrared galaxies with $L_{8-1000\ \mu\mathrm{m}} < 10^{12}\ \mathrm{L}_{\odot}$.

The interest in using the 7.7 μm PAH emission as a SFR indicator is that with it we are able to remove the continuum contribution to the 8 μm band, which in the presence of an AGN may be substantial and even dominant (see for example the continuum-dominated SMGs in Fig. 3.2: SMM J123553.26, SMM J163650.43 and SMM J221737.39). We find that the 7.7 μm PAH flux in SMGs correlates with the

extinction-corrected Hα flux (see Fig. 3.14). We emphasize that even though the same UV stellar radiation field is the source of excitation for the Hα and the PAH emission features, the excitation processes are quite distinct: Hα emission arises from ionized gas surrounding young O stars, while PAH emission is produced by the stochastic heating of very small dust grains (Draine & Li 2007). It has been further shown that PAHs can still be excited by the longer-wavelength photons of B stars. Therefore, even though the apparent correlation does not have a physically trivial explanation, it suggests that PAH emission can indeed be used as a tracer of recent star formation.

We do not find any correlation between PAH EWs and the Hα luminosities: SMGs with low EWs may also display luminous Hα emission. This suggests that even for SMGs with a significant AGN mid-IR contribution high SFRs are inferred. We note that the use of Hα as a SFR indicator is vulnerable to uncertainties, even if it has been corrected for extinction using the Hβ/Hα Balmer decrement (Takata et al. 2006). Additional extinction, unaccounted for by the Balmer decrement, may be present and thus remains a caveat. Indeed, as we show in the next section, the degrees of extinction (A_V) estimated for the mid-IR emission in SMGs are significantly higher than measured from the Balmer decrement, as the latter only measures the extinction to regions which are detectable in Hα, with the most extincted regions not contributing at all.

3.5.2 Dust Distribution in SMGs

The range in silicate optical depths we find in SMGs, $\tau_{9.7\mu\mathrm{m}} \sim 0.05$–$1.5$, falls below the typical values reported for both local ULIRGs and AGNs ($< \tau_{9.7\ \mu\mathrm{m}} > \sim 1.5$; Shi et al. 2006; Hao et al. 2007). Recent work by Desai et al. (2007) measured the strength of silicate-absorption features in a large sample of low-redshift ULIRGs from the Bright *IRAS* Sample to find that *cold* ULIRGs, with the steeper mid-IR spectra $S_{25\mu\mathrm{m}}/S_{60\mu\mathrm{m}} \lesssim 0.2$, have deeper silicate-absorption features than *warm* ULIRGs, with $S_{25\mu\mathrm{m}}/S_{60\mu\mathrm{m}} \gtrsim 0.2$. We find that SMGs have $\tau_{9.7\mu\mathrm{m}}$ values close to that of *warm* ULIRGs, such as *IRAS* FSC05189−252, and to the median value found for star-

forming low-redshift galaxies ($<\tau_{9.8\ \mu\mathrm{m}}>= 0.24 \pm 0.10$; see Fig. 3.10). Our observed silicate optical depths correspond to a median visual extinction of $A_V \sim 6$, assuming $A_V = (18 \pm 2) \times \tau_{9.7\ \mu\mathrm{m}}$ (Draine 2003).

The strength of the silicate feature can provide insight into the distribution of dust along the line of sight. The strong silicate absorption measured for *cold* low-redshift ULIRGs can be explained by a small, deeply embedded source with large amounts of obscuring dust along the line of sight (Levenson et al. 2007). Shallower silicate-absorption features and the presence of silicate emission, such as found in both the high-redshift mid-IR-selected sources presented by Sajina et al. (2007) and in *cold* low-redshift ULIRGs suggest that in the mid-IR there is a direct view to the hot thermal continuum source, possibly through a clumpy obscuring medium.

The observed 7.7/6.2 PAH ratios of the SMGs (Fig. 3.9) are also significantly lower than those seen in local nuclear starburst and ULIRG populations. This ratio is potentially sensitive to ionization and reddening, with softer radiation fields and lower obscuration leading to lower 7.7/6.2 ratios. When taken with the differences in silicate absorption, both these results can be explained by a single cause: lower extinction towards the mid-IR line and continuum emitting regions within SMGs, compared to either local nuclear starbursts or ULIRGs. These latter populations are dominated by star-formation activity in highly compact regions and the lower extinction in the SMGs suggests the mid-IR visible star formation in these galaxies is likely to occur in a more extended component, more similar to the activity in the disks of "normal" star-forming galaxies in the local Universe.

Evidence for extended star formation within SMGs has also been found at other wavelengths. High-resolution MERLIN/VLA observations of two samples of SMGs have revealed radio morphologies extending out to $\sim 1''$ or ~ 8 kpc in size (Chapman et al. 2004; Biggs & Ivison 2008). These two studies find that $\sim 85\%$ of the combined sample of 24 SMGs have extended radio emission, while only $\sim 15\%$ appear to be dominated by an unresolved component. Adopting radio emission as a proxy for far-IR emission, these results suggest that massive star formation is occurring on ~ 5 kpc scales within SMGs. This is in contrast to results for local ULIRGs, where the far-IR

emission is confined to a compact nuclear region of $\sim$ 1–2 kpc in size (Charmandaris et al. 2002). Further evidence for physically extended star formation within SMGs has come from studies of their rest-frame optical emission lines. Swinbank et al. (2006) mapped Hα emission from eight SMGs with integral field spectroscopy and found Hα structures extending to 1–2$''$ or $\sim$ 8–16 kpc in size. These results differ, however, from the extent of molecular gas emission in SMGs: sub-arcsecond resolution millimeter imaging of CO emission from six SMGs with the IRAM Plateau de Bure Interferometer suggests compact warm gas distributions in these galaxies, with sizes $\lesssim$ 2 kpc (Tacconi et al. 2006, 2008). These observations typically target the high-J CO transitions, which trace warm and dense gas, so it remains possible that there are more extended reservoirs of cold gas on $\gg$ 2 kpc scales within these systems which could fuel their extended star formation. Our mid-IR results give further evidence towards a more extended distribution of the star-forming regions in SMGs, in contrast to the compact nuclear starbursts seen in similarly luminous local galaxies.

3.6 Conclusions

SMGs are an enigmatic population which have been proposed to undergo a tremendous amount of star-forming activity, in order to explain their ultra-luminous infrared emission. The high stellar masses and SFRs inferred for these galaxies have prompted the idea that SMGs are the likely progenitors of today's most massive galaxies. However, the contribution from AGN activity to the bolometric luminosity has remained a caveat to these results. We present the largest sample of SMGs observed in the mid-IR with *Spitzer* IRS. Our main results are:

1. At the individual level, we find that 80% of SMGs in our sample display strong PAH features, with $L_{7.7\mu\mathrm{m}} \sim 10^{43}$–$10^{45}\,\mathrm{erg\,s^{-1}}$. This confirms for a large sample of SMGs that this is a population undergoing intense star formation, including some of the most intense star-formation events ever witnessed in the Universe.

2. We find only three cases of SMGs with continuum-dominated spectra (12% of our sample), which indicates that even though SMGs appear to be starburst-

dominated as an ensemble, some diversity is present within the sample.

3. We find that SMGs have a spread in optical depths as measured by the strength of the silicate absorption feature at $\lambda \sim 9.7$ μm. However, the mean value is significantly less than local ULIRGs or low-redshift nuclear starburst-dominated galaxies. This difference suggests that SMGs have lower dust obscuration to their mid-IR continuum emitting regions than local ULIRGs.

4. Comparison of PAH flux ratios, $S_{7.7\mu\mathrm{m}}/S_{11.3\mu\mathrm{m}}$, suggests that SMGs host similar radiation environments to local star-forming galaxies. However, the $S_{7.7\mu\mathrm{m}}/S_{6.2\mu\mathrm{m}}$ PAH ratio is lower in SMGs than in local nuclear starbursts or ULIRGs. This can most easily be explained if the extinction to these regions is lower in SMGs than in the local populations.

5. Our composite SMG spectra allow us to make more reliable measurements of the potential AGN contribution as revealed by an enhanced hot-dust continuum at $\lambda_{rest} \sim 10.5$ μm. We make conservative assumptions regarding the AGN contribution and find that the relative contribution of an AGN with respect to star-formation activity remains low. With a maximum AGN contribution of $\lesssim 35\%$ to the total luminous output, SMGs are clearly a galaxy population dominated by intense starburst activity.

6. We conclude that the detailed mid-IR spectra of SMGs show several differences with either local ULIRGs or nuclear starbursts. These differences can be most easily explained by a difference in the extinction to the mid-IR continuum and line emitting regions of these galaxies, with the SMGs showing systematically lower extinction. Given the compact geometry of the mid-IR emission from local ULIRGs, the difference in extinction we see argues that the mid-IR emission in SMGs, both continuum and PAH-emission, arises in a more extended component ($\gg$ 1–2 kpc). This supports radio and Hα studies which indicate that star formation in SMGs is extended on scales of ~ 5 kpc, far larger than seen in local ULIRGs.

Acknowledgements We thank Alexandra Pope, Elisabetta Valiante, Anna Sajina and Bernard Brandl for facilitating results and/or reduced spectra of their *Spitzer*

samples for proper comparison to our galaxies in this work. We are also grateful to Laura Hainline, Patrick Ogle, Vandana Desai and James Geach for helpful discussions.

Chapter 4

Hα and [OIII] Spectroscopic Insight From High-Redshift Ultra-Luminous Infrared Sources

SMGs are inferred to have high star-formation rates, SFR $\sim 100 - 1000$ $M_\odot$ yr^{-1} and large stellar masses, $M_{stellar} \gtrsim 10^{11}$ $M_\odot$. These findings suggest that SMGs are undergoing intense starburst episodes and that they may be major sites of stellar build up. As part of a continuing program to understand these sources and their context, we sought rest-frame optical line emission from a sample of submm- and mm-detected galaxies at a mean redshift, $< z > \sim 2.0$, with the Near-Infrared Spectrograph (NIRSPEC) on the Keck Telescope to identify the presence of AGN in the center of these galaxies through detection of broad Hα and [OIII] lines, and using the line ratio diagnostics from [NII]/Hα and [SII]/Hα. Our results emphasize the challenges faced by long-slit spectroscopic techniques when both AGN and star-forming activity are present: we demonstrate that rest-frame optical emission line-widths may be enhanced by emission from the broad-line region near a central AGN and thus result in overestimates of dynamical masses.

4.1 Introduction

Ultra-luminous infrared galaxies (ULIRGs; $L_{8-1000\ \mu m} > 10^{12}$ $L_\odot$) contribute a negligible fraction of local star formation, but are major sites of massive star formation

Table 4.1. Summary of *NIRSPEC* Observations

Name	RA[a] ($h\,m\,s$)	Dec. ($^\circ\,'\,''$)	NIRSPEC Filter	Exposure times ks	Date
SMM J030227.73	03:02:27.73	+00:06:53.5	N5	3.0	Aug. 2004
SMM J123716.01	12:37:16.01	+62:03:23.3	N6	1.8	April 2006
SMM J123549.44	12:35:49.44	+62:15:36.8	N7	7.2	April 2006
			[OIII] (N5)	7.2	April 2006
SMM J123635.59	12:36:35.59	+62:14:24.1	N4	9.0	April 2006
MIPS 142824.0	14:28:24.0	+35:26:19	N7	2.4	March 2005

[a] Radio center from C05 compilation

and metal production at higher redshifts, where they have been identified only by the detection of their thermal dust emission in the millimeter (mm) and sub-mm wavebands (Smail et al. 1997; Barger, Cowie & Sanders 1999; Eales et al. 1999; Bertoldi et al. 2000; Cowie et al. 2002; Scott et al. 2002; Borys et al. 2003; Webb et al. 2003b; Coppin et al. 2005; Younger et al. 2007). Furthermore, the space density of these extreme galaxies appears to increase by a factor of ~ 1000 from $z \sim 0$ to $z \sim 2$ (C05; Le Floc'h et al. 2005; Caputi et al. 2007).

Rest-frame UV redshifts have been extremely valuable to understand the luminosity, astrophysical nature and to enable follow-up observations of SMGs. They have revealed that the redshift distribution of radio-identified SMGs coincides with the epoch of peak quasar activity, with a significant contribution to the global SFR density at $z = 2 - 3$ not traced in the UV (C05). However, UV lines are typically subject to offsets from galactic outflows and winds: velocity offsets of up to $few \times 1000$ km s^{-1} have been found in SMGs between Lyα, Hα and molecular CO lines (Greve et al. 2005; Swinbank et al. 2004, hereafter S04; Takata et al. 2006). Even though these offsets provide information about the winds in SMGs and their effect on the surrounding inter-galactic medium (Heckman 2001), they can also confuse the accurate identification of groups of galaxies associated with the same large-scale structures (Blain et al. 2002). Furthermore, these offsets can be sufficiently large to fail to deliver the necessary redshift accuracy needed to undertake some detailed follow-up observations. For example, observations of CO emission have traditionally

required high precision, due to the narrow observed mm-wave frequency band. It is thus important to obtain more accurate redshifts for the interstellar medium in the SMGs. Rest-frame optical lines should provide a more accurate redshift for the bulk of the gas in the interstellar medium of the potential well of the galaxy. Further, at $z \sim 2$ the near-IR traces a rich array of rest-frame optical emission lines, including the Balmer lines (e.g., Hα, Hβ) and a number of forbidden lines (e.g., [NII], [SII], [OIII]) that enable us to probe their astrophysics.

Low-resolution near-IR observations can resolve the ratio of the adjacent [NII] and Hα line strengths, the so-called N2-index, which has been shown to correlate well with the (12+log[O/H]) metallicity indicator. The [NII] line traces diffuse ionized medium and, together with Hα, it is sensitive to the hardness of the radiation. Together with the [SII]/Hα line ratio, the N2-index can be used as a coarse metallicity estimate and can indicate the presence of an AGN radiation field if [NII] and/or [SII] are very strong (e.g., Veilleux et al. 1995).

S04 reported a large program of near-IR follow up observations of 30 radio-identified SMGs from the C05 sample, using long-slit Hα observations with the Near-Infrared Spectrograph (NIRSPEC; McLean et al. 1998) instrument at Keck. We present here a continuation of this program, including observations of multiple lines in four radio-identified submm-detected galaxies from C05 and the mm-detected galaxy, MIPS 142824.0 (Borys et al. 2006). We present our sample and observing strategy in §4.2 and describe our reduction and analysis in §4.3. Our results are shown in §4.4 and discussed in detail in §4.5.

4.2 Sample Selection and Observing Strategy

Four out of the five sources presented here were drawn from the sample of radio-identified SMGs in C05. Based on rest-frame UV observations with the blue-sensitive Low-Resolution Imaging Spectrograph on Keck (LRIS-B; Oke et al. 1995; McCarthy et al. 1998), C05 spectroscopically-confirmed these objects to be in the redshift range $1.4 \lesssim z \lesssim 2.2$. We make no target selection based on UV properties, and thus

maintain diverse UV properties within our sample.

We also include in our sample a hyper-luminous galaxy ($L_{8-1000\ \mu m} \gtrsim 10^{13}\ L_{\odot}$) detected in all three bands of the Multiband Imager for *Spitzer* (MIPS: $24, 70, 160\ \mu$m; Rieke et al. 2004). With no evident AGN signatures at wavelengths ranging from the optical to the radio, this galaxy has been interpreted as powered entirely by star formation and thus a likely analog to the SMGs that are found at higher redshifts (see Borys et al. 2006).

Our selection criteria also include observing feasibility. Our targets are too faint to be detected in short exposures, making it necessary to use nearby bright stars as references for blind telescope pointing offsets, based on deep K-band imaging (e.g., Smail et al. 2004). Therefore, we select objects that have a near-IR bright star within $1'$. We also selected our targets to have both Hα and [OIII] lines redshifted into regions of the near-IR atmospheric windows that are relatively free of sky line emission.

Our science observations consist on repeating a series of ABBA sequences, each sequence comprising 4×15-min frames (each frame usually built from three coadds of 300s each) with the science target at two different positions on the NIRSPEC slit, separated by $\sim 15 - 20''$. For flux-calibration purposes, we perform a short exposure of a Vega-type ($A0$) standard star, with weak stellar absorption features, using the exact instrument setup for each science target. Furthermore, we take repeated frames of the standard star at different positions along the slit with spacings of $\sim 15''$ for rectification purposes.

For the redshifts covered by our sample, Balmer and [OIII] emission lines are redshifted into the H- and K-band. We used the low-resolution setting of NIRSPEC with the $42'' \times 0.76''$ slit, achieving a resolution of $R \sim 2000$ (see Section 4.3). We collected our data from August 2004 to April 2006. Observing conditions were of varying quality, with occasional clouds and seeing $\sim 0.8 - 1.5''$ in the V-band. Details of our observations are summarized in Table 4.1.

4.3 Reduction and Analysis

We reduced the spectra using the IRAF package. Preliminary reduction steps comprise elimination of bad pixels using the combined dark frames and removal of cosmic rays. Spatial correction is required to place the wavelength direction along the y-axis and the spatial direction along the x-axis. We do a rough spatial rectification of the spectrum by applying a rotation of 5.1 degrees, followed by a curvature correction defined by the trace of the standard star. We base our wavelength solution on the identification of Argon lines from calibration lamps, using the IRAF tasks IDENTIFY and REIDENTIFY.

We rely on nod-subtraction within each ABBA sequence for the bulk of sky subtraction. We create two (A - B) pairs from each ABBA sequence. Each of these nod-subtracted images display a positive and a negative trace of the science targets. We reduce persistent OH-line emission in these 2D spectra by fitting a polynomial along the spatial direction and subtracting it with IRAF's BACKGROUND task. We show the 2D spectra of our targets in the top panels of Figs. 4.1-4.5. We define our instrumental spectral resolution by measuring the width of individual OH lines ($\sim$ 10 Å). In the K-band this translates to an achieved resolution of $R \sim 2000$. We use the measured width of sky lines to correct for instrument resolution in determining the FWHM of the emission lines. We apply this correction by adding the science emission line FWHM and the sky-line width in quadrature, $\mathrm{FWHM}_{corr} = \sqrt{(FWHM_{obs})^2 - (10\ \text{Å})^2}$, where typically $\Delta\mathrm{FWHM}/\mathrm{FWHM}_{corr} \lesssim 1\%$.

We combine (A - B) pairs and use IRAF task APALL to extract a 1D spectrum within an interactively-set spatial aperture ($\sim 2''$) in the reduced 2D spectrum. We flux-calibrate the final 1D spectra for our targets using the standard star spectra taken during the same night with the same instrument configurations. We reduce the standard star observations in the same manner as science images. We use the Vega SED (Colina 1996) as a reference and construct a scaled Vega-type spectrum according to the magnitude of the observed standard. We derive flux calibration

corrections at each wavelength by dividing the observed 1D standard spectra by this scaled reference spectrum and apply these calibration corrections to the science 1D spectra. The flux-calibrated 1D spectra for our targets are presented in the bottom panels of Figs. 4.1-4.5.

We characterize the emission features detected in our spectra – Balmer line Hα, and forbidden doublets [NII], [OIII] and [SII] – in terms of integrated line flux, full-width half-maximum and central wavelength of emission. We fit each emission feature with a gaussian curve using the IRAF task SPLOT, allowing the amplitude, width and central wavelengths as free parameters. In the case of several emission features within the same spectra, as is the case for SMM 030227.73 and SMM 123549.44, we fix the relative wavelength offsets between the lines to introduce redshift as a free parameter.

Even after careful flux calibration, significant uncertainties remain in the absolute flux values. The near-IR sky varies on short time scales and so observed standard spectra do not provide an exact correction to the atmospheric absorption when science exposures are taken. Quantification of these uncertainties is difficult. We attempt to estimate these uncertainties by considering the noise in the sky-background during line fitting. For this reason we input the rms of the off-line regions into our fitting routine, to better characterize uncertainties in line integrated flux and FWHM. Furthermore, significant calibration uncertainty is due to slit losses in which the entire target is *not* fully enclosed by the relatively narrow $0.76''$ slit. This may occur either due to: (1) a misalignment of the object within the NIRSPEC slit; (2) considerable seeing $\gtrsim\ 1''$; or (3) as a result that the target is larger than the slit size. In the case of SMGs, the latter is a known source of uncertainty, since the typical extent of Hα emission has been shown to be $\gtrsim\ 4-8$ kpc, which at $z\ \sim\ 2$ corresponds to $0.5-1''$.

4.3.1 Deblending Emission Lines

The Hα lines in our sample are blended with contributions from the [NII] line doublet at $\lambda\ =\ 6549, 6583$ Å. With a line ratio based on transition probabilities of $[\mathrm{NII}]_{6549}$:$[\mathrm{NII}]_{6583}$ equal to 1 : 3 (Osterbrock 1989), we deemed it *reasonable* to decon-

volve the emission complex into two principal emission lines: Hα and NII[6583], using the DEBLENDING mode in the IRAF task SPLOT: we specify the wavelength region for the deblending to be performed, the relative spacing of the lines, and we allow gaussian curves to be fit with redshift, amplitude and FWHM as free parameters.

Similarly, we consider the relative transition probabilities for the forbidden doublets [SII] and [OIII] at $\lambda_{[SII]} = 6716, 6731$ Å and $\lambda_{[OIII]} = 4959, 5007$ Å, with $[\mathrm{SII}]_{6731}$:$[\mathrm{SII}]_{6717} = 3.4$ and $[\mathrm{OIII}]_{5007}$:$[\mathrm{OIII}]_{4959} = 2.86$, respectively (Osterbrock 1989). Since the resolution of our observations does not allow us to discern these two emission features, we consider only the strongest lines during deblending. This results in upper limits for the strengths of $[\mathrm{NII}]_{5007}$ and $[\mathrm{SII}]_{6731}$ if deblending the Hα+[NII] complex is possible and when an [SII] emission feature is detected above the noise level, respectively.

4.4 Results

We present the 2D and 1D near-IR spectra for the SMGs in our study in Figs. 4.1-4.5 and present our results in Table 4.2. The spectra for MIPS J142824.0+352619 is described by Borys et al. (2006). We include it here for completeness.

4.4.1 SMM J030227.73

We detect a prominent emission feature atop a significant continuum for this source (see Fig. 4.1). With an optical redshift of $z_{opt} = 1.408$ (C05), we identify this feature with Hα line emission. There is definite sub-structure within this feature, which we attribute to the blending of the Hα line with the forbidden line doublet [NII]. Furthermore, a faint line is detected at the expected location for the [SII] doublet.

We obtain upper limits for [SII] emission, but our attempt to deblend the Hα+[NII] complex into two distinct components was not successful within reasonable uncertainties. Excluding the contribution from [NII], we extract upper limits to the Hα and [SII] emission for this source. Considering both emission features, we confirm that this source is at $z = 1.407 \pm 0.001$, within 125 km s^{-1} of the optical redshift.

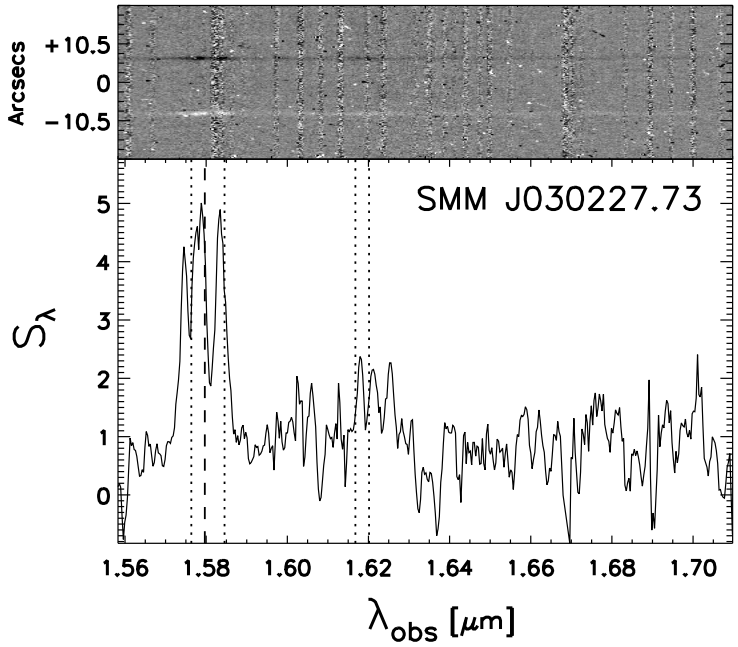

Figure 4.1 Near-IR spectrum of SMM J030227.73. (**Top:**) Fully-reduced, sky-subtracted 2D spectrum with wavelength increasing along the x-axis. Both the positive and negative traces of this object, separated by 10.5″ from the center of the slit, are visible. A broad emission line is evident in both these traces. (**Bottom:**) The flux-calibrated 1D spectrum in the observed frame with flux expressed in units of 10^{-15} erg s^{-1} cm^{-2} μm^{-1}. The central wavelength of the Hα line is indicated by a vertical dashed line and the positions of the [NII] and [SII] doublets are shown by dotted lines. The spectrum is smoothed to 10 Å bins, corresponding to the spectral resolution of the observations.

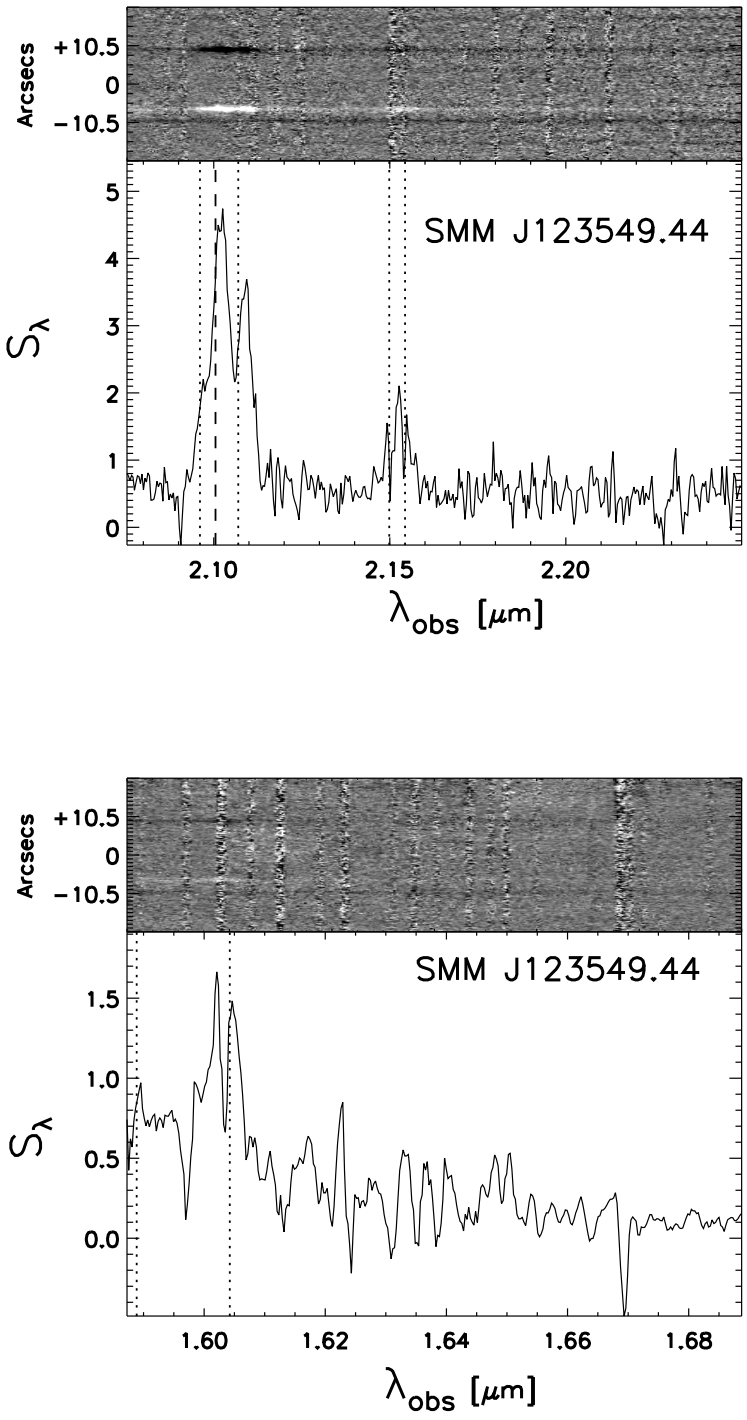

Figure 4.2 Near-IR $K-$ and $H-$band spectra of SMM J123549.44, following the same format as Fig. 4.1.(**Top:**) K-band spectrum of SMM J123549.44 showing clear emission from the Hα+[NII] complex. (**Bottom:**) H-band observations, revealing a fainter, but definite emission from $[OIII]_{5007}$.

4.4.2 SMM J123549.44

This SMG lies within the GOODS-North field and thus benefits from a wealth of multi-wavelength coverage. It has been identified as having AGN signatures in the X-ray (Alexander et al. 2005a), near-IR (S04) and mid-IR (Menéndez-Delmestre et al. 2008) wavebands. Tacconi et al. (2006, 2008) have also undertaken high-resolution CO observations of this galaxy and find CO emission dominated by a compact source ($\lesssim 0.5''$) with a prominent double-peaked CO profile, which they associate with orbital motions of gas within a disk.

H- and the *K*-band follow-up of this SMG reveals clear emission features at the expected locations for Hα, [SII] and [OIII] according the $z_{opt} = 2.2032$ (see Fig. 4.2). The Hα, [SII] and [OIII] emission features for SMM J123549.44 are observed to be broad, with $\sigma_{rest} \sim 800 - 1000$ km s^{-1} (see Table 4.3), which suggests that the observed near-IR emission is associated with AGN activity. Based on the central wavelengths for the observed Hα and [SII] emissions, we constrain the redshift to $z_{H\alpha,[SII]} = 2.205 \pm 0.001$. Considering the location of the [OIII] emission line, we find $z_{[OIII]} = 2.202 \pm 0.001$. The comparison of the rest-frame UV redshift to $z_{H\alpha,[SII]}, z_{[OIII]}$ indicates that there are slight redshift offsets between these lines. Forbidden [OIII] emission is offset from the Hα emission, with $\Delta v \sim 340$ km s^{-1}, while Lyα is at a relative velocity $\Delta v \sim 625$ km s^{-1} with respect to Hα. These differences lie outside the estimated uncertainties $\Delta\lambda \gtrsim 10$ Å, and therefore indicate intrinsic velocity offsets between the emission regions. However, we note that these differences remain quite small in comparison to velocity offsets typically found in quasars, $\Delta v \gg 1000$ km s^{-1}. These velocity offsets fall within the velocity dispersions (FWHM) of the individual emission features, which indicates that the redshift differences are not necessarily the result of systemic velocity differences (which would suggest the presence of outflows), but can be explained in terms of the velocity dispersion within different parts of the galaxy.

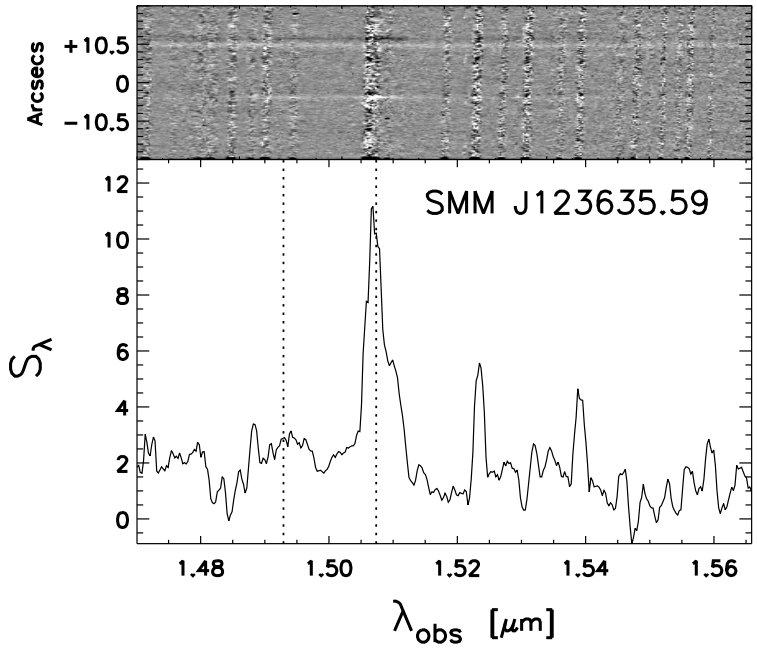

Figure 4.3 Near-IR spectrum of SMM J123635.6, following the same format as Fig. 4.1. We see clear line emission from [OIII] at $\lambda_{rest} = 5007$ Å and at a significantly lower level, a flux excess at the redshifted location expected for $[\mathrm{OIII}]_{4959}$ emission (dotted lines).

4.4.3 SMM J123635.59

This SMG was first identified as an extended μJy radio source and was initially assumed to be powered by star formation (Richards 2000). However, AGN signatures have been reported in the rest-frame UV and optical: Chapman et al. (2005) detect strong CIV ($\lambda_{CIV} = 1550$ Å), which is often associated with quasars. Dawson et al. (2003) and S04 have identified an underlying broad component to the Hα emission (FWHM$_{H\alpha} \gtrsim 2500$ km s^{-1}), and ultra-deep X-ray observations with *Chandra* revealed that this SMG is a source of hard X-ray emission (Alexander et al. 2005a).

To provide more insight, we undertook H-band observations and obtained a clear detection of the forbidden [OIII] emission at $\lambda_{obs} \sim 1.507$ μm. We also have marginal detection of the weaker component of the doublet, [OIII]$_{4959}$, evident as a slight flux excess in the continuum at $\lambda_{obs} \sim 1.493$ μm (see Fig. 4.3). We derive a redshift $z_{[OIII]} = 2.011 \pm 0.001$, which is significantly offset from $z_{opt} = 2.005$ and corresponds to a velocity offset $\Delta v \sim 1640$ km s^{-1}. In contrast to SMM J123549.44, the [OIII] line is relatively narrow ($\sigma_{[OIII]} \sim 330$ km s^{-1}; see Table 4.3), which suggests that this offset is associated with an outflow.

4.4.4 SMM J123716.01

Rest-frame UV observations set this SMG at $z_{opt} = 2.037$. In Fig. 4.4 we show the K-band NIRSPEC spectrum, which clearly shows the Hα+ [NII] emission complex. We make the conservative assumption that the emission complex is dominated by Hα emission and obtain an observed Hα flux of $S_{H\alpha} = 5.0 \times 10^{-15}$ erg s^{-1} cm^{-2}. We compare this value to the Hα flux estimated from Hβ measurements by (Takata et al. 2006), based on the theoretical H$_\alpha$/H$_\beta \sim 2.86$ ratio for an HII-region (Osterbrock 1989). In the case of no extinction, with $S_{H\beta} = 2.81 \pm 0.32 \times 10^{-15}$ erg s^{-1} cm^{-2}, the expected Hα emission corresponds to $S_{H\alpha} \sim 8.0 \times 10^{-15}$ erg s^{-1} cm^{-2}. Therefore, it is clear that the detected Hα emission is being decreased.

This decrease cannot be explained by the contamination from an over-subtracted atmospheric OH line emission. The closest sky line is centered at ~ 2.09 μm, which

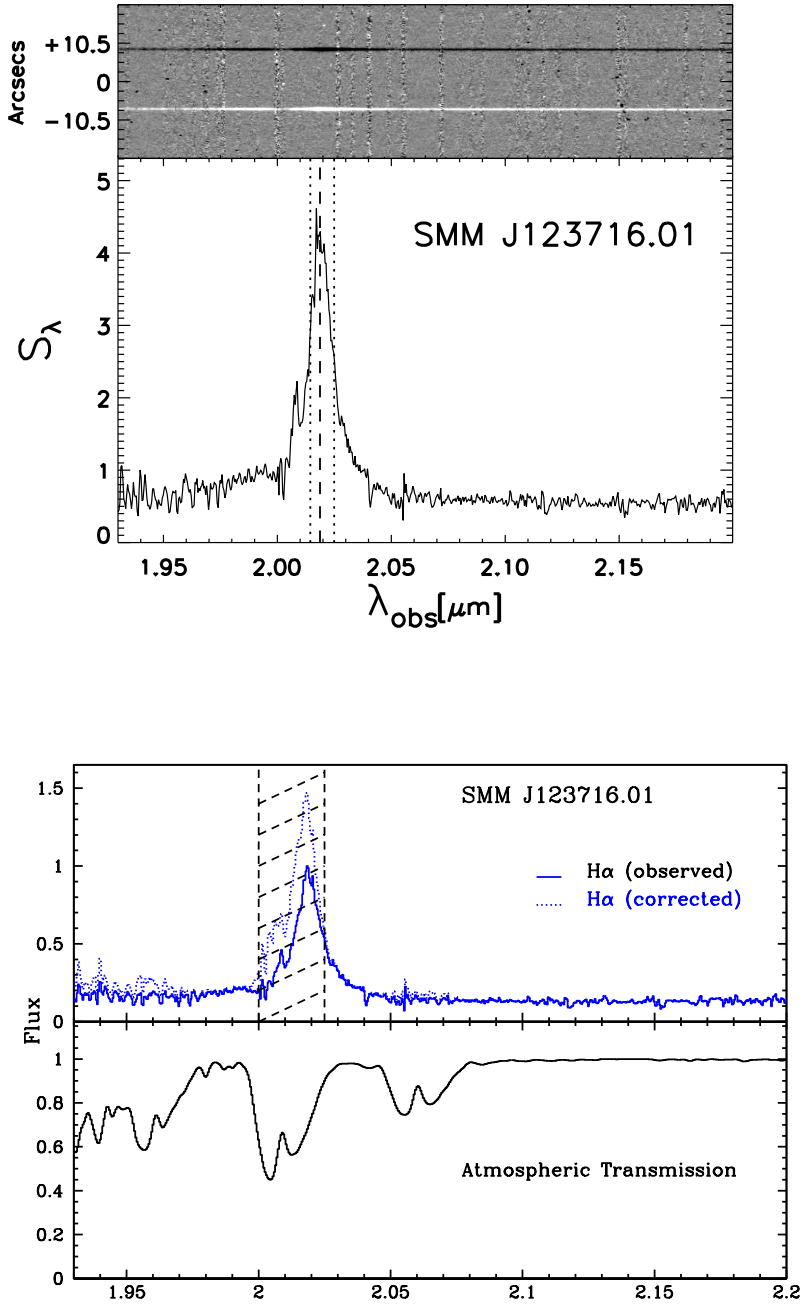

Figure 4.4 (**Top:**) Observed near-IR spectrum of SMM J123716.01, following the same format as Fig. 4.1. (**Bottom:**) Hα emission line spectrum corrected for atmospheric absorption. At this wavelength, atmospheric absorption becomes significant, as the trough in atmospheric transmission in the bottom panel show. To correct for this, we divide our spectrum by the atmospheric transmission to mimic the emission line free of absorption (top panel, dotted-line spectrum). See §4.4.4 for details.

would only affect the red wing of the emission feature. We note that at $z = 2.037$, Hα is redshifted to an observed wavelength range that coincides with a significant trough in the atmospheric transmission (see bottom panel of Fig. 4.4) centered at $\lambda \sim 2.01$ μm. The depth of this trough reduces the atmospheric transmission coefficient by $\sim 40\%$. This results in a measured flux substantially lower than the otherwise unabsorbed Hα+ [NII] emission.

We approximate a correction to this atmospheric absorption by dividing our observed spectrum by the atmospheric transmission and creating an *unabsorbed* version of the spectrum. The *true* emission strength likely lies between these two boundaries. Therefore, we characterize the line emission in both spectra, obtaining line integrated fluxes and FWHMs in both spectra and adopt the average between these two to describe the *unabsorbed* line emission. Considering the complexity presented by this emission feature, we do not attempt to deconvolve the Hα+[NII] complex. We find $z_{H\alpha} = 2.073$ and include these adopted values in Tables 4.2, 4.3.

Note that the resulting absorption-corrected values still lie below the expected value determined from the Hβ in Takata et al. (2006). To explain this mismatch in values, we consider other factors that may be leading to a lower Hα. As discussed in Section 4.3, slit losses may be responsible for a decreased detection of emission from an extended target. We carefully inspected the SCAM images and ensured that the offset star, used for the blind offsets to the science target as described in Section 4.2, was well-centered in the slit. With a seeing of $\simeq 1''$ for these observations, it is likely that SMM J123716.01 was not fully enclosed by the width of the slit. Furthermore, the slit-width of the Subaru OHS spectrograph with which Hβ observations for this object were made is $0.95''$ in comparison to NIRSPEC's $0.76''$. NIRSPEC measurements would amount to 80% of that measured by OHS. This may further explain why our Hα flux corrected for atmospheric absorption still remains below the expected value based on the theoretical Hα/Hβ ratio.

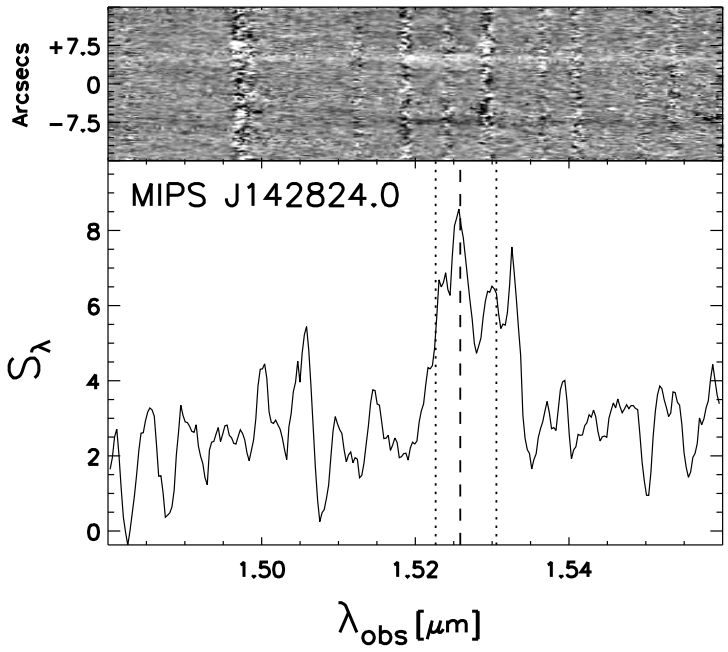

Figure 4.5 Near-IR spectrum of MIPS J142824.0, following the same format as Fig. 4.1. we see that this mm-detected source displays broad Hα emission, blended with flanking [NII] lines at $\lambda = 6459, 6583$ Å.

Table 4.2. Redshifts and Near-IR Integrated Line Fluxes

SMM J	z_{opt}[a]	$z_{H\alpha}$	$z_{[OIII]}$	$z_{[SII]}$	$S_{H\alpha}$[b]	$S_{[NII]}$	$S_{[OIII]}$	$S_{[SII]}$
030227.73	1.4080	1.406	–	2.409	3.054 ± 0.42	1.708 ± 0.42	–	1.341 ± 0.41
123549.44	2.2032	2.203	2.202	2.197	–	–	–	–
123635.59	2.0050	2.015[c]	2.011	–	0.42 ± 0.03[c]	–	0.035 ± 0.002	–
123716.01	2.0370	2.073	–	–	6.60 ± 0.26	–	–	–
MIPS142824.0	–	1.324	–	–	3.01 ± 0.31	2.46 ± 0.35	–	–

[a] From C05

[b] Integrated line flux expressed in unis of 10^{-15} erg s^{-1} cm^{-2}.

[c] From Swinbank et al. (2004).

4.4.5 MIPS J142824.0+352619

This object was first detected in *Spitzer* GTO observations of the NOAO Deep Wide-Field Survey (NDWFS) Boötes field and is discussed in detail by Borys et al. (2006). With strong mid-IR flux and extremely red optical colors ($R-K > 6$), it was inferred that this object was very dust-enshrouded. Follow-up submm observations at 350 μm with the SHARC-II camera (Dowell et al. 2003) on the Caltech Submm Observatory (CSO) and at 850 μm with the SCUBA instrument on the James Clerk Maxwell Telescope (JCMT) provided the shape of the SED of this object. Photometric redshift estimates suggested that this object was at $z > 1$, which suggested that this object was remarkably luminous in the IR, with $L_{8-1000\ \mu m} \gtrsim 10^{13} L_{\odot}$. Devoid of any evident signatures of the presence of an AGN, the large observed IR luminosity suggested that this galaxy was a remarkable specimen that afforded an opportunity to study in detail an example of the relatively unexplored $z = 1 - 2$ dusty starburst population.

Spitzer mid-IR spectroscopy with IRS uncovered strong PAH emission features and placed the galaxy at $z \sim 1.33$ (Desai et al. 2006). However, the intrinsically broad PAH emission features and the relatively low resolution of IRS signified a large uncertainty on this redshift, $\Delta z \sim 0.1$. It is at this stage that a more accurate redshift, based on rest-frame optical emission lines, was necessary.

We show the near-IR spectrum of MIPS J142824.0+352619 in Fig. 4.5. We detect a clear emission feature at $\lambda_{obs} \sim 1.53$ μm, which we identify as Hα emission, likely

blended with the [NII] forbidden line doublet at $\lambda_{rest} = 6549, 6583$ Å. We derive a redshift of $z = 1.323 \pm 0.001$ by fitting gaussians jointly to Hα and the flanking $[\mathrm{NII}]_{6583}$ line. The best fit to this emission indicates a significantly high contribution from [NII] emission, amounting to [NII]/H$\alpha \sim 0.8$. We measure an Hα line width of $\mathrm{FWHM}_{rest} = 1000 \pm 135$ km s^{-1} in the rest-frame, but we caution that this is an upper limit to the intrinsic width, since it may contain contributions from the [NII] lines.

4.5 Discussion

As a result of star formation, the abundance of metals increases in the course of the star-formation history of a galaxy. Rest-frame optical emission line strengths can give us an insight to these chemical abundances. Following the approach of S04, we use the N2-index [1] to estimate the metallicities of the galaxies in our sample. For this, we rely on the calibration by Pettini & Pagel (2004):

$$12 + Log(O/H) = 8.90 + 0.57 \times N2. \tag{4.1}$$

We find that the galaxies in our sample have N2-indices that place them close to solar metallicity (see Table 4.4), within the range found by S04. These results together with other studies on the metal abundance hosted by SMGs (e.g., Tecza et al. 2004) show that SMGs are metal-rich galaxies, with $Z/Z_{\odot} \gtrsim 1$ (see also Bouché et al. 2007).

SMGs have been found to display large redshift offsets between Lyα, Hα and molecular CO lines of up to $few \sim 1000$ km s^{-1} (Smail et al. 2003, 2004; Greve et al. 2005). These redshift offsets indicate that large velocity outflows are sometimes found in these objects. In Fig. 4.6 we compare near-IR redshifts to optical redshifts presented by C05, including those available for four SMGs in our sample. We find that two SMGs in our sample have Hα and optical redshifts within $\Delta z \lesssim 10$ Å of each other,

[1] $N2 = Log([NII]/H\alpha)$

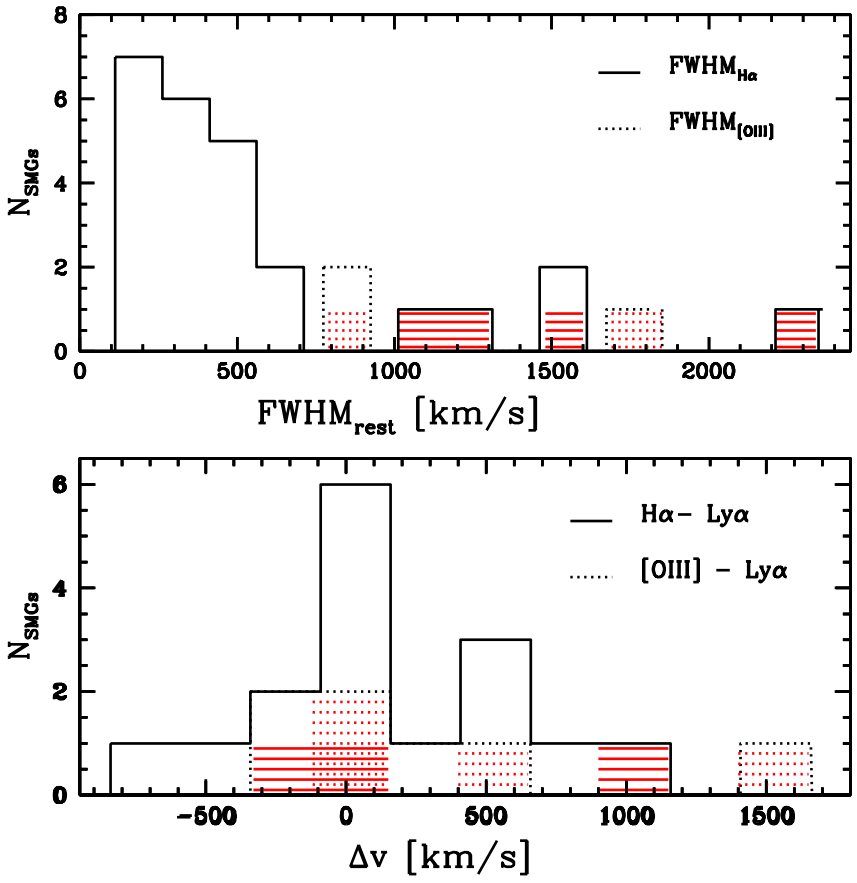

Figure 4.6 (**Bottom:**) Distribution of relative velocities in SMGs as given by differences in rest-frame UV redshifts from C05 and rest-frame optical redshifts, derived from Hα (solid histogram) and [OIII] (dotted histogram) observations. We include objects from S04 and Takata et al. (2006) in addition to the objects in our sample. The hatched regions distinguish the contribution from our sample to these histograms: Hα and [OIII] offsets from Lyα are shown by solid- and dotted-hatched regions, respectively. The velocity offset we find for the QSO-classified SMG SMM J123716.01 falls outside of the displayed region (see § 4.4 for details). (**Top:**) Following the same line-coding as the bottom figure, distribution of line widths (FWHM$_{rest}$) for SMGs.

which corresponds to our spectral resolution. In the cases of SMM J123635.59 and SMM J123716.01, we find $\Delta z = 0.01, 0.036$, respectively. These redshift differences translate into relative velocities of ~ 1000 km s^{-1} for SMM J123635.59 and ~ 3500 km s^{-1} for SMM J123716.01.[2] The SMG SMM J123716.01 has been identified as a QSO by C05, which explains the very large velocity outflow (see also Takata et al. 2006).

Strong outflows have also been identified in extreme objects, such as QSOs (Richards et al. 2002: $\gg$ *few* $\times$ 1000 km s^{-1}) and in populations of less-massive, high-redshift galaxies: optically-selected LBGs display velocity offsets ~ 750 km s^{-1} (Adelberger et al. 2003). Detection of CIV and OIV absorption near QSOs and LBGs (e.g., Adelberger et al. 2003) signals the effect that such ionizing outflows may have in enriching their surroundings. Given that SMGs are among the most luminous objects in the universe, it is to be expected that SMGs host stronger outflows than LBGs. Considering the chemical abundances of SMGs, such outflows are potentially powerful at transforming the intergalactic environments rapidly.

4.5.1 AGN Signatures in SMGs

The near-IR provides with a number of diagnostic lines that can be used to probe for the presence of an underlying AGN. Veilleux et al. (1995) explored the use of the [SII]/Hα ratio to classify galaxies into different spectral types. They analyzed a large sample of 200 bright IRAS sources and classified them into spectral types according to a number of intensity ratios, including [SII]/Hα and [NII]/Hα. Two sources in our sample – SMM J123549.44 and SMM J030227.73 – display [SII] emission, with [SII]/H$\alpha \sim 0.2, 0.4$, respectively (see Table 4.3). According to Veilleux et al. (1995), these ratios are clear AGN signatures commonly found in low-ionization nuclear emission-line regions (LINERs) and Seyfert galaxies.

The presence of an AGN can also be probed through detection of broad emission lines. Broad line emission may be associated with ordered orbital motions of gas but

[2] $\Delta \mathrm{v} = |\mathrm{z_{opt}} - \mathrm{z_{H\alpha}}|/(1 + \mathrm{z_{opt}})$

Table 4.3. Summary of Spectral Classifications

SMM J	FWHM$_{H\alpha}$[a] km s^{-1}	FWHM$_{[OIII]}$[a] km s^{-1}	[NII]/Hα	[SII]/Hα	Class	Comments
030227.73	1500 ± 266	–	0.56 ± 0.21	0.44 ± 0.19	SB;[b] AGN[c]	high [SII]/Hα-ratio; FWHM$_{H\alpha}$ > 500 km s^{-1}
123549.44	1183 ± 43	1850 ± 37	0.56 ± 0.04	0.19 ± 0.02	SB;[b] int	FWHM$_{H\alpha}$ > 500 km s^{-1}
123635.59 (nw)[d]	240 ± 33	775 ± 40	0.67 ± 0.27[e]	–	AGN[e]	[NII]/Hα > 0.7; Broad Hα, [OIII]
123635.59 (br)	1623 ± 213[e]	775 ± 40				
123716.01	2349 ± 94	–	–	–	QSO[b]AGN[f]	FWHM$_{H\alpha}$ > 500 km s^{-1}
MIPS142824.0	1042 ± 135	–	0.82 ± 0.20	–	SB [g]AGN	[NII]/Hα > 0.7; FWHM$_{H\alpha}$ > 500 km s^{-1}

[a] FWHM are expressed in rest-frame and derived assuming $z = z_{H\alpha}$.

[b] From rest-frame UV (C05).

[c] From Hα integral field spectroscopy Swinbank et al. (2006).

[d] Dawson et al. (2003) and Swinbank et al. (2004) distinguish a narrow and broad Hα component for this SMG.

[e] From long-slit Hα spectroscopy (Swinbank et al. 2004).

[f] From long-slit Hα spectroscopy (Takata et al. 2006).

[g] From Borys et al. (2006).

it can also be the result of having a direct view of the randomly moving high-velocity gas within the broad-line region of a central AGN. S04 have shown that 40% of SMGs display a broad Hα component, with FWHM$_{rest}$ $\sim$ 500 $-$ 3000 km s^{-1}. These line-widths are narrower than those typically found for classical quasars (FWHM$_{H\alpha}$ $\gtrsim$ 2$-$ 8 $\times$ 10^3 km s^{-1}; e.g., Puchnarewicz et al. 1997), but are markedly larger than those found for other populations of starburst-dominated galaxies (e.g., FWHM$_{rest}$ $\lesssim$ 500 km s^{-1} in LBGs; Erb et al. 2003). In Fig. 4.6 we see that the galaxies in our sample display among the broadest Hα and [OIII] line-widths that have been identifed in SMGs. These large velocity dispersions suggest that we are seeing the broad-line region close to a central AGN.

S04 separate SMGs into three classes (see Fig. 4.7): an AGN-dominated class with FWHM$_{H\alpha}$ $\gtrsim$ 1000 km s^{-1} and/or [NII]/Hα $>$ 0.7; a class of composite systems displaying intermediate line-widths, FWHM$_{H\alpha}$ $\sim$ 500 $-$ 1000 km s^{-1}; and a class of SMGs with no evident AGN signatures, likely dominated by star formation (FWHM$_{H\alpha}$ $\lesssim$ 500 km s^{-1} and [NII]/Hα $<$ 0.7). All the galaxies in our sample display line-widths or [NII]/Hα line ratios that place them in either the AGN- or composite-class (see Fig.4.7 and Table 4.3).

Three out of five of our targets include ultra-deep *Chandra* X-ray data and have been identified as hard X-ray sources (Alexander et al. 2005a). We have included these X-ray classifications as well as the classifications based on other observed wavelengths in Table 4.3. Our near-IR classification based on line-widths and line ratio diagnostics is in agreement with AGN signatures at other wavelengths. The only exception is MIPS 142428.04. Uncertainties in the deblending of the Hα+[NII] complex remains an important caveat to these results and are a potential source of disagreement. The combination of broad Hα and high [NII]/Hα line ratio strongly suggests that this object harbors an AGN. However, the contribution of the AGN to the total luminous output of this galaxy does not necessarily dominate over the the contribution from star-forming activity (Borys et al. 2006).

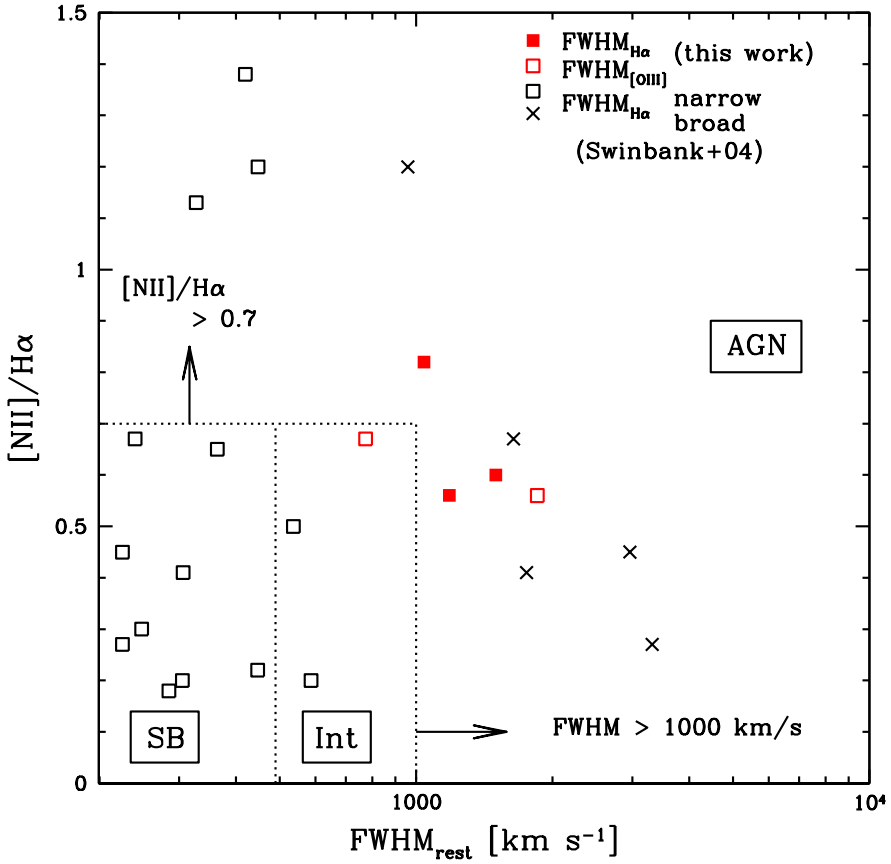

Figure 4.7 [NII]/Hα line ratios as a function of Hα and [OIII] line widths for SMGs, with the objects presented in this work highlighted. We include results from the near-IR spectroscopic program presented by S04 and include their classification into starburst (SB), AGN-dominated (AGN) and AGN+SB composites (Int). See §4.5.1 for details.

4.5.2 Star Formation Rates

Submm- and mm- selected galaxies are dusty systems and thus suffer from significant extinction. In the near-IR, the obscuration is not as high as in the optical, but still remains an important caveat to the observed line luminosities. Takata et al. (2006) show that the Hα-derived SFRs for these objects, with no correction for reddening are systematically lower than those derived from the total infrared luminosity $L_{8-1000\ \mu m}$ (Takata et al. 2006).

Takata et al. (2006) have shown that SMGs typically have observed Hα/Hβ $\sim$ 5$-$20, corresponding to extinction levels in the range $A_v \sim 1-4$ with a median $< A_v >= 2.9 \pm 0.5$, using the reddening curve from Calzetti et al. (2000).[3] Line emission from Hβ falls at 4861 Å, bluewards of $\lambda_{H\alpha} = 6563$ Å and it thus suffers more from dust obscuration than Hα. The intrinsic, unobscured ratio between these recombination Balmer lines is expected to be 2.86 (Osterbrock 1989). Therefore, comparison of the observed Hα/Hβ ratio with the intrinsic value, called the *Balmer decrement*, provides with an estimate of the extinction along the line of sight:

$$S_{H\alpha}(\tau_\lambda \sim \tau_{\rm Balmer}) = S_{H\alpha}(\tau_\lambda = 0) \times e^{-\tau_{\rm Balmer}} \tag{4.2}$$

$$\tau_{\rm Balmer} = \tau_\beta - \tau_\alpha = \ln[\frac{\rm H\alpha/H\beta}{2.86}]. \tag{4.3}$$

We apply a reddening correction of $e^{\tau_{Balmer}} \sim 4$ to the measured Hα luminosities assuming a *typical* Balmer decrement ~ 10 (see Table 4.4). This factor is significantly larger than the typical attenuation found for other high-redshift populations, such as the optically-selected LBGs, with attenuations of an average factor of 1.7 (Erb et al. 2006a). This demonstrates that an increased level of internal extinction is found in SMGs, with respect to other well-studied high-redshift populations.

We estimate SFRs in our targets from the reddening-corrected Hα line, assuming the following relation presented by Kennicutt (1998):

[3] Assuming the simplified case of a dust screen in the line of sight to the source, $E(B-V) = 0.935 \times [\ln(\rm H\alpha/H\beta) - \ln(2.86)]$ (Calzetti et al. 1994).

Table 4.4. Star Formation Rates, Metallicities and Dynamical Masses

SMM J	$L_{H\alpha}$[a] L$\odot$	$L_{8-1000\mu m}$[b] 10^{12} L$\odot$	$SFR_{H\alpha}$ $M_\odot$ s^{-1}	SFR_{IR} $M_\odot$ s^{-1}	M_{dyn} $M_\odot$	$12 + Log(O/H)$[c]
SMMJ030227.73	9.85×10^{10}	27.80	2978	4788	3.77×10^{12}	8.76
SMMJ123635.59	3.31×10^{10}	4.05	1001	697	9.68×10^{10}	–
SMMJ123549.44	–	4.45	–	766	2.35×10^{12}	8.76
SMMJ123716.01	5.58×10^{11}	5.25	–	904	–	–
MIPS142824.0	8.35×10^{10}	16.00	2526	2755	1.82×10^{12}	8.85

[a] Extinction-corrected using typical Balmer decrement found for SMGs by Takata et al. (2006). See §4.5.2 for details.

[b] We use total infrared luminosities from C05, corrected by approximately a factor of two, following Kovács et al. (2006)

[c] Derived from N2-index. See §4.5 for details.

$$SFR\,[\mathrm{M_\odot\,yr^{-1}}] = 7.9 \times 10^{-42} \times (L_{H\alpha}[\mathrm{erg\,s^{-1}}]). \tag{4.4}$$

With observed Hα luminosities (not corrected for extinction) in the range of $0.3 - 6 \times 10^{11}$ L$_\odot$, and assuming that the Hα line characteristics are due to star formation, the targets in our sample have SFRs $\sim 400 - 1200$ M$_\odot$ yr^{-1}. The SMG SMM J123716 has been previously identified as a QSO and thus the particularly wide Hα line (and consequently, very large Hα luminosity) is clearly a reflection of the ionization and kinematics within the AGN's broad line region.

We compare SFRs calculated from the existing Hα measurements and those derived from the total IR emission (Kennicutt 1998). For the latter we use $L_{8-1000\ \mu m}$ by C05, which are estimated from radio and submm-wave flux densities, corrected by approximately a factor of two, following Kovács et al. (2006). We find that even when corrected for extinction (as shown in Table 4.4), Hα-derived SFR estimates still remain a factor of $2 - 4$ less than those derived from the IR luminosity. These results are in reasonable agreement with the analysis of Takata et al. (2006). This suggests that additional extinction, unaccounted for by the Balmer decrement, may be present.

4.5.3 Stellar Dynamical Masses

From the widths of the rest-frame optical emission lines we can obtain estimates of dynamical masses for the galaxies in our sample. The relation between line-width and dynamical mass relies on the assumption that line-broadening is due to the motion of the gas in the general, large-scale gravitational potential well of the galaxy. For the sake of simplification, we approximate a galaxy to a sphere of uniformly distributed gas. For this case, the dynamical mass is given by:

$$M_{dyn} = 5 \times \sigma^2_{rest}(R/G), \tag{4.5}$$

where σ = FWHM/2.355 is the velocity dispersion of the gas, R is the radial size of the gas distribution and G is the gravitational constant. Hα narrow-band emission observations have shown that SMGs have a typical (seeing-corrected) radial size of 0.5–1$''$ or 4–8 kpc (Smail et al. 2004), while integral field spectroscopic observations have shown that the Hα distribution may extend out to $\sim 2''$ or 16 kpc (Swinbank et al. 2006). Assuming an Hα spatial extension of 1$''$, Hα line-widths in our study result in dynamical masses in the range of $M_{dyn} \sim 10^{11} - few \times 10^{12}$, with a median value of $< M_{dyn} >= 2.4 \pm 3.2 \times 10^{12}$ M$_\odot$ (see Table 4.4).

SMG masses are expected to be significant in order to retain a substantial amount of processed metal-rich gas in the interstellar medium, as observed in isolated cases (Tecza et al. 2004). However, we note that important caveats must be kept in mind in deriving stellar dynamical masses. Long-slit spectroscopy only provides us with an insight to the integrated emission of the galaxy. Therefore, it is very challenging to distinguish between the fraction of a broad Hα line due to ordered gas motions reflecting the dynamics of the entire galaxy and Hα emission arising from the broad line region of a central, albeit possibly weak, AGN. S04 have attempted to disentangle the broad and narrow-Hα components and have derived a median stellar dynamical mass $< M_{dyn} >\sim (1.5 \pm 0.9) \times 10^{11}$ M$_\odot$.

Greve et al. (2005) report median dynamical masses $< M_{dyn} >\sim 1.2\pm1.5\times10^{11}$ M$_\odot$ from detailed mapping of CO emission of 12 CO-detected SMGs. These observations

target higher CO transitions ($J \geq 2$) and thus trace mainly the dense, warm molecular gas in these galaxies definitely not associated with an AGN. It is thus possible that larger dynamical masses are traced by the colder, more extended molecular medium. Stellar masses of $\sim 10^{11}$ $M_\odot$ have been inferred from SED fitting of near-IR and optical aperture photometry (Borys et al. 2005). However, recent work by Maraston et al. (2006) suggests that popular stellar population models do not include a proper treatment of thermally pulsing asymptotic giant branch (TP-AGB) stars, which can result in significantly lower photometric mass estimates for high redshift galaxies, where TP-AGB stars are expected to contribute strongly to the galaxy SED.

The collection of these results indicates that reliable mass estimates for SMGs are still a work in progress. However, studies agree that SMGs are massive galaxies. The presence of such large masses already in place at these high redshifts, together with the large number density of these objects poses strong constraints in current theories of mass assembly. In order to reconcile these stellar masses and SFRs at $z \sim 2$ with the masses of local massive ellipticals, Baugh et al. (2005) have suggested that a top-heavy initial mass function may be at work in these galaxies. However, the appeal to a flat IMF and the validity of this assumption remains controversial. Both theoretical work and observational constraints remain necessary to develop a model of galaxy formation to reproduce the observed galaxy counts in the low- and high-redshift universe.

4.6 Conclusions

We present near-IR observations of five mm- and submm- detected galaxies in continuation of a large program to investigate the rest-frame optical emission of high-redshift ULIRGs. We derive dynamical masses and star-formation rates for these objects: $M_{dyn} \sim 10^{12}$ $M_\odot$ and $SFR \sim 1 - 3 \times 10^3$ $M_\odot$ yr^{-1}, assuming a typical extinction in the near-IR corresponding to a Balmer decrement Hα/H$\beta \sim 10$. These results provide further evidence supporting that mm- and submm-selected ULIRGs at high-redshift are highly massive systems undergoing intense star-forming activity.

We also find large velocity offsets between rest-frame UV and Hα lines for two of our objects, suggesting that strong outflows are present. With near- to super-solar metallicities, SMGs are likely rapidly enriching their environments.

Our observations also show clear AGN-like broad line signatures and/or high [NII]/Hα spectral diagnostic ratios in all five of our targets. We emphasize that when both star formation and an AGN are present, even though the high S/N of our low-resolution NIRSPEC observations is sufficient to detect clear AGN signatures, long-slit spectroscopic techniques face difficulties in disentangling their independent contributions and may result in overestimates of the SFRs and stellar masses of SMGs. This motivates greatly the pursuit of exploring the two-dimensional spatial distribution of line emission that recent integral field spectrographs provide. We have initiated such an effort with the OH-Suppressing Infrared Spectrograph (OSIRIS; Larkin et al. 2006) on Keck, as we discuss in Chapter 5.

Acknowledgements We thank the team of support astronomers, telescope operators and the staff members at the Keck Observatories for their assistance with the observations. In particular, we thank Jim Lyke, Grant Hill and Al Conrad for their excellent on-site support. We are also grateful to Dawn Erb for insightful discussions and her guidance in the reduction of NIRSPEC data. The data presented herein were obtained at the W.M. Keck Observatory, which is operated as a scientific partnership among the California Institute of Technology, the University of California and the National Aeronautics and Space Administration. The Observatory was made possible by the generous financial support of the W.M. Keck Foundation. The authors wish to recognize and acknowledge the very significant cultural role and reverence that the summit of Mauna Kea has always had within the indigenous Hawaiian community. We are most fortunate to have the opportunity to conduct observations from this mountain.

Chapter 5

OSIRIS IFU View of Submillimeter Galaxies: a 2-D Spectroscopic Insight to Starburst Galaxies in the High-Redshift Universe

We target Hα emission of three *submillimeter* galaxies (SMGs) at mean redshift, $< z > \sim 2.0$ with the OH-Suppressing Infrared Imaging Spectrograph (OSIRIS) in conjunction with the Keck Laser-Guide Star Adaptive Optics system. This spatially-resolved spectroscopic insight into the kpc-scale structure of these galaxies, reveals that the Hα emission in SMGs extends over scales $\sim 0.5'' - 2.0''$ or $4 - 17$ kpc. We distinguish spatially compact, broad-Hα line regions associated with an AGN and the extended regions of star formation traced by narrow-line Hα emission. This allows us to refine significantly estimates of stellar dynamical masses and star-formation rates (SFR) for the SMG population, which are critical for imposing constraints to current models of galaxy formation, but in the past inevitably hampered by both AGN contamination of emission lines and incomplete spatial sampling in long-slit spectroscopic studies. We also explore the dynamics of gas in the inner galaxy halo to improve our understanding of the internal dynamics of this enigmatic galaxy population. We find no evidence of ordered orbital motion, but rather large velocity offsets ($\sim \ few \ \times \ 100$ km s^{-1}) between distinct galactic-scale sub-components. Considering the disturbed morphology of SMGs, these sub-components are likely remnants of originally independent gas-rich galaxies that are in the process of merging, hence

triggering the ultraluminous SMG phase. Our Hα-based results are consistent with those derived from high-resolution CO observations, with $M_{dyn} \sim 4-20 \times 10^{10}$ $M_\odot$. We find that SMGs host SFR surface densities $\Sigma_{SFR} \sim 4-20$ $M_\odot$ yr^{-1} kpc^{-2}, a factor of $\sim 2-6$ higher than the median value for optically-selected high-redshift galaxies, but similar to local ULIRGs and circumnuclear starbursts.

5.1 Introduction

The details of stellar mass assembly are crucial for a full understanding of galaxy evolution. Most of the present-day stellar mass was already in place at $z \sim 1$, and the bulk of stellar build-up apparently took place at $1 \lesssim z \lesssim 2.5$ (e.g., Dickinson et al. 2003). Within this redshift range, galaxies grow rapidly to attain their final stellar masses. With inferred SFRs $\gtrsim 100-1000$ $M_\odot$ yr^{-1}, SMGs could build the stellar bulk of a massive galaxy in under a few hundred million years.

At $z \sim 2$, the large stellar masses associated with SMGs ($\sim 10^{11}$ $M_\odot$; Borys et al. 2005) represent important constraints in models of galaxy formation. Furthermore, they have led to the claim of a possible top-heavy IMF to reconcile SFRs at $z \sim 2$ with the masses of local massive ellipticals (Baugh et al. 2005). However, the SMG stellar mass estimates rely on fitting SED to near-IR and optical aperture photometric data (Borys et al. 2005) and recent work by Maraston et al. (2006) suggests that there is significant uncertainty associated with the assumed stellar ages and thus on photometric mass estimates derived for high redshift galaxies.

As discussed in Chapter 4, deep long-slit spectroscopic observations of Hα emission in SMGs with the Near-Infrared Spectrograph (NIRSPEC) on Keck have also provided further constraints to the dynamical masses inherent to this population: S04 find a median value of $\simeq (1.5 \pm 0.9) \times 10^{11}$ $M_\odot$ for a sample of 30 SMGs. Moreover, S04 report that broad Hα emission (FWHM$_{H\alpha} \gtrsim 1000$ km s^{-1}) is present in $\gtrsim 40\%$ of their SMG sample and that the composite spectrum of their sample is best represented by a narrow Hα line and an underlying broad Hα component with narrow-to-broad-line flux ratio of 0.6 ± 0.1 and with FWHM$_{rest} = 325 \pm 30$ and

1300 $\pm$ 210 km s^{-1}, respectively. The broad Hα line is due to the large velocities within the broad-line region close to a central AGN. Dynamical mass estimates based on the width of the Hα line thus retain the substantial caveat that broadening and brightening of the Hα emission due to the blended nuclear emission from an AGN may result in overestimates. When both AGN and star-forming activity are present, long-slit spectroscopic techniques face difficulties in disentangling their independent contributions, and may result in wrong estimates of the SFRs and dynamical masses of SMGs. The S/N of Hα NIRSPEC long-slit observations is sufficient to detect a clear AGN-like broad line signature, but is inadequate to reliably quantify the AGN contribution (S04). Therefore, SFRs and dynamical masses of SMGs may both be overestimated. Furthermore, dynamical information has also proved difficult to extract from NIRSPEC data (S04), even for the less extreme and likely more ordered cases of optically-selected LBGs at similar redshifts (Erb et al. 2003).

Integral field spectroscopy opens the possibility of investigating the properties of nebular emission at different scales within a galaxy. A two-dimensional (2D) spatial spectroscopic insight to the line emission is the only viable probe of the distribution and dynamics of the gas in the inner galaxy, on $1 - 10$ kpc scales. The 2D velocity fields can cast new light on the nature of these galaxies, whether consisting of gas forming stars in a disk or a merger between galaxies.

Results from the SPectrometer for Infrared Faint Field Imaging (SPIFFI) on the ESO Very Large Telescope (VLT) first showed how 2D spectroscopy could reveal structure in line emission across a dusty galaxy at $z \simeq 2.5$ (Tecza et al. 2004). Their marginally resolved (non-AO) spectra reveal substructure in nebular and continuum emission. Using the relatively modest $0.2''$ resolutions $R \simeq 1000, 1700$ of the integral-field unit (IFU) at UKIRT (UIST) and the Gemini Near-IR Spectrograph (GNIRS) IFU at Gemini-South, respectively, Swinbank et al. (2006) (hereafter, S06) investigated the 2D spectra of six SMGs at $z = 1.3 - 2.5$. They detected kpc-scale Hα sub-structure, including multiple components and extended emission. The OH-Suppressing Infrared Imaging Spectrograph (OSIRIS; Larkin et al. 2006) on Keck II benefits from superior spectral resolution ($R \simeq 3000 - 3800$) and a larger tele-

Table 5.1. Summary of *OSIRIS* Observations

Name	RA[a] ($h\,m\,s$)	Dec. ($^\circ\,'\,''$)	$z_{optical}$	Filter	Plate Scale mas	Exposure times ks	Date
SMM J030227.73[b]	03:02:27.73	+00:06:53.5	1.4076;[d]	$Hn2$	100	12.6	Oct. 2005
SMM J123549.44[e]	12:35:49.44	+62:15:36.8	2.2032[c]	$Kn2$	50	10.8	May 2007
SMM J163650.43[f]	16:36:50.43	+40:57:34.5	2.3850[c]	$Kn3$	50	12.6	May 2007

[a] Radio center from C05

[b] Tip-tilt star 03:02:25.19 +00:06:43.80, with R-mag= 17.8 and 39.3″ separation.

[c] From S04

[d] From S06

[e] Tip-tilt star 12:35:43.33 +62:14:56.69, with R-mag= 15.0 and 58.6″ separation.

[f] Tip-tilt star 16:36:50.61 +40:56:50.92, with R-mag= 13.7 and 43.6″ separation.

scope (10-m). Moreover, OSIRIS is designed to be used with the Keck Laser-Guide Star Adaptive Optics (LGS-AO; Wizinowich et al. 2006; van Dam et al. 2006) system, which allows for atmospheric distortion corrections to be derived from parallel observing of a nearby bright star and applied to the science targets. Adaptive Optics thus enables diffraction-limited resolution to be reached with ground-based observations to probe for kpc-scale structures in galaxies at $z \sim 2$.

In this chapter we present the results of an OSIRIS program that we have undertaken to study the 2D distribution of Hα emission of three SMGs from the radio-identified sample of C05. We discuss our sample selection and observing strategy in §5.2. The steps comprising the reduction and analysis of the science spectra are discussed in §5.3. Our results are presented in §5.4 and discussed in §5.5.

5.2 Observations

We obtained our observations from October 2005, during the shared-risk science period of the OSIRIS instrument, to March 2008. Observing conditions varied from photometrically optimal, with $\sim$ 0.4″ seeing in the V-band, to moderate, with a seeing $\sim 1''$.

The integral field capability of OSIRIS is based on an array of 3000 lenslets, each

of which produces a spectrum of a different location of the observed target. In this way, OSIRIS spectroscopically *dissects* the 2D-image of a galaxy. To optimize the detection of our targets, we selected SMGs with bright Hα lines, detected in previous long-slit spectra (S04; Takata et al. 2006). LGS-AO allows for corrections to be derived for targets with a $tip-tilt$ star that can be as faint as $R \sim 18$ within $1'$ of the science target. Taking all these considerations into account, we selected our science targets carefully to optimize OSIRIS performance.

5.2.1 Sample Selection

We selected our SMG targets from the sample of SMGs in C05. We took advantage of existing near-IR long-slit Hα spectroscopy (S04, Takata et al. 2006) to select those SMGs with the brightest Hα lines, $S_{H\alpha} \gtrsim 10^{-15}$ erg s^{-1} cm^{-2} to optimize detection. For the tip-tilt star selection we used the Keck Adaptive Optics Guide Star online tool [1] and corroborated the quality of the tip-tilt star candidates (stellar nature and magnitude) using the Sloan Digital Sky Survey Catalog Archive Server (Adelman-McCarthy et al. 2008).

We also selected SMGs with Hα emission lines that did not fall on bright near-IR OH sky emission lines. The resulting sample of SMG targets, complying with these requirements are listed in Table 5.1.

5.2.2 Instrument Configuration and Observing Strategy

The targets in our sample have redshifts from $z \simeq 1.4$ to $z \simeq 2.4$, which places their observed Hα emission in the $H-$ and $K-$band.[2] In the interest of obtaining the largest field of view available at the observed Hα wavelengths, we used the narrow-band filters indicated in Table 5.1.

Our observations include a combination of the 100-mas and the 50-mas plate-

[1] http://www2.keck.hawaii.edu/software/findChartGW/acqTool.php

[2] AO corrections in the $J-$band are not optimal. The *strehl* value for a given wavelength gives a measure of the quality of the LGS-AO corrections and is given by: $S = e^{-(2\pi\sigma/\lambda)^2}$; therefore, as λ decreases, so does the AO correction.

scales, which provide the largest fields of view (FOV): $\sim\ 4.8'' \times 6.4''$ and $\sim\ 2.4'' \times 3.2''$, respectively. The 100-mas lenslet plate-scale has the advantage of allowing us to maximize the area of photon collection, crucial for the study of faint objects. However, the background thermal noise for this coarsest plate-scale had been significantly underestimated (Law et al. 2006); instrument servicing on February 2006 included a decreased pupil size for the $0.05''$, $0.035''$ and $0.02''$ plate-scales, leading to a significant decrease in thermal background. Thereafter, we used the $50-$lenslet scale to benefit from the reduced instrument background to improve our science detections at the cost of a reduced FOV.

Our observing strategy consists of an initial pair of spectroscopic frames offset from one another by $0.5''$ on the tip-tilt star. These short-exposure frames ($\sim 1 - 10$ s) were used as a coordinate centering reference. Having calculated precise offsets to the science target from deep $K-$band images (e.g., Smail et al. 2004), we do a blind-offset to the science target. These consist on sets of standard ABBA sequences separated by tiny offsets ($\pm 0.5''$) followed by a sky-integration frame, offset by $\sim \pm 15''$ from the science target. Each ABBA sequence comprises four $15-$minute frames taken at two positions separated by $0.5''$ to allow for on-object dithering. Our strategy required a large number of dark frames, taken during the afternoon prior to and in the morning after the observing night. These darks have the same exposure times as the science exposures.

5.3 Reduction and Analysis

We use the OSIRIS Data Reduction System (DRS) pipeline [3] to do the basic reduction of all science and calibration data. The pipeline consists of an IDL-based program comprising a collection of individual modules, each of which performs a specific task and which we can optionally include or exclude at different pipeline *passes*. OSIRIS raw files are multi-extension fits files, with the image data contained in the 0^{th} extension, the standard deviation of sampling in the 1^{st} and the data quality (bad pixel

[3] http://www.astro.ucla.edu/∼irlab/osiris/pipeline.html

mask) on the 2^{nd}. Key information, including telescope pointing information for each exposure, is included in the data headers. The major reduction steps of the pipeline are: subtraction of a dedicated sky frame from each science exposure, transformation of a *raw* 2D file into a three-dimensional (3D) data cube and the mosaicing of all science frames into one single data cube. The resulting 3D data cube has two spatial axes (x, y) and a third axis for wavelength (λ), calibrated according to the corresponding rectification matrix available for the particular instrument setup (filter and lenslet plate-scale). We refer the reader to the OSIRIS Manual [4] for a detailed description of the pipeline.

The science targets in our program are faint and potentially significantly extincted sources. Their analysis thus requires a series of reduction steps in addition to the standard pipeline processing to minimize the otherwise persistent sky background. In particular, we perform additional corrections to remove instrument artifacts (a simulated flat-fielding) and sky subtraction. These additional reduction steps are tuned carefully to each object.

The OSIRIS pipeline assumes that any signal in the image corresponds to photons from the science target. Any charge accumulation on the detector or any other spurious signal of different nature will therefore be interpreted as part of the science detection. To get rid of these artifacts we simulate a flat-fielding of the science data cubes. For this, we pipeline-process the individual dedicated sky exposures by subtracting a *master*-dark image from each sky frame, where the *master*-dark image results from median-combining the collected dark frames. For the standard sky-subtraction step within the OSIRIS pipeline, we use the processed sky cube taken within the shortest time from the science exposure (the *nearest* sky frame).

In addition to this standard sky subtraction, we perform two additional steps of sky subtraction. In the case of faint targets, such as the ones in our sample, residual background from the OH lines after sky subtraction can be significantly detrimental to our analysis. We first create a *supersky* 2D image, by median-combining the pipeline-reduced sky cubes (without making any offsets with respect to the telescope

[4] http://www.astro.ucla.edu/∼irlab/osiris/downloads/

pointing information in the individual sky frame headers) and wavelength-collapsing the combined cube along the λ-range around where the emission line is expected, $\lambda \simeq \lambda_{H\alpha} \pm 600\,\text{Å}$. We then divide each wavelength slice in the science data cube by this *supersky* image, simulating a flat-fielding of the science image. The second step of additional sky subtraction consists of calculating the median flux for all spatial pixels in each λ-frame in the science data cube and subtracting this value from each (wavelength-slice) frame in the science cube. In this way we set the persistent background to zero, eliminating the residual background plateau within the science cube.

Finally, we mosaic the different science frames using the mean-clip averaging algorithm included in the OSIRIS pipeline. For this, we rely on the *RA* and *DEC* header keywords, which remain accurate telescope pointing coordinates throughout observations with uninterrupted LGS acquisition.

In the cases where OH-line background still persisted at a significant level within the mosaiced cube, we also made use of the sky-subtraction routine developed by Davies (2007). This routine is specifically tailored to remove under- and over-subtracted OH-emission from near-IR integral-field spectra, taking into account the temporal variations in absolute fluxes of OH-lines as well as their individual fluxes relative to each other. Although only a modest increase in S/N resulted for the observations presented here ($\lesssim 1.5$), we adopt this routine.

5.3.1 Hα Maps

The major appeal of integral field spectroscopy is that it allows for a 2D spatial insight to the spectral properties of an object. We take advantage of this new view and construct a number of maps to help us understand the distribution of Hα properties across the SMGs in our sample. These include Hα narrow-band (NB) images, and velocity and line-width maps.

With sky-subtracted, flat-fielded, mosaiced science data cubes in hand, we produce NB images collapsed over a range $\Delta v \simeq 1000 - 2000$ km s^{-1} centered at the redshifted

Hα line for each of our targets, assuming redshifts from prior long-slit near-IR spectroscopy (S04), verified against OSIRIS observations. We use these Hα narrow-band images to map the overall distribution of the line emission and to measure the spatial extent of nebular emission throughout the galaxy. In this way, we distinguish between compact and more diffuse regions of emission. The former are likely associated with AGN or compact starburst, while the latter indicate extended star formation. We convert integrated Hα line fluxes at each pixel into a SFR, following Kennicutt (1998):

$$SFR\ [\mathrm{M_\odot\,yr^{-1}}] = 7.9 \times 10^{-42} \times (L_{H\alpha}\ [\mathrm{erg\,s^{-1}}]) \tag{5.1}$$

The distribution of SFRs across the object is used to build star-formation rate surface density ($\Sigma_{\rm SFR}$) maps, considering the pixel scale of the observations. These maps allow us to compare our $\Sigma_{\rm SFR}$-values to those found in local star-forming galaxies (Kennicutt 1998) and other high-redshift populations (e.g., LBGs; Erb et al. 2006a). We caution that the AGN contribution to the Hα emission is included in these maps, which we exclude from the SFR quantitative analysis in §5.5.2.

We extract velocity maps for each science cube by fitting gaussian line profiles in the dispersion direction at each pixel location. To improve the *S/N* in these velocity maps, we first convolve the data along the spatial direction with a 2D gaussian function with FWHM = 2.0 pixels. These velocity maps allow us to probe for velocity offsets between distinct components in each system. We use the gaussian fits at each pixel to re-construct the science detection in terms of *S/N* maps and to map the distribution of line widths, in terms of the velocity dispersion $\sigma_{rest} = \mathrm{FWHM}_{rest}/2.355$. The latter allows us to probe for the presence of AGNs, as revealed by large linewidths, with $\mathrm{FWHM}_{rest} \gtrsim 1000$ km s^{-1}.

We take advantage of our NIRSPEC long-slit observations (see Chapter 4; S04) to provide an *approximate* flux calibration to the Hα line in our data cubes. For this, we collapse each data cube along the dispersion direction within a $\Delta\lambda \sim \mathrm{FWHM}_{H\alpha}$ and use our integrated NIRSPEC line flux as a reference. With calibrated flux information,

we are in a position to derive SFR distributions for our objects.

5.4 Results

In this section we present our results for each individual target. We show Hα maps for each of our targets in Figs. 5.1-5.6. We rotated each of these images from the instrument position angle (PA) such that North is up and East points towards the left.

5.4.1 SMM J030227.73

SMM J030227.73 was first detected by Webb et al. (2003b) as part of the Canada-UK Deep Submillimeter Survey (CUDSS). Optical and near-IR spectra by C05 and S04 place this galaxy at $z \simeq 1.4076$. A high [NII]/Hα ratio ([NII]/Hα $=$ 1.38$\pm$ 0.07; S04) and a broad Hα (FWHM$_{H\alpha}$ $=$ 1500 $\pm$ 266 km s^{-1}; see Chapter 4) suggests that this SMG has significant AGN activity. These conclusions were confirmed by S06 with the Gemini-GNIRS integral field unit. Furthermore, *Spitzer* mid-IR spectroscopic follow-up of this object shows a substantial excess in mid-IR continuum, suggesting a significant AGN contribution (see Table 3.4; Menéndez-Delmestre et al. 2008).

We create a NB Hα image by collapsing the reduced data cube along the wavelength range $\simeq$ 1.57 $-$ 1.59 μm, centered around the redshifted Hα line corresponding to $z = 1.4076$. The resulting Hα emission map is shown in Fig. 5.1. On the bottom-left panel of Fig. 5.1 we overlay Hα contours on the *HST-ACS/NICMOS* true color image of SMM J030227.73, representing the *BVI*-band continuum of this galaxy. From the *HST* image we see that the continuum emission is dominated by a bright, compact source, which coincides with the compact ($\simeq 0.7''$) peak of Hα emission detected with OSIRIS. S06 detect compact Hα emission coinciding with what appears in the *HST* image as a secondary compact knot, 1.3$''$ away from the central source (just off our OSIRIS FOV). They tentatively identify this second clump as an AGN, according to a high [NII]/Hα ratio.

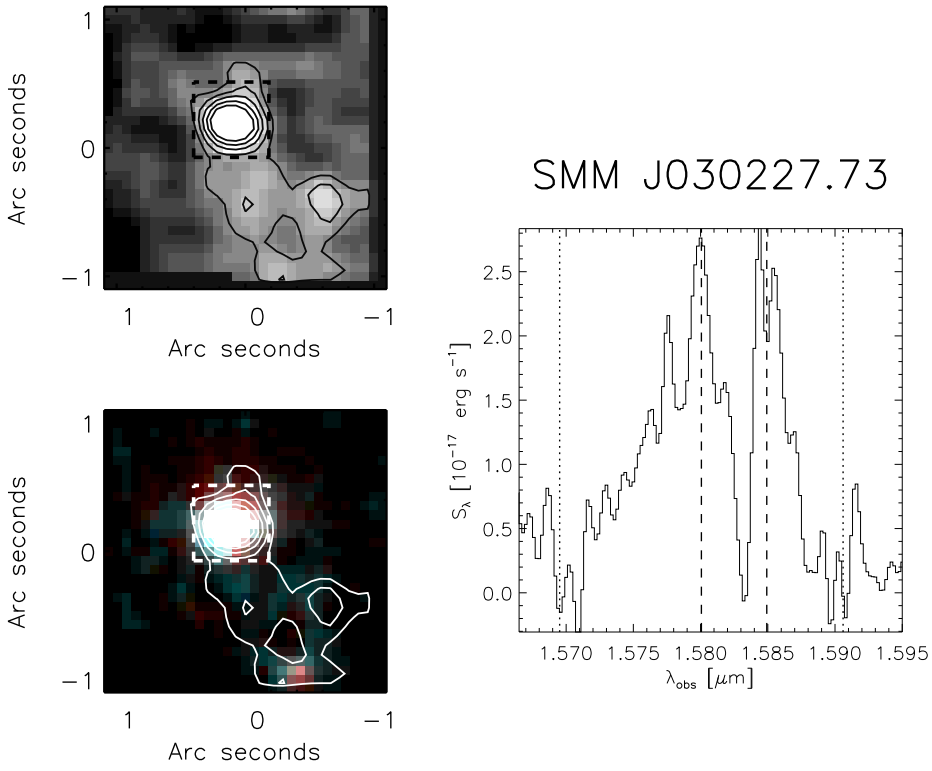

Figure 5.1 OSIRIS Hα detection in SMM J030227.73. (**Top Left:**) OSIRIS Hα emission integrated across the line with surface brightness contours overlaid (inner and outer contour $\sim 50, 10\sigma$). (**Bottom Left:**) The same σ-contours overlaid on a multicolor *HST*-NICMOS image of the galaxy. Note that there is substantial offset between the HST emission and the OSIRIS Hα emission. (**Right:**) Flux-calibrated 1D spectrum of Hα emission within the region indicated by the dashed box in the left panels. The redshifted wavelengths for Hα and [NII]$_{6583}$ are indicated by the dashed lines. The dotted vertical lines denote the wavelength range over which we collapsed the OSIRIS cube to obtain the narrow-band Hα-[NII] image shown in the bottom left panel. We see that the central compact source displays a bright, broad Hα ($S_{H\alpha} = 1.023 \pm 0.06 \times 10^{-15}$ erg s^{-1} cm^{-2} Å^{-1}, FWHM$_{rest} = 1070 \pm 76$ km s^{-1}, with significant emission from the [NII] line ([NII]/H$\alpha = 0.53 \pm 0.1$).

With the aid of LGS-AO, OSIRIS allows us to resolve the region between these two compact components, in contrast to the S06 results, which distinguish no diffuse Hα emission. To the South-East of the central bright source in Fig. 5.1, OSIRIS intensity contours highlight a region of diffuse Hα emission that extends out to $\gtrsim 1''$.

In Fig. 5.2 we show the Hα *S/N*, line-width and velocity maps for SMM J030227.73. The bright, compact knot from the central source stands out at a $S/N > 30$ while the faint and diffuse emission appears at a lower, but still significant $S/N \sim 10 - 15$. We extract a 1D spectrum of the compact, bright region which reveals broad Hα emission (FWHM$_{rest}$ = 1070 ± 76 km s^{-1}), accompanied by a strong emission from the forbidden transition [NII]$_{6583}$ (see Fig. 5.1). From the spatial distribution of Hα line-widths in Fig. 5.2, we see the difference in Hα line characteristics between the compact and diffuse emitting regions, where the latter displays a much narrower component (FWHM$_{rest}$ = 110 ± 15 km s^{-1}). This suggests that the bright central source corresponds to an AGN (in agreement with S06), while the diffuse emission appears to be associated with spatially extended star formation. Since our OSIRIS observations do not cover the full extent of this secondary knot of emission we cannot test the possibility of two AGNs within this system.

The velocity map in Fig. 5.2 (bottom panel), measured relative to the rest-frame UV redshift identified by C05, suggests that the diffuse Hα component is offset from the compact component by $\simeq 150 \pm 50$ km s^{-1}.

5.4.2 SMM J123549.44

Long-slit near-IR observations of this source (S04) and ultra-deep *Chandra* images (Alexander et al. 2005a) have revealed clear AGN signatures. Furthermore, recent mid-IR observations have revealed an excess of hot continuum emission, in agreement with the hypothesis of a significant contribution from AGN activity to the bolometric luminosity (Menéndez-Delmestre et al. 2008). Tacconi et al. (2006, 2008) have also undertaken high-resolution CO observations of this galaxy. They found CO emission dominated by a compact source ($\lesssim 0.5''$) with a prominent double-peaked CO profile,

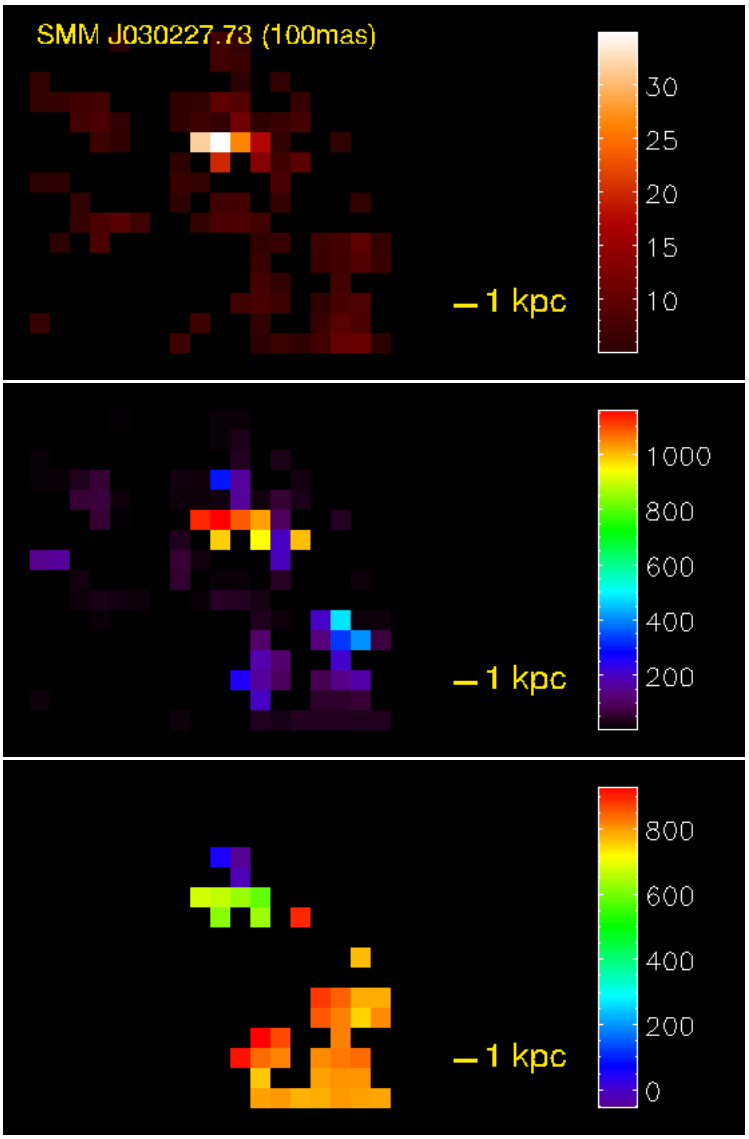

Figure 5.2 Distribution of Hα emission in SMM J030227.73. For all images, North is up and East is left. (**Top:**) S/N map displaying a bright compact source and additional lower-level extended emission. (**Middle:**) Hα line-width (σ_{rest}) map in units of km s^{-1}, showing that the central component has a rather broad (FWHM$_{H\alpha}$ $\simeq$ 1000 km s^{-1}) relative to the extended emission, with FWHM$_{H\alpha}$ $\lesssim$ 200 km s^{-1}. This distribution of line-widths suggests that the bright compact Hα emission in the center is associated with the broad-line region of a central AGN. Extended emission appears to be narrower and thus associated with star formation. (**Bottom:**) Hα velocity map, suggesting relative offsets $V_{rel} \simeq 200$ km s^{-1}. See §5.4.1 for details.

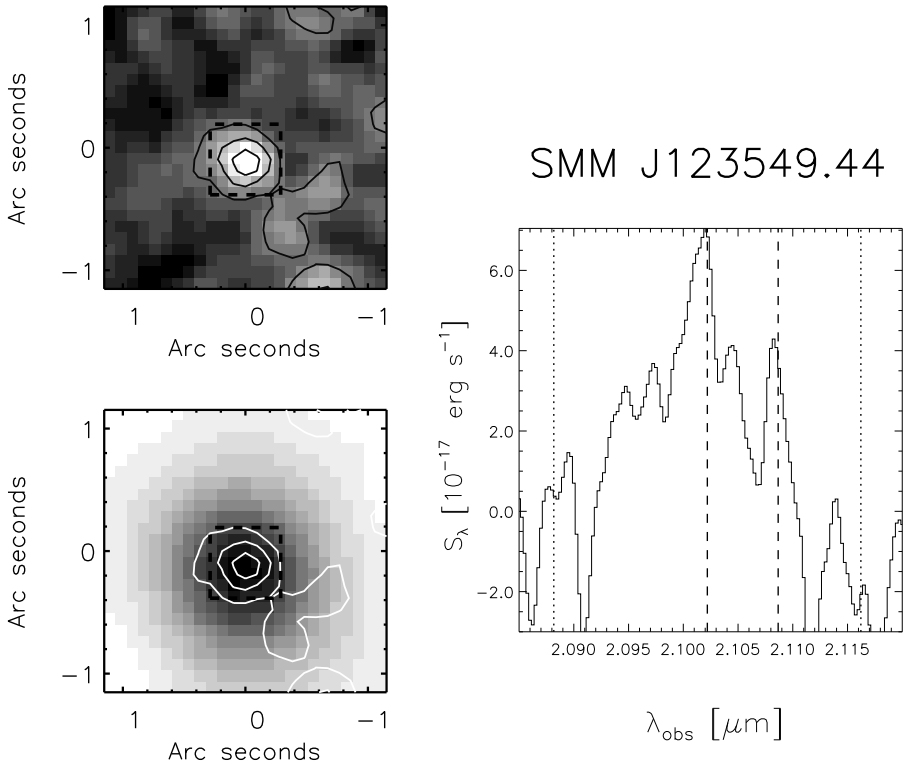

Figure 5.3 Hα emission as detected by OSIRIS in SMM J123549.44, following the same format as Fig. 5.1. The bottom left panel displays the Hα OSIRIS contours (the outermost representing the 5σ contours) overlaid on a *NICMOS* $I-$band image. We see that the Hα within the central $\sim 1''$ is dominated by a bright, compact source. Displaying a broad Hα line (FWHM$_{rest}$ $\gtrsim$ 1000 km s^{-1}), we take this emission knot to be associated with AGN activity.

which they associate with the orbital motions of gas within a disk close to the central AGN.

Optical and near-IR (long-slit) spectroscopy set this object at $z = 2.2032$ (C05, S04). The redshifted Hα line is thus expected at $\lambda = 2.1023$. We collapse the OSIRIS cube along the dispersion direction within Δv $\simeq$ 2000 km s^{-1} and obtain the narrow-band Hα image presented in Fig. 5.3. The Hα emission for SMM J123549.44 is dominated by a compact ($\sim 0.7''$) source, though faint traces of diffuse emission extend out to $1''$ to the South-West of the central region (see also S/N map in Fig. 5.4). From long-slit observations, S04 report a relatively narrow Hα emission of FWHM$_{rest}$ $\simeq$ 536 km s^{-1} SMM J123549.44. However, we find that the integral

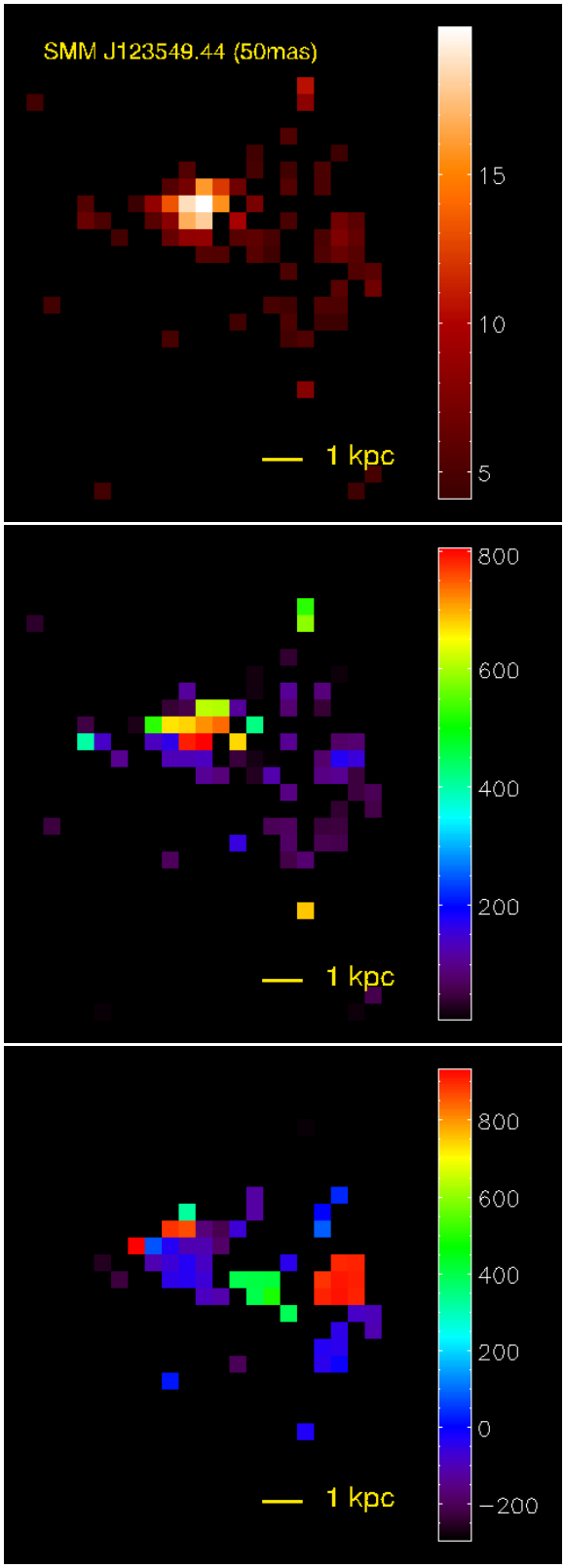

Figure 5.4 Distribution of Hα emission in SMM J123549.44, following the same format as Fig. 5.2. We see that the Hα emission is dominated by a compact source with broad Hα emission (FWHM$_{rest}$ = 1400 km s^{-1} or $\sigma \simeq 600$ km s^{-1}). At a fainter $S/N \simeq 5$, diffuse emission can be seen with narrower Hα line emission ($\sigma \lesssim 200$ km s^{-1}).

OSIRIS view of this object allows us to distinguish a rather broad Hα line from the central region indicated by the dashed box in Fig. 5.3, with FWHM$_{rest}$ $\simeq$ 1390 $\pm$ 50 km s^{-1} (or σ $\simeq$ 600 km s^{-1} in the middle panel of Fig. 5.4). The map of relative velocities (using z = 2.2032 as a reference; S04) suggests that there might be velocity offsets of up to 900 km s^{-1} within the diffuse region. Such large velocity offsets within this system may be attributed to the relative motion of multiple galactic-scale companions, potentially undergoing a merger. However, the low S/N of this trace remains an important caveat.

5.4.3 SMM J163650.43

This galaxy was first identified in the submm by Scott et al. (2002) and its broad-band near-IR emission has been studied in detail by Smail et al. (2003). With a bolometric luminosity L$_{bol}$ = (3 $\pm$ 2) $\times$ 10^{13} L$_{\odot}$, this galaxy is unusually luminous even as an SMG (Chapman et al. 2003). Optical and near-IR spectroscopy revealed a redshift of $z \simeq 2.38$ and unveiled broad Hα emission (S04) and a high [OIII]/Hβ ratio, signatures characteristic of a Seyfert AGN (Smail et al. 2003). This galaxy has been resolved into different components, with its spatial extension and complex structure (Smail et al. 2003; S06).

With OSIRIS LGS-AO, we zoom into the inner regions of this galaxy. In Fig. 5.5 we show the OSIRIS data cube collapsed along the dispersion direction within a range Δv $\simeq$ 2000 km s^{-1} and centered at λ $\simeq$ 2.22 μm, where redshifted Hα is expected for this source. We find diffuse Hα emission extending over $\simeq$ $(1'')^2$, in the shape of an arc. We overlay the OSIRIS intensity contours atop a true-color BVI-band *HST*-image to find that the Hα emission extends throughout the continuum light. We extract the 1D spectrum of a region enclosing the full extent of the Hα emission (box 2) and measure an intermediately broad Hα line with FWHM$_{rest}$ = 710 $\pm$ 50 km s^{-1}. A closer look at the distinct regions within this galaxy reveals that the ensemble emission is the result of a combination between a broad Hα region (box 1) and regions with narrow Hα emission (box 0), with FWHM$_{rest}$ = 2400 and 475 km s^{-1}, respectively.

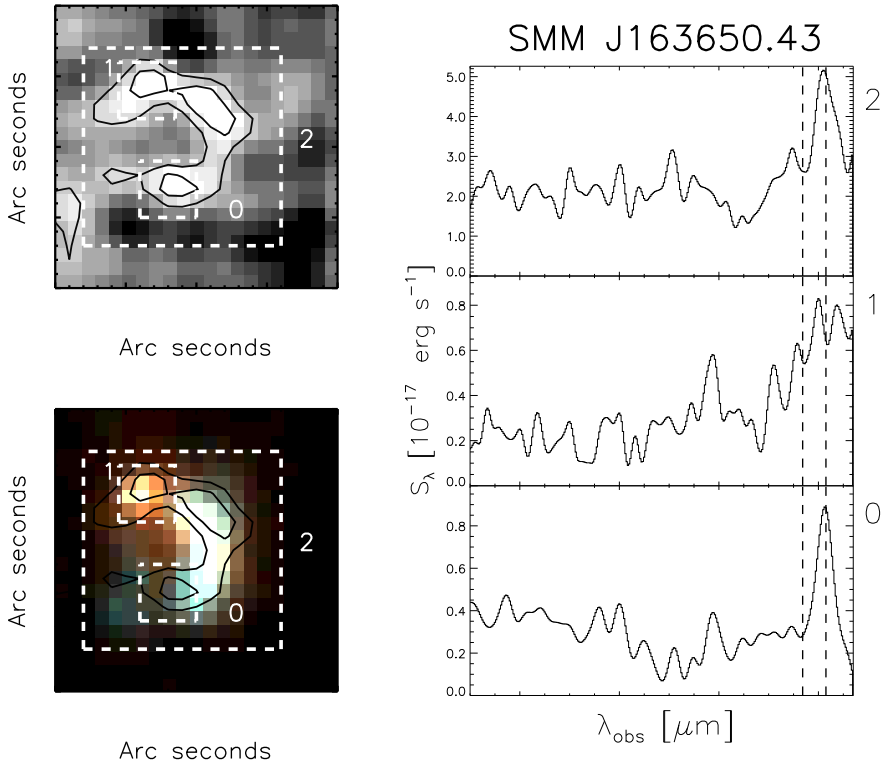

Figure 5.5 Hα emission as detected by OSIRIS in SMM J163650.43, following the same format as Fig. 5.1, with surface brightness contours in 2σ steps with the outermost contour corresponding to 8σ, overlaid on a multicolor *HST*-NICMOS image of the galaxy. The Hα intensity contours extend along the entire continuum-bright region in the *HST* image. We see that there is diffuse emission extending in the shape of an arc, within which Hα line characteristics differ: the north-east red clump in the *HST* image (box 1) displays a broad Hα line, while other regions of the diffuse emission display a narrow Hα line (box 0). See §5.4.3 for details.

The broad Hα emission coincides with the red knot visible in the underlying *HST* image, while the narrow Hα regions are associated with the diffuse emission to the south.

In Fig. 5.6 we show the S/N of the gaussian fits to the Hα line at each spatial pixel within the source. The southern and eastern extension of the arc-shaped region in the collapsed OSIRIS cube in Fig. 5.5 have modest S/N ($\sim 5-8$). This physically extended region corresponds to narrow Hα detection, as can be seen by the values of velocity dispersion $\sigma \simeq 200$ km s^{-1} (FWHM$_{rest} = 475$ km s^{-1}; see Table 5.2) in the middle-panel of Fig. 5.6. On the other hand, the northern compact region with broad Hα emission (FWHM$_{rest} = 2400$ km s^{-1}) suffers from low S/N (< 3). This reflects the greater ease of detecting a narrow emission line that emerges sharply from the continuum emission as compared with a broad emission feature (see Fig. 5.5). We do not find any velocity offset between the different components in this galaxy, as given by the centroids of the gaussian fits to the Hα line emission.

Prior long-slit spectroscopic work by S04 attempted to disentangle the broad and narrow Hα components. They distinguished narrow Hα component with an underlying broad component (FWHM$_{rest} \simeq 306 \pm 47$ and 1753 ± 238 km s^{-1}, respectively). We emphasize that the long-slit spectroscopic view provides insight solely to the integrated emission from the region enclosed within the slit. Contributions to the Hα emission arising from the AGN are mixed with extended emission arising from star-forming regions. Therefore, it is very challenging to separate reliably these two contributions. With OSIRIS we are able to separate reliably spectra of spatially distinct regions within a galaxy. This separation between spatial and spectral information allows us to derive reliable dynamical masses and SFRs, uncontaminated by the broad-line region of an AGN. We discuss this in §5.5.1 and §5.5.2.

5.5 Discussion

Recent near-IR integral field spectroscopic observations by S06 have shown that most SMGs often have multiple components that can be spatially distinguished within the

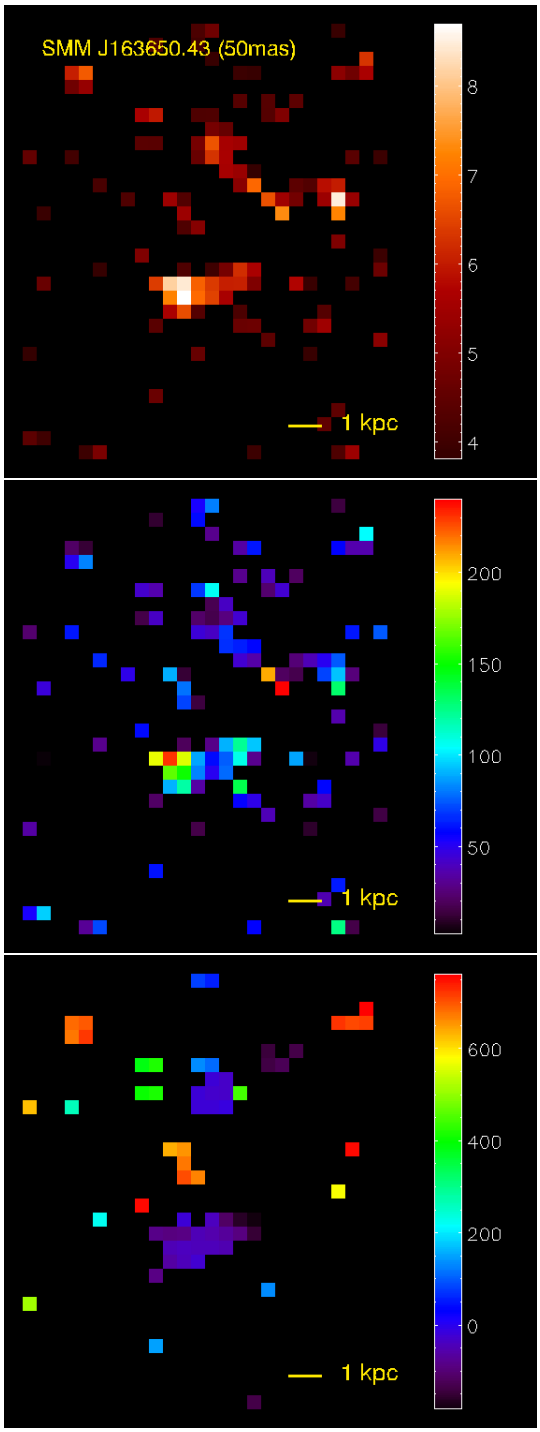

Figure 5.6 Distribution of Hα emission in SMM J163650.43, following the format of Fig. 5.2. We note that the S/N-map shows very weak detection of the region corresponding to the broad Hα region. It is more difficult to detect a broad, shallow line atop a continuum than it is to detect a narrow line. These maps show precisely this: the northern clump with broad Hα (see Fig. 5.5) does not appear in these maps, while the southern region, with narrower Hα ($\sigma \simeq 200$ km s^{-1}) stands out clearly.

central ~ 8 kpc. With OSIRIS we have been able to peer into these central regions, allowing us to zoom further in than these previous integral field observations without LGS-AO corrections.

From the global dynamics revealed by the integral view of our SMG targets, we find no indication that gas kinematics are associated with ordered motions, as would be present in a gaseous disk. This is in contrast to relatively recent reports on high-redshift LBGs (Förster Schreiber et al. 2006; Law et al. 2007), where continuous, gradual velocity gradients have been identified in individual cases as evidence for ordered rotation. SMGs do not appear to host such ordered kinematics: we find velocity offsets between distinct components, but no continuous velocity structure across SMGs. These results strengthen the conclusion derived from deep rest-frame optical *HST*-imaging that SMGs are disturbed systems, likely corresponding to a merger (Smail et al. 1998, 2004). Within this context the distinct components that comprise the SMGs could potentially be associated with the remnants of the pre-merger galaxies.

We have been able to spatially distinguish regions with broad Hα emission that are dominated by AGN activity and those with narrow Hα emission where star formation is taking place. Diffuse, narrow Hα emission – where star-formation activity dominates – extends over $\sim 0.7 - 2''$ (see Table 5.2). At the redshifts covered by our targets, these angular sizes correspond to $8 - 17$ kpc. These sizes compare reasonably well to those presented by S06 and Tecza et al. (2004), who report resolved nebular emission on scales from $4 - 11$ kpc for a total of seven SMGs. With these sizes in hand, we are in a position to derive reliable SFRs – keeping Hα flux calibration caveats in mind – and clean estimates of dynamical masses as traced by the Hα emission from the ionized gas distribution in regions with no AGN contribution (see §5.5.1).

5.5.1 Dynamical Masses

The kinematics of the gas, as given by the velocity dispersion (σ) of rest-frame optical lines, can be used to estimate dynamical masses. This relies on the assumption

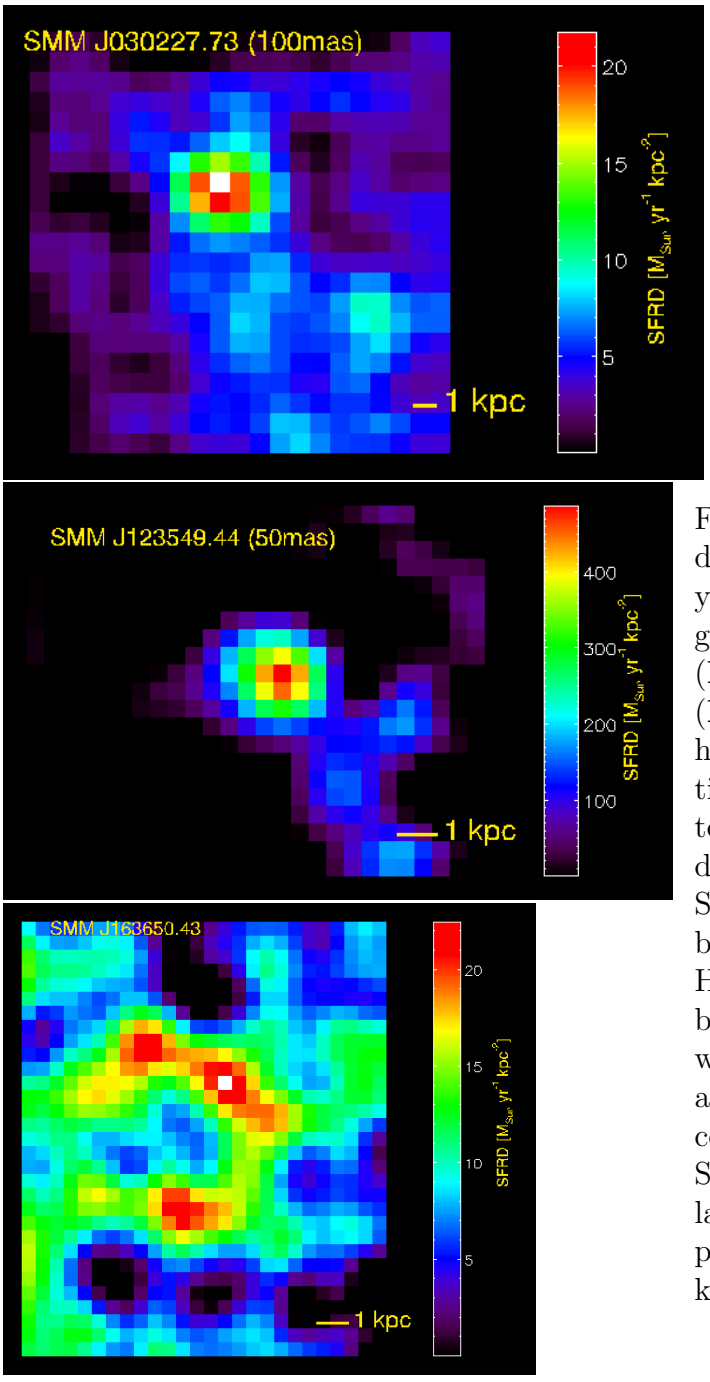

Figure 5.7 Map of SFR surface densities ($\Sigma_{\rm SFR}$) in units of $M_\odot$ yr^{-1} kpc^{-2} for our three SMG targets: (**Top:**) SMM J030227.73, (**Middle:**) SMM J123549.44 and (**Bottom:**) SMM J163650.43. We have estimated a typical extinction correction and applied it to these maps (see §5.5.2 for details). SMM J030227.73 and SMM J123549.44 are dominated by a compact region of broad Hα associated with an AGN. In both cases, diffuse emission towards the south-western direction appears to be composed of several compact knots, $\sim$ 1 kpc in size. SMM J163650.43 displays a very large spatial extension, also comprised of compact knots of $\sim 1-2$ kpc in size.

that line broadening is due to the internal dynamics of the gas within the galaxy's central potential well. However, in the presence of an AGN – and depending on the geometrical orientation of the object – the large velocities intrinsic to the gas within the AGN's broad-line region may enhance the width of rest-frame optical lines by confusion. The resulting mixing of gas kinematics contained by rest-frame optical lines makes it quite challenging to disentangle the AGN and the stellar contributions through long-slit spectroscopy, and can lead to significant overestimates in dynamical masses and SFRs. Since a number of AGN signatures have been revealed in X-ray, optical and mid-IR observations of individual SMGs (e.g., Alexander et al. 2005a, C05, Menéndez-Delmestre et al. 2008), this is a critical consideration to take into account.

With OSIRIS we can rely on the line-width of the Hα emission of regions uncontaminated by an AGN to derive reliable dynamical masses. For this, we use Equation 4.5, where σ is the velocity dispersion of the gas and R is the radial size of the gas distribution. We use velocity dispersions of the regions displaying no AGN signatures (referred to as *diffuse* emission regions in Table 5.2) and consider the full spatial extension of the Hα emission in determining the radial size of the gas distribution. In this manner, we estimate a dynamical mass for each galaxy as a whole assuming that the gas dynamics are reflected by the line-width of the narrow Hα line observed in the regions uncontaminated by the broad-line region of an AGN. We find dynamical masses $M_{dyn} = (4.3 \pm 0.6) \times 10^{10}$ M$_\odot$ and $M_{dyn} = (2.0 \pm 0.5) \times 10^{11}$ M$_\odot$ for SMM J030227.73 and SMM J163650.43, respectively. In the case of SMM J123549.44, OSIRIS only detects marginally faint diffuse emission, and so we do not estimate a dynamical mass.

Assuming typical sizes of $\sim 0.5 - 1''$ or $4 - 8$ kpc, S04 find a typical mass of $M_{dyn} \sim (1 - 2) \times 10^{11} M_\odot$ for SMGs. For SMM J163650.43, they distinguish a narrow Hα component with FWHM$_{rest} = 306 \pm 47$ km s^{-1} which translates into a dynamical mass $M_{dyn} = (1.62 \pm 0.50) \times 10^{11}$ M$_\odot$ using Equation 4.5. This value agrees with our spatially resolved result (see Table 5.2). S04's NIRSPEC observations of SMM J030227.73, uncorrected for any AGN contamination to the integrated broad

Hα emission detected suggest a dynamical mass $M_{dyn} = (3.15 \pm 0.23) \times 10^{11}$ $M_{\odot}$. By excluding the contamination from AGNs to the width of the Hα line, our OSIRIS results lead to a significantly lower and more reliable dynamical mass than that derived in long-slit observations.

From Fig. 5.7 we can see that the Hα emission within the diffuse region is concentrated in 2–3 multiple clumps. Due to the low S/N of the Hα line in these individual components, we cannot derive explicitly dynamical masses for the individual clumps. We compare sizes and σ-values for these regions to those reported for LBGs by Erb et al. (2003) and Law et al. (2007): for the three SMGs in our sample we find that with values of $\sigma_{rest} \lesssim 200$ km s^{-1} within the regions of diffuse emission and clump sizes $R \sim 1$ kpc (see middle panel in Figs. 5.2, 5.4, 5.6 and Fig. 5.7). The individual clumps that compose the diffuse emission in SMGs thus have similar properties to that of individual LBGs. We come back to this discussion in the following section.

Greve et al. (2005) report dynamical masses in the range $M_{dyn} = 0.3{-}37 \times 10^{10}$ $M_{\odot}$ derived from CO (3-2) observations in a large sample of 18 SMGs. Similar results have been obtained from high-resolution CO observations by Neri et al. (2003) and Tacconi et al. (2006, 2008). We do not have a direct comparison to the dynamical masses measured in CO for SMM J030227.73 or SMM J163650.43, but our results are consistent with the range of lower limits from CO masses found for SMGs. The similarity in these results suggest that the molecular gas – as traced by CO – and the ionized gas – traced by the Hα emission to which we have unique spatially-resolved access with OSIRIS – both appear to map similar baryonic dynamics.

5.5.2 Hα Sizes and Gas Masses

The integral field view of Hα emission in a galaxy can give us clues as to the distribution of star-formation activity per projected area, by associating the Hα integrated line flux at each pixel with a local SFR, following Equation 5.1, taking into account the pixel scale (50 mas or 100 mas) used for the OSIRIS observations. In Fig. 5.7 we show maps of (projected) SFR surface densities ($\Sigma_{\rm SFR}$) for the three SMGs in our

Table 5.2. Summary of *OSIRIS* IFU Results

	SMM J030227.73	SMM J123549.44	SMM J163650.43
z_{opt}	1.408	2.203	2.378
$z_{H\alpha}$	1.4076	2.2032	2.385
$S_{H\alpha}$ (broad) [erg s^{-1} cm^{-2}]	$1.02 \pm 0.06 \times 10^{-15}$	$5.35 \pm 0.13 \times 10^{-15}$	$1.04 \pm 0.06 \times 10^{-15}$
$S_{H\alpha}$ (narrow) [erg s^{-1} cm^{-2}]	$0.59 \pm 0.04 \times 10^{-15}$	–	$0.25 \pm 0.03 \times 10^{-15}$
FWHM$_{rest}$ (broad) [km s^{-1}]	1070 ± 76	1390 ± 50	2400 ± 134
FWHM$_{rest}$ (narrow) [km s^{-1}]	110 ± 15	–	475 ± 60
$[NII]/H\alpha$	0.53 ± 0.1	0.2 ± 0.1	–
SFR$_{\rm diffuse}$ [M$_\odot$ yr^{-1}] [a]	293 ± 10	278 ± 82	559 ± 23
$\Sigma_{\rm SFR}$ [M$_\odot$ yr^{-1} kpc^{-2}] [b]	1.38 ± 0.37	–	4.76 ± 0.42
Size $_{\rm compact}$	$0.7 \times 0.7''$	$0.7 \times 0.7''$	$0.4 \times 0.4''$
	6×6 kpc^2	5.9×5.9 kpc^2	3.3×3.3 kpc^2
Size $_{\rm diffuse}$	$1.1 \times 1.5''$	$1.1 \times 0.7''$	$1 \times 1''$
	9.4×12.8 kpc^2	9.2×5.9 kpc^2	8.3×8.3 kpc^2
Size $_{\rm total}$	$2.0 \times 1.7''$	$1.3 \times 0.9''$	$1 \times 1''$
	17.0×14.5 kpc^2	10.9×7.5 kpc^2	8.3×8.3 kpc^2
M$_{\rm dyn}$ [M$_\odot$]	$(4.3 \pm 0.6) \times 10^{10}$	–	$(2.0 \pm 0.5) \times 10^{11}$
M$_{\rm gas}$ [M$_\odot$] [c]	$(2.5 \pm 0.7) \times 10^{10}$	$(9.0 \pm 0.6) \times 10^{10}$	$(3.5 \pm 1.4) \times 10^{10}$

[a] Observed SFRs as measured from the observed Hα line, not corrected for extinction.

[b] SFR surface densities within the diffuse region, from the Hα-derived SFR at each pixel, divided by the pixel area.

[c] Gas masses derived from our extinction-corrected $\Sigma_{\rm SFR}$, assuming the Schmidt-Kennicutt relation. We correct for the expected overestimate resulting from the inherent assumption of a H_2–CO conversion factor appropriate for normal galaxies, rather than ULIRGs. See §5.5.2 for details.

sample, corrected for extinction based on typical Balmer decrements found in SMGs (Takata et al. 2006; see §4.5.2 for details).

We find extinction-corrected SFR surface densities $\Sigma_{\rm SFR} \sim 10-100$ M$_\odot$ yr^{-1} kpc^{-2} within the regions of diffuse emission in SMM J030227.73 and SMM J163650.43. These values set SMGs within the high range of $\Sigma_{\rm SFR}$ values found for local circumnuclear starbursts, but $2-3$ orders of magnitude higher than in normal spirals (see Fig. 9 in Kennicutt 1998). They are also on the high end of the $\Sigma_{\rm SFR}$ distribution for the optically-selected LBGs (see Law et al. 2007), and significantly higher than the LBG median, $<\Sigma_{\rm SFR}>= 2.9$ M$_\odot$ yr^{-1} kpc^{-2} (see Fig. 3 in Erb et al. 2006a). Note that the SMGs in our sample exhibit SFR surface densities that remain *below* the highest values of $\Sigma_{\rm SFR}$ found in local starbursts by approximately two orders of magnitude. These results, together with the spatially-extended Hα distribution $\gtrsim 1''$, suggests that SMGs have similar intermediately high rates of star formation as local circumnuclear starbursts. However, SMGs appear to be undergoing this intense activity on

much larger spatial scales, reflecting their much greater luminosity.

By tracing the regions undergoing star formation, the distribution of (narrow-line) Hα emission can also provide us with a mapping of the star-forming molecular and presumably gas-rich regions that fuel this activity. Even though CO observations have a direct view of the distribution of molecular gas throughout a galaxy, the ionized gas surrounding massive stars is expected to mix with the molecular gas medium, thus giving an additional window to characterize the molecular gas budget of a galaxy. We assume the validity of the local Schmidt Law presented by Kennicutt (1998) (hereafter, the *Schmidt-Kennicutt* relation) to associate the global SFR surface density with the gas surface density ($\Sigma_{\rm gas}$) in these galaxies:

$$\Sigma_{\rm SFR} = (2.5 \pm 0.7) \times 10^{-4} \times (\Sigma_{\rm gas})^{1.4\pm0.15}, \tag{5.2}$$

where $\Sigma_{\rm SFR}$ is in units of [$M_\odot$ yr^{-1} kpc^{-2}] and $\Sigma_{\rm gas}$ in [$M_\odot$ pc^{-2}]. When referring to *gas* masses, we assume that the molecular gas component comprises the bulk of the total gas. This is a reasonable assumption, as it has been shown that in nearby starbursts the atomic gas comprises less than a few percent of the total gas mass (e.g., Sanders & Mirabel 1996).

We note that the Schmidt-Kennicutt relation relies – for the sake of simplicity – on the assumption that a common CO-to-H_2 conversion factor can be used for all galaxies (see Kennicutt 1998). In particular, it assumes a conversion factor valid for nearby normal galaxies, M(H_2)= $X_{CO}L'_{CO(1-0)}$, where $X_{CO} \simeq 4.6$. However, the validity of this assumption is disputed: this conversion factor systematically overestimates gas masses in local ULIRGs (Solomon & Vanden Bout 2005). The physical basis for the CO-to-H_2 relation in normal galaxies relies on the assumption that molecular gas principally lies within gravitationally bound, virialized clouds. In the case of ULIRGs, a more appropriate gas-distribution model is that of CO emission arising from an intercloud medium, so that CO kinematics not only reflect gas masses, but also dynamical masses from stars intermixed in this medium. Hence, a conversion factor $X_{CO} \simeq 0.8$ K km s^{-1} pc^2 has been adopted as a more appropriate conversion

factor for ULIRGs (see also Tacconi et al. 2008). Taking this into account, we assume that gas masses calculated from the $\Sigma_{\rm gas}$ derived from the Schmidt-Kennicutt relation will likely be overestimated by a factor of $\sim 4.6/0.8 \simeq 6$.

Keeping these caveats in mind, we use the Schmidt-Kennicutt relation to estimate gas densities and assuming a typical Hα extinction correction for SMGs (see §4.5.2), we obtain $\Sigma_{\rm gas} \sim 10^3 - 10^4$ M$_\odot$ pc^{-2}, similar to the findings of Greve et al. (2005) and Tacconi et al. (2006, 2008) based on CO observations of SMGs. For the observed sizes over which we detect nebular emission and considering the caveats discussed above, we estimate gas masses $M_{\rm gas} \sim \Sigma_{\rm SFR} \times R^2 = (2.5 \pm 0.7), (9.0 \pm 0.6)$, and $(3.5 \pm 1.4) \times 10^{10}$ M$_\odot$ for SMM J030227.73, SMM J123549.44 and SMM J163650.43, respectively. The quoted errors correspond to the deviation in flux values found within the extended region of emission. More accurate uncertainties are estimated to amount to $\gtrsim 30\%$.

These gas masses are similar to those found in LBGs ($< M(H_2) >= 3.0 \times 10^{10}$ M$_\odot$ within a typical radius of ~ 2 kpc; see Erb et al. 2006b; Law et al. 2007). Furthermore, CO interferometric observations of low-redshift ULIRGs show that such extreme local objects are also gas-rich, M$(H_2) \sim 10^9 - 4 \times 10^{10}$ M$_\odot$, with typical spatial extensions of $\lesssim 1$ kpc (e.g., Young & Scoville 1991). Therefore, even though SMGs appear to be just as or even more gas-rich than these other galaxy populations, the typical sizes over which molecular gas extends for SMGs are significantly larger, though some of the brightest and most massive LBGs do appear to have more comparable Hα spatial extensions ($R_{H\alpha} \sim 2 - 7$ kpc; Förster Schreiber et al. 2006).

Together with the finding that SFR surface densities in SMGs are similar to those found in circumnuclear starbursts and higher than those in LBGs, these gas masses suggest that SMGs are consuming their available gas rapidly. With extinction-corrected SFRs from the diffuse regions in SMGs $\sim 1000 - 2000$ M$_\odot$ yr^{-1}, we estimate that SMGs will deplete their gas reservoirs on a timescale of $M_{\rm gas}$/SFR$\simeq 10^8$ yr. Considering the short gas-depletion timescale, this suggests that the SMG phase represents a very short episode in the evolution history of a galaxy.

5.5.2.1 Comparison to CO-Derived Gas Masses

The gas masses we estimate agree with the average value determined from CO observations of SMGs (Greve et al. 2005; Tacconi et al. 2006, 2008). Assuming a CO-to-H_2 conversion factor appropriate for local ULIRGs, Greve et al. (2005) measure a median molecular gas mass $< M(H_2) > \ = \ (3.0 \ \pm \ 1.6) \ \times \ 10^{10}$ $M_\odot$. Tacconi et al. (2008) undertook high-resolution CO observations of four SMGs, including SMM J123549.44, and found $M_{gas}(CO) \ = \ (4 \ \pm \ 0.5) \ \times \ 10^{10}$ $M_\odot$ for SMM J123549.44, comparable with our result.

We note that CO observations typically target high-J ($J \geq 2$) CO transitions, rather than the lowest (1-0) transition. The former trace warm and dense gas, while the latter trace the likely more abundant and colder gas. Hainline et al. (2006) reported the first detection of CO(1-0) emission from SMM J13120+4242 with the Green Bank Telescope, deriving a cold molecular gas mass of $M_{CO(1-0)} \ = \ 1.6 \ \times \ 10^{11}$ $M_\odot$, four times larger than that derived from the higher CO(4-3) transitions (Greve et al. 2005). This suggests that a large fraction of molecular gas is likely left unaccounted for when tracing CO through the higher J-transitions and that the true gas masses are likely closer to 4× these higher-J estimates.

There are also important caveats to keep in mind when relying on the ionized gas to map the distribution of gas across a galaxy, three which we briefly mention here. First, even though in the near-IR we are less prone to dust obscuration than in the optical, dust extinction is still an important factor. We have accounted for attenuations in observed Hα luminosities considering the typical optical depth derived from the Balmer decrement in SMGs (Takata et al. 2006). However, dust extinction in excess of the Balmer decrement would likely translate into lower estimates for gas masses. Second, our observations are limited to the OSIRIS FOV, such that we do not see the extent of the ionized gas beyond a radial distance of $R \sim 1-2''$ or $8-16$ kpc from the center. The third caveat we note is that our observations are only sensitive to regions with the highest surface brightness, ignited by massive star formation. Therefore, our gas estimates are likely lower limits that fail to uncover the full extent of the gas

reservoir in these galaxies, which is likely traced to a better degree by CO observations of low-J transitions. However, even with these caveats in mind, the consistency of CO-derived gas mass estimates for SMGs with our Hα-derived values suggests that the spatial scale of ionized gas may be a viable venue to explore the distribution and abundance of gas fueling in high-redshift star-forming galaxies. Furthermore, recent high-resolution CO observations have shown that the CO emission can be displaced (and sometimes completely disjoint) from the distribution of the ionized gas (see Fig. 3 in Tacconi et al. 2008 for a clear example). This enigmatic result shows that we are only starting to unveil the intricacies of the gaseous kinematics within these galaxies. This motivates further the use of AO to probe the details of the distribution of the near-IR emitting gas.

With the gas masses derived from the extinction-corrected Hα emission (see Table 5.2) and considering the stellar masses derived from broad-band photometry ($M_{stellar} = 2.51 \pm 2.65 \times 10^{11}$ $M_{\odot}$; Borys et al. 2005), we estimate an average gas fraction of $< M_{\rm gas}/M_{stellar} > \sim 0.1 - 0.4$. If we consider the gas masses derived from CO emission (Greve et al. 2005) and boosted by the factor of four suggested by the work from Hainline et al. (2006), this gas fraction increases to ~ 0.5 (see also Neri et al. 2003). These results reinforce the conclusion that SMGs are gas-rich systems.

The preponderance of multiple galactic-scale sub-components in SMGs – as revealed by CO and both our IFU observations and those of S06 – together with the disturbed morphology reminiscent of interacting systems (Smail et al. 2004) suggests that SMGs are likely the result of merging episodes between gas-rich galaxies. LBGs have also been found to have large gas fractions $\sim 50\%$ (Erb et al. 2006b). Putting this together with the similar velocity dispersions and Hα emission sizes found in the individual clumps comprising the diffuse emission in SMGs to that of individual LBGs, these results suggest that the mergers in SMGs resemble mergers of $2 - 3$ 'LBG-like' sub-units.

5.6 Conclusions

We present the first integral-field spectroscopic LGS-AO observations on SMGs. We distinguish spatially the compact broad-Hα emission associated with an AGN and the extended narrow-Hα emission associated with star formation. We have thus improved our understanding on the internal dynamics of this enigmatic galaxy population and make reliable estimates of SMG masses and SFRs, uncontaminated by AGN and star formation mixing of rest-optical lines.

We do not find any indication of ordered motion within our targets. We find relative velocities of a few 100 km s^{-1} between galactic-scale sub-components in two of our targets, suggesting that these might be the remnants of originally independent systems undergoing a merger. Even after eliminating the influence of AGN activity, we measure large extinction-corrected SFRs $\sim 1000 - 2000$ M$_\odot$ yr^{-1} and large gas masses $M(H_2) \sim 10^{10}$ M$_\odot$. These gas masses are similar to those found in local ULIRGs and high-redshift LBGs, but the spatial extent over which Hα emission extends is significantly larger in SMGs, $\sim 8 - 16$ kpc. Furthermore, SMGs display similar SFR surface densities to local circumnuclear starbursts. All of these results taken together suggest that the submillimeter phase denotes a short-lived flaring-up of large spatial extension across these systems that rapidly depletes the available gas through intense star formation.

Acknowledgements We thank Thiago S. Gonçalves, David R. Law and Mark Swinbank, for helpful and insightful discussions on the treatment and analysis of OSIRIS observations. We are also grateful to the Keck support team for the fantastic on-site help in obtaining these observations, in particular to Al Conrad, Randy Campbell, Hien Tran, David LeMignant, Jim Lyke and Christine Melcher.

Chapter 6

Summary

At the time of their discovery in the late 1990's, SMGs founded a new observational field: they afforded the opportunity to study galaxies that made up the bulk of (obscured) stellar growth at cosmologically-significant redshifts ($z \gtrsim 2$) that had until then remained inconspicuous in optical/UV surveys. With ultra-luminous energetic outputs ($L_{IR} \gtrsim 10^{12}$ $L_{\odot}$; C05), large stellar masses ($M_{stellar} \sim 10^{11}$ $M_{\odot}$) and inferred high SFRs $\gtrsim$ 1000 $M_{\odot}$ yr^{-1} (Borys et al. 2005), SMGs are prime candidates for the progenitors of the most massive galaxies at $z \sim 0$ and the likely major stellar build-up sites at $z \sim 2$ (Lilly et al. 1999; Smail et al. 2004).

At low redshifts, a plethora of studies have shown that dust-enshrouded galaxies with comparable luminosities have complex, disturbed morphologies (e.g., Soifer et al. 2000; Scoville et al. 2000), with intense starburst and AGN activity concentrated in a compact region ($\lesssim$ 1 kpc; Charmandaris et al. 2002), suggestive of a merger-driven origin. The extreme luminosities of distant SMGs match, but are they high-redshift analogs of local ultra-luminous infrared galaxies and do they host similar astrophysics?

In this thesis I have concentrated on the mid- and near-IR spectroscopic study of the sub-sample of SMGs with identified radio-counterparts and spectroscopic UV redshifts compiled by Chapman et al. (2005). Our main results are:

1. **SMGs are dominated by star formation.** From the mid-IR spectra of the largest sample observed to date with *Spitzer*-IRS we find that the majority of SMGs (80%) display strong PAH spectral features, while only a minority (12% of our sample) display continuum-dominated spectra. This indicates that SMGs are

undergoing intense star formation, and that some diversity in AGN contribution to the mid-IR is present within the population. However, from the composite SMG spectrum – as revealed by an enhanced hot-dust continuum at $\lambda_{rest} \sim 10$ μm – we determine that this AGN contribution is $\lesssim 35\%$ to the total luminous output. The SMG population is dominated by intense starburst activity and displays among the most luminous PAH features observed locally and at high redshift: it likely includes some of the most intense star-formation events ever witnessed in the Universe.

2. **SMGs have spatially extended mid-IR emission.** The observed ratio of PAH features – sensitive to the hardness of the ionization field and reddening – and the strength of the silicate absorption feature at $\lambda \sim 9.7$ μm – which provides insight into the distribution of dust along the line of sight – suggest lower extinction towards the mid-IR line and continuum emitting regions within SMGs, as compared with either local nuclear starbursts or ULIRGs. Given the compact mid-IR emission from local ULIRGs, the difference in extinction argues that the mid-IR emission in SMGs, both continuum and PAH-emission, arises in a more extended component ($\gg$ 1–2 kpc).

3. **SMGs display velocity offsets suggestive of powerful outflows.** We study the rest-frame optical line emission in a sample of SMGs to provide a more accurate redshift for the bulk of the gas in the ISM of the potential well of these galaxies. We find redshift differences between rest-frame UV and Hα lines amounting to $\sim$ *few* $\times$1000 km s^{-1}, which indicate that large velocity outflows are present. Considering the enriched chemical abundances hosted by SMGs, with near- to super-solar metallicities, such outflows are potentially powerful at transforming the intergalactic environments.

4. **SMGs have Hα extended emission, exceeding sizes of local ULIRGs.** With spatially-resolved integral field spectroscopy with Keck OSIRIS we distinguish multiple galactic-scale sub-components within a sample of SMGs, as traced by Hα emission. In particular, we distinguish spatially between regions bright in Hα emission that are dominated by AGN activity from those where star formation is taking place. We show that SMGs host SFR surface densities a factor of $\sim 2-6$ higher than the

median value for optically-selected high-redshift galaxies, but similar to local ULIRGs and circumnuclear starbursts, though the spatial extent of Hα emission is significantly larger in SMGs, $\sim 8-16$ kpc.

5. **SMGs comprise multiple galactic-scale sub-units.** We see no evidence for ordered orbital motion – such as would be present in a gaseous disk – but find relative velocities of $\sim few \times 100$ km s^{-1} between sub-components in individual SMGs. This may suggest that these sub-units are remnants of originally independent systems undergoing a merger. Considering the similarities between the individual clumps in SMGs with those of individual LBGs in terms of size and velocity dispersions – taken as a proxy of dynamical mass–, these results suggest that the mergers in SMGs may comprise multiple 'LBG-like' sub-units.

The dominant role of star formation in SMGs, their large dynamical and (estimated) gas masses and their wide spatial extension all suggest that the SMG phase denotes a flaring-up that rapidly depletes the available gas through intense star formation of large spatial extension across these systems. With extended emission ($\gtrsim 8-17$ kpc) beyond that found in local ULIRGs ($\lesssim 1$ kpc; Charmandaris et al. 2002), it is possible that the evolutionary stages prior to the SMG phase are distinct from the major mergers that produce local ULIRGs. Minor mergers may also play an important role in the assembly of galaxy mass (Guo & White 2007) and could potentially provide an additional origin to the SMG phase.

It has been a notorious challenge for galaxy formation models to reproduce the 850 μm counts – which require replicating the extreme luminosities of SMGs – without overshooting the number density of bright and massive galaxies at $z \sim 0$ (Granato et al. 2000; Baugh et al. 2005). Furthermore, under the assumption that SMGs are high-redshift analogs of local ULIRGs, the abundance of this galaxy population is contingent on the frequency of (major) galaxy mergers igniting powerful starbursts at these high redshifts. Therefore, the possibility of invoking less dramatic events to trigger an SMG phase in galaxies could hold promise in the context of galaxy formation theory.

6.1 Future Directions

Through this past decade, a collective multi-wavelength effort has enabled a steadily growing picture of the astrophysical details of SMGs (e.g., Ivison et al. 1998; Frayer et al. 1998, 1999; Blain et al. 1999, 2002; Chapman et al. 2004; Frayer et al. 2004; Sheth et al. 2004; Smail et al. 2004; Swinbank et al. 2004; C05; Greve et al. 2005; Kneib et al. 2005; Lutz et al. 2005; Takata et al. 2006; Hainline et al. 2006, 2009; Tacconi et al. 2006, 2008; Menéndez-Delmestre et al. 2007, 2008; Valiante et al. 2007; Younger et al. 2007; Pope et al. 2008). The research presented in this thesis comprises a significant step towards understanding the astrophysical properties of the ensemble of SMGs, and also suggests a number of (clear) paths for furthering their investigation. In particular, the OSIRIS results that we have presented comprise merely a few objects of a nascent observing program. We are in the process of increasing our sample with the aim of furthering our understanding of the inner dynamics in SMGs as traced by the ionized near-IR emitting gas. Furthermore, we have initiated an effort to combine the power of spatially-resolved Hα OSIRIS spectroscopy with deep imaging with the Keck near-IR camera NIRC-2 in conjuction with LGS-AO to probe the detailed near-IR continuum morphology and stellar colors of the lower surface-brightness extended stellar component of SMGs. The combination of existing *HST*-ACS data (Smail et al. 2004) and high-resolution near-IR imaging will allow us to estimate SEDs of kpc-scale components within SMGs and to provide an insight into color gradients and thus the distribution of obscuration in these systems.

In the near future, the upcoming launch of the *Herschel* Space Observatory will extend our exploration of the extragalactic Universe to encompass the longer IR wavelengths beyond the *Spitzer* view. *Herschel* GTO programs have already been approved for $\lambda \sim 110 - 500$ μm imaging of the HDF, Lockman Hole, and Groth Strip fields, as part of two large collaborations: the PACS Evolutionary Probe (PEP) and the Herschel Multi-tiered Extragalactic Survey (HerMES). These observations will map rest-frame $\lambda \gtrsim 24$ μm for $z \gtrsim 2$ galaxies, which can give us additional insight to the ongoing star-formation activity. They will also provide for better constraints of

the far-IR SED of SMGs, which will give us a better understanding of their typical dust temperatures and luminosities.

We make special note that the target of most SMG studies has been the radio-identified sample of SMGs with precise positions on the sky (within $\sim 1''$) and spectroscopically-confirmed UV redshifts compiled by C05. However, $\sim 30\%$ of the sources uncovered at $\lambda = 850-1100$ μm do not display a sufficiently bright radio counterpart for unambiguous identification and their follow-up study at other wavelengths has been slower as a consequence. As discussed in Chapter 3, it is still unclear whether inherent differences in dust temperatures and/or differences in redshift distributions exist between SMGs with identified radio-counterparts and those without (Chapman et al. 2004; Younger et al. 2007). The first step towards characterization of this radio-undetected SMG population is to obtain accurate positions ($\lesssim 1''$), to undertake spectroscopic follow-up and obtain reliable redshifts. The Submillimeter Array (SMA) and the Combined Array for Research in mm-wave Astronomy (CARMA) are currently available instruments that has been shown to be suitable for this task (Younger et al. 2007; Sheth, K. et. al. in prep).

In only a few years the Atacama Large Millimeter/submm Array (ALMA) will come online with a resolution $\sim 0.005''$ at the highest frequencies that will surpass that of Hubble and the VLA by a factor of ~ 10. These high-resolution observing capabilities will not only allow for accurate positions of SMGs, but will also allow the detailed mapping of molecular gas morphology and mass as traced by CO rotation lines ($J > 2$) without incurring in the extremely demanding typical observing times ($\gtrsim 30$ hrs per source) that are currently necessary (Neri et al. 2003; Greve et al. 2005; Tacconi et al. 2006, 2008). ALMA will also enable high-resolution imaging in the mm/submm bands down to the sub-mJy flux level, avoiding the problem of confusion that has limited current submm cameras to $\gtrsim 2$ mJy and pushing the detection limit down to the realm of more *normal* galaxies at the SMG redshifts.

Bibliography

Adelberger, K. L., Steidel, C. C., Shapley, A. E., & Pettini, M. 2003, ApJ, 584, 45

Adelman-McCarthy, J. K., et al. 2008, ApJS, 175, 297

Allamandola, L. J., Tielens, A. G. G. M., & Barker, J. R. 1989, ApJS, 71, 733

Alexander, D. M., Bauer, F. E., Chapman, S., Smail, I., Blain, A., Brandt, W. N., Ivison, R. 2005, ApJ, 632, 736 (A05)

Alexander, D. M., Smail, I., Bauer, F. E., Chapman, S. C., Blain, A. W., Brandt, W. N., & Ivison, R. J. 2005, Nature, 434, 738

Alexander, D. M., Chary, R. R., Pope, A., Bauer, F. E., Brandt, W. N., Daddi, E., Dickinson, M., Elbaz, D.m Reddy, N. A. 2008, ArXiv e-prints, 803, arXiv:0803.0636

Alexander, D. M., et al. 2008, AJ, 135, 1968

Alonso-Herrero, A., Colina, L., Packham, C., Díaz-Santos, T., Rieke, G. H., Radomski, J. T., Telesco, C. M. 2006, ApJ, 652, 83

Armus, L., Heckman, T. M., & Miley, G. K. 1989, ApJ, 347, 727

Armus, L. et al. 2004, ApJS, 154, 178

Armus, L. et al. 2006, ApJ, 640, 204

Armus, L., et al. 2007, ApJ, 656, 148

Barger, A. J., Cowie, L. L., & Sanders, D. B. 1999, ApJ, 518, L5

Barger, A. J., Cowie, L. L., Smail, I., Ivison, R. J., Blain, A. W., & Kneib, J.-P. 1999, AJ, 117, 2656

Baugh, C. M., Lacey, C. G., Frenk, C. S., Granato, G. L., Silva, L., Bressan, A., Benson, A. J., & Cole, S. 2005, MNRAS, 356, 1191

Bertoldi, F., et al. 2000, A&A, 360, 92

Biggs, A.D., Ivison, R.J., 2008, MNRAS, 385, 893

Blain, A. W., Smail, I., Ivison, R. J., & Kneib, J.-P. 1999, MNRAS, 302, 632

Blain, A., Smail, I., Ivison, R., Kneib, J.-P., Frayer, D. T. 2002, Phys. Rep., 369, 111B

Blain, A. W., Chapman, S. C., Smail, I., & Ivison, R. 2004, ApJ, 611, 725

Borys, C., Chapman, S., Halpern, M., & Scott, D. 2003, MNRAS, 344, 385

Borys, C., Scott, D., Chapman, S., Halpern, M., Nandra, K., & Pope, A. 2004, MNRAS, 355, 485

Borys, C., Smail, I., Chapman, S. C., Blain, A. W., Alexander, D. M., & Ivison, R. J. 2005, ApJ, 635, 853

Borys, C., et al. 2006, ApJ, 636, 134

Bouché, N., Lehnert, M. D., Aguirre, A., Péroux, C., & Bergeron, J. 2007, MNRAS, 378, 525

Brandl, B. R. et al. 2006, ApJ, astro-ph/0609024

Buat, V., Boselli, A., Gavazzi, G., & Bonfanti, C. 2002, A&A, 383, 801

Calzetti, D., Kinney, A. L., & Storchi-Bergmann, T. 1994, ApJ, 429, 582

Calzetti, D., Armus, L., Bohlin, R. C., Kinney, A. L., Koornneef, J., & Storchi-Bergmann, T. 2000, ApJ, 533, 682

Caputi, K. I., et al. 2007, ApJ, 660, 97

Carilli, C. L., & Yun, M. S. 1999, ApJ, 513, L13

Chakrabarti, S., Fenner, Y., Hernquist, L., Cox, T. J., & Hopkins, P. F. 2006, ArXiv Astrophysics e-prints, arXiv:astro-ph/0610860

Chapman, S., Blain, A., Ivison, R., Smail, I. 2005, Nature, 422, 695

Chapman, S. C., Smail, I., Blain, A. W., & Ivison, R. J. 2004, ApJ, 614, 671

Chapman, S., Blain, A., Smail, I., Ivison, R. 2005, ApJ, 622, 772 (C05)

Charmandaris, V., et al. 2002, A&A, 391, 429

Colina, L., & Bohlin, R., Castelli, F. 1996, Absolute Flux Calibrated Spectrum of Vega (STSci Rep. OSG-CAL-96-01; Baltimore; STSci)

Condon, J. J. 1992, ARA&A, 30, 575

Coppin, K., Halpern, M., Scott, D., Borys, C., & Chapman, S. 2005, MNRAS, 357, 1022

Coppin, K., et al. 2008, MNRAS, in press, arXiv:0806.0618

Cowie, L. L., Barger, A. J., & Kneib, J.-P. 2002, AJ, 123, 2197

Croton, D. J. 2006a, MNRAS, 369, 1808

Croton, D. J., et al. 2006b, MNRAS, 365, 11

Daddi, E., Cimatti, A., Renzini, A., Fontana, A., Mignoli, M., Pozzetti, L., Tozzi, P., & Zamorani, G. 2004, ApJ, 617, 746

Dawson, S., McCrady, N., Stern, D., Eckart, M. E., Spinrad, H., Liu, M. C., & Graham, J. R. 2003, AJ, 125, 1236

Davies, R. I. 2007, MNRAS, 375, 1099

Deo, R. P., Crenshaw, D. M., Kraemer, S. B., Dietrich, M., Elitzur, M., Teplitz, H., & Turner, T. J. 2007, ApJ, 671, 124

Desai, V. et al. 2006, ApJ, 641, 133

Desai, V., et al. 2007, ApJ, 669, 810

Dickinson, M., Papovich, C., Ferguson, H. C., & Budavári, T. 2003, ApJ, 587, 25

Dole, H., et al. 2006, A&A, 451, 417

Dowell, C. D., et al. 2003, Proceedings of the SPIE, 4855, 73

Downes, D., & Solomon, P. M. 1998, ApJ, 507, 615

Draine, B. T. 2003, ARA&A, 41, 241

Draine, B. T., & Li, A. 2007, ApJ, 657, 810

Eales, S., Lilly, S., Gear, W., Dunne, L., Bond, J.R., Hammer, F., Le Fèvre, O., & Crampton, D. 1999, ApJ, 515, 518

Elbaz, D., Cesarsky, C. J., Chanial, P., Aussel, H., Franceschini, A., Fadda, D., & Chary, R. R. 2002, A&A, 384, 848

Erb, D. K., Shapley, A. E., Steidel, C. C., Pettini, M., Adelberger, K. L., Hunt, M. P., Moorwood, A. F. M., & Cuby, J.-G. 2003, ApJ, 591, 101

Erb, D. K., Steidel, C. C., Shapley, A. E., Pettini, M., Reddy, N. A., & Adelberger, K. L. 2006, ApJ, 647, 128

Erb, D. K., Steidel, C. C., Shapley, A. E., Pettini, M., Reddy, N. A., & Adelberger, K. L. 2006, ApJ, 646, 107

Förster Schreiber, N. M., Sauvage, M., Charmandaris, V., Laurent, O., Gallais, P., Mirabel, I. F., Vigroux, L. 2003, A&A, 399, 833

Förster Schreiber, N. M., Roussel, H., Sauvage, M., & Charmandaris, V. 2004, A&A, 419, 501

Förster Schreiber, N. M., et al. 2006, ApJ, 645, 1062

Franx, M., et al. 2003, ApJ, 587, L79

Frayer, D. T., Ivison, R., Scoville, N. Z., Yun, M., Evans, A. S., Smail, I., Blain, A., Kneib, J.-P. 1998, ApJ, 506, L7

Frayer, D. T., et al. 1999, ApJ, 514, L13

Frayer, D. T., Reddy, N. A., Armus, L., Blain, A. W., Scoville, N. Z., & Smail, I. 2004, AJ, 127, 728

Galliano, F., Madden, S. C., Tielens, A. G. G. M., Peeters, E., & Jones, A. P. 2008, ApJ, 679, 310

Garrett, M. A. 2002, A&A, 384, L19

Genzel, R. et al. 1998, ApJ, 498, 579

Gispert, R., Lagache, G., & Puget, J. L. 2000, A&A, 360, 1

Glenn, J., et al. 1998, Proceedings of the SPIE, 3357, 326

Granato, G. L., Lacey, C. G., Silva, L., Bressan, A., Baugh, C. M., Cole, S., & Frenk, C. S. 2000, ApJ, 542, 710

Greve, T. R., et al. 2005, MNRAS, 359, 1165

Guo, Q., & White, S. 2007, ArXiv e-prints, 708, arXiv:0708.1814

Hainline, L. J., Blain, A. W., Greve, T. R., Chapman, S. C., Smail, I., & Ivison, R. J. 2006, ApJ, 650, 614

Hainline, L. J., Blain, A. W., Smail, I., Frayer, D., Chapman, S. C., Ivison, R. 2008, in prep.

Hao, L., Weedman, D. W., Spoon, H. W. W., Marshall, J. A., Levenson, N. A., Elitzur, M., & Houck, J. R. 2007, ApJl, 655, L77

Heckman, T. M., Armus, L., & Miley, G. K. 1990, ApJS, 74, 833

Heckman, T. M. 2001, Gas and Galaxy Evolution, ASP Conference Proceedings, Vol. 240, 345. Edited by John E. Hibbard, Michael Rupen, and Jacqueline H. van Gorkom

Helou, G., Soifer, B. T., & Rowan-Robinson, M. 1985, ApJ, 298, L7

Helou, G. 1999, "The Universe as Seen by ISO". Eds. P. Cox & M. F. Kessler. ESA-SP 427., 797

Ho, P. T. P. 2000, Imaging at Radio through Submillimeter Wavelengths, 217, 227

Holland, W. S., et al. 1999, MNRAS, 303, 659

Horne, K. 1986, PASP, 98, 609

Houck, J. R. et al. 2004 ApJS, 154, 18

Houck, J. R. et al. 2005 ApJ, 622, 105

Kauffmann, G., & White, S. D. M. 1993, MNRAS, 261, 921

Kneib, J.-P., Neri, R., Smail, I., Blain, A., Sheth, K., van der Werf, P., & Knudsen,K. K. 2005, A&A, 434, 819

Ivison, R. J., Smail, I., Le Borgne, J.-F., Blain, A. W., Kneib, J.-P., Bezecourt, J., Kerr, T. H., & Davies, J. K. 1998, MNRAS, 298, 583

Ivison, R. J., Smail, I., Barger, A. J., Kneib, J.-P., Blain, A. W., Owen, F. N., Kerr, T. H., & Cowie, L. L. 2000, MNRAS, 315, 209

Ivison, R. J., et al. 2002, MNRAS, 337, 1

Kennicutt, R. C., Jr. 1998, ApJ, 498, 541

Knudsen, K. K., et al. 2006, MNRAS, 368, 487

Komossa, S., Burwitz, V., Hasinger, G., Predehl, P., Kaastra, J. S., Ikebe, Y. 2003 ApJ, 582, 15

Kovács, A., Chapman, S., Dowell, C. D., Blain, A., Ivison, R., Smail, I., Phillips, T. G. 2006, ApJ, 650, 592

Krabbe, A., Böker, T., Maiolino, R. 2001 ApJ, 557, 626

Kreysa, E., et al. 1998, Proceedings of the SPIE, 3357, 319

Larkin, J., et al. 2006, Proceedings of the SPIE, 6269, 62691A

Laurent, O., Mirabel, I. F., Charmandaris, V., Gallais, P., Madden, S. C., Sauvage, M., Vigroux, L., Cesarsky, C. 2000, A&A, 359, 887

Law, D. R., Steidel, C. C., & Erb, D. K. 2006, AJ, 131, 70

Law, D. R., Steidel, C. C., Erb, D. K., Larkin, J. E., Pettini, M., Shapley, A. E., & Wright, S. A. 2007, ApJ, 669, 929

Le Floc'h, E., et al. 2005, ApJ, 632, 169

Levenson, N. A., Sirocky, M. M., Hao, L., Spoon, H. W. W., Marshall, J. A., Elitzur, M., & Houck, J. R. 2007, ApJl, 654, L45

Lilly, S. J., Eales, S. A., Gear, W. K. P., Hammer, F., Le Fèvre, O., Crampton, D., Bond, J. R., & Dunne, L. 1999, ApJ, 518, 641

Lira, P., Ward, M. J., Zezas, A., & Murray, S. S. 2002, MNRAS, 333, 709

Lutz, D., Maiolino, R., Spoon, H. W. W., & Moorwood, A. F. M. 2004, A&A, 418, 465

Lutz, D., Valiante, E., Sturmn, E., Genzel, R., Tacconi, L., Lehnert, M., Sternberg, A., Baker, A. 2005 ApJ, 625, 83 (L05)

Lutz, D., et al. 2007, ApJl, 661, L25

Maraston, C., Daddi, E., Renzini, A., Cimatti, A., Dickinson, M., Papovich, C., Pasquali, A., & Pirzkal, N. 2006, ApJ, 652, 85

McCarthy, J. K., et al. 1998, Proceedings of the SPIE, 3355, 81

McLean, I. S., et al. 1998, Proceedings of the SPIE, 3354, 566

Menéndez-Delmestre, K., et al. 2007, ApJl, 655, L65

Menéndez-Delmestre, K., et al. submitted to ApJ

Monaco, P., Fontanot, F., & Taffoni, G. 2007, MNRAS, 375, 1189

Narron, R., Ogle, P., Laher, R. R. 2006 ADASS XVI Conference, Tucson, Arizona

Neri, R., et al. 2003, ApJl, 597, L113

Neufeld, D. A. 1991, ApJ, 370, L85

Ogle, P., Whysong, D., & Antonucci, R. 2006, ApJ, 647, 161

Oke, J. B., et al. 1995, PASP, 107, 375

Osterbrock, D. E. 1989, Astrophysics of Gaseous Nebulae and Active Galactic Nuclei (University Science Books: Mill Valley, California)

Peeters, E., Spoon, H. W. W., Tielens, A., G., G., M. 2004, ApJ, 613, 986

Pettini, M., & Pagel, B. E. J. 2004, MNRAS, 348, L59

Pope, A. et al. 2006, MNRAS, 370, 1185

Pope, A. et al. 2006, ApJ, astro-ph/0711.1553

Puchnarewicz, E. M., et al. 1997, MNRAS, 291, 177

Richards, E. A. 2000, ApJ, 533, 611

Richards, G. T., Vanden Berk, D. E., Reichard, T. A., Hall, P. B., Schneider, D. P., SubbaRao, M., Thakar, A. R., & York, D. G. 2002, AJ, 124, 1

Rieke, G. H., et al. 2004, ApJS, 154, 25

Rigopoulou, D., Spoon, H. W. W., Genzel, R., Lutz, D., Moorwood, A. F. M., Tran, Q. D. 1999, AJ, 118, 2625

Rigopoulou, D., et al. 2006, ApJ, 648, 81

Risaliti, G., et al. 2006, MNRAS, 365, 303

Roussel, H., Sauvage, M., Vigroux, L., & Bosma, A. 2001, A&A, 372, 427

Sajina, A., Yan, L., Armus, L., Choi, P., Fadda, D., Helou, G., & Spoon, H. 2007, ApJ, 664, 713

Salpeter, E. E. 1955, ApJ, 121, 161

Sanders, D. B., Soifer, B. T., Elias, J. H., Madore, B. F., Matthews, K., Neugebauer, G., & Scoville, N. Z. 1988, ApJ, 325, 74

Sanders, D. B., & Mirabel, I. F. 1996, ARA&A, 34, 749

Scott, S. et al. 2002, MNRAS, 331, 817

Scoville, N. Z., et al. 2000, AJ, 119, 991

Sheth, K., Blain, A. W., Kneib, J.-P., Frayer, D. T., van der Werf, P. P., & Knudsen, K. K. 2004, ApJ, 614, L5

Shi, Y., et al. 2006, ApJ, 653, 127

Simpson, C., Rawlings, S. 2000, MNRAS, 317, 1023

Smail, I., Ivison, R., Blain, A.1997, ApJ, 490L, 5S

Smail, I., Ivison, R. J., Blain, A. W., & Kneib, J.-P. 1998, ApJ, 507, L21

Smail, I., Ivison, R. J., Blain, A. W., & Kneib, J.-P. 2002, MNRAS, 331, 495

Smail, I., Chapman, S. C., Ivison, R. J., Blain, A. W., Takata, T., Heckman, T. M., Dunlop, J. S., & Sekiguchi, K. 2003, MNRAS, 342, 1185

Smail, I., Chapman, S. C., Blain, A. W., & Ivison, R. J. 2004, ApJ, 616, 71

Smith, J. D. T., et al. 2007, ApJ, 656, 770

Soifer, B. T., Sanders, D. B., Madore, B. F., Neugebauer, G., Danielson, G. E., Elias, J. H., Lonsdale, C. J., & Rice, W. L. 1987, ApJ, 320, 238

Soifer, B. T., & Neugebauer, G. 1991, AJ, 101, 354

Soifer, B. T., et al. 2000, AJ, 119, 509

Solomon, P. M., & Vanden Bout, P. A. 2005, ARA&A, 43, 677

Spoon, H. W. W., Keane, J. V., Tielens, A. G. G. M., Lutz, D., Moorwood, A. F. M., & Laurent, O. 2002, A&A, 385, 1022

Spoon, H. W. W., Moorwood, A. F. M., Lutz, D., Tielens, A. G. G. M., Siebenmorgen, R., Keane, J. V. 2004, A&A, 414, 873 (S04)

Steidel, C. C., Adelberger, K. L., Shapley, A. E., Pettini, M., Dickinson, M., & Giavalisco, M. 2003, ApJ, 592, 728

Steidel, C. C., Shapley, A. E., Pettini, M., Adelberger, K. L., Erb, D. K., Reddy, N. A., & Hunt, M. P. 2004, ApJ, 604, 534

Sturm, E., Lutz, D., Tran, D., Feuchtgruber, H., Genzel, R., Kunze, D., Moorwood, A. F. M., Thornley, M. D. 2000, A&A, 358, 481

Sturm, E., et al. 2006, ApJl, 653, L13

Swinbank, A. M., Smail, I., Chapman, S., Blain, A., Ivison, R., Keel, W. C. 2004, ApJ, 617, 64 (S04)

Swinbank, A. M., Chapman, S. C., Smail, I., Lindner, C., Borys, C., Blain, A. W., Ivison, R. J., & Lewis, G. F. 2006, MNRAS, 371, 465

Swinbank, A. M., et al. 2008, submitted to MNRAS

Tacconi, L. J., et al. 2006, ApJ, 640, 228

Tacconi, L. J., et al. 2008, ApJ, 680, 246

Takata, T., Sekiguchi, K., Smail, I., Chapman, S., Geach, J. E., Swinbank, A. M., Blain, A., Ivison, R. 2006, ApJ, astro-ph/0607580

Tecza, M., et al. 2004, ApJl, 605, L109

Teplitz, H. I., et al. 2007, ApJ, 659, 941

Tran, Q. D. et al. 2001, ApJ, 552, 527

Valiante, E., Lutz, D., Sturm, E., Genzel, R., Tacconi, L. J., Lehnert, M. D., & Baker, A. J. 2007, ApJ, 660, 1060

van Dam, M. A., et al. 2006, PASP, 118, 310

Veilleux, S., Kim, D.-C., Sanders, D. B., Mazzarella, J. M., & Soifer, B. T. 1995, ApJS, 98, 171

Veilleux, S., Kim, D.-C., & Sanders, D. B. 1999, ApJ, 522, 113

Veilleux, S., Kim, D.-C., & Sanders, D. B. 2002, ApJS, 143, 315

Voit, G. M. 1992, MNRAS, 258, 841

Webb, T. M., et al. 2003, ApJ, 587, 41

Webb, T. M. A., Lilly, S., Clements, D. L., Eales, S., Yun, M., Brodwin, M., Dunne, L., & Gear, W. 2003b, ApJ, 597, 680

Weedman, D. W., et al. 2005, ApJ, 633, 706

Weedman, D., et al. 2006, ApJ, 653, 101

Weedman, D. W., & Houck, J. R. 2008, ArXiv e-prints, 806, arXiv:0806.4101

White, S. D. M., & Rees, M. J. 1978, MNRAS, 183, 341

Wizinowich, P. L., et al. 2006, PASP, 118, 297

Wu, H., Cao, C., Hao, C.-N., Liu, F.-S., Wang, J.-L., Xia, X.-Y., Deng, Z.-G., & Young, C. K.-S. 2005, ApJl, 632, L79

Yan, L. et al. 2005, ApJ, 628, 604 (Y05)

Yan, L., et al. 2007, ApJ, 658, 778

Young, J. S., & Scoville, N. Z. 1991, ARA&A, 29, 581

Younger, J. D., et al. 2007, ApJ, 671, 1531

Yun, M. S., Reddy, N. A., & Condon, J. J. 2001, ApJ, 554, 803